PONTIFICIA UNIVERSIDAD CATÓLICA DE CHILE

ESCUELA DE INGENIERÍA

ADVANCES IN THE WESTERN ANDEAN FRONT AQUIFERS CHARACTERIZATION BY GRAVIMETRIC AND ELECTRICAL SURVEYS (CENTRAL CHILE – 32°50'S)

RONNY JAVIER FIGUEROA GONZÁLEZ

Thesis submitted to the Office of Research and Graduate Studies in partial fulfillment of the requirements for the Degree of Master of Science in Engineering

Advisors:
GONZALO YÁÑEZ
GLORIA ARANCIBIA

Santiago de Chile, (January, 2020)

PONTIFICIA UNIVERSIDAD CATÓLICA DE CHILE
ESCUELA DE INGENIERÍA

ADVANCES IN THE WESTERN ANDEAN FRONT AQUIFERS CHARACTERIZATION BY GRAVIMETRIC AND ELECTRICAL SURVEYS (CENTRAL CHILE – 32°50'S)

RONNY JAVIER FIGUEROA GONZÁLEZ

Members of the Committee:

GONZALO YÁÑEZ
GLORIA ARANCIBIA
FRANCISCO SUÁREZ
LINDA DANIELE
ENZO SAUMA

Thesis submitted to the Office of Research and Graduate Studies in partial fulfillment of the requirements for the Degree of Master of Science in Engineering

Santiago de Chile, (January, 2020)

Hakuna Matata

ACKNOWLEDGEMENTS

My greatest gratitude goes to my family: without their unconditional support I would not have been able to continue studying. To my mother, who taught me to persevere and give my best; to my siblings, Gerald, Rocio and Bastian who have helped and tolerated me in times of crisis. I thank Javi who has been a great friend and support during the Master, especially in times of crisis. To Almu for her incredible company, love and advice at all times.

I thank Gonzalo who has taught me so much in geoscientific subjects, but from whom I rescue even more lessons of life, patience and help since we know each other. To Gloria, to whom I attribute my involvement in the world of geosciences, in addition to all the times I went for her help and made me think in a practical and accurate way. To Linda, Matias and Benoit for the enriching discussions, advice and teachings on academic and life issues, as well as all their support on hydrogeological matters.

To my geo-friends Josefa, Felipe dV, Sofia, Maringue and Jorge for the nice moments we shared, and the purely scientific discussions accompanied by a cold beer. To my friends Felipe G., Alvaro, Seba, Arturo and Greco for their constant support and good disposition to relax in game sessions. Special thanks to all of those who accompanied me to the field; thank you for the good vibes and disposition in those countless field days.

This research was supported by projects FONDECYT n° 1170569 and the Andean Geothermal Center of Excellence (CEGA) FONDAP-CONICYT project n° 15090013. Partial funding for college fees came from the San Andrés scholarship, provided by College UC. I acknowledge financial support given by the Dirección de Postgrado de la Escuela de Ingeniería UC (DIPEI) to assist the IAH-congress. In addition, I thank Termas el Corazón and Mr. Anton for field access.

GENERAL INDEX

Page

TABLES INDEX

Page.

FIGURES INDEX

Page.

RESUMEN

En regiones áridas, las aguas subterráneas desempeñan un papel fundamental para el desarrollo de las actividades socioeconómicas y humanas. Las zonas montañosas proporcionan una gran parte del agua subterránea a través de diferentes mecanismos a las cuencas, donde las poblaciones se concentran mayoritariamente. Las zonas de falla condicionan la circulación del agua subterránea, debido a la modificación de la permeabilidad intrínseca de la roca fresca, en particular cuando se encuentra en la transición entre los frentes de montaña y las cuencas. Esta investigación se centra en la influencia de los límites y la geometría de las zonas de falla, en el flujo de agua subterránea de las áreas montañosas aledañas a la cuenca sedimentaria. Como caso de estudio, se estudió la Zona de Falla de Pocuro (PFZ), ubicada en la zona central de Chile (32.5S). Para llevar a cabo este objetivo, se usó una aproximación geofísica utilizando mediciones de gravedad y resistividad constreñida por datos geológicos e hidrogeológicos. Los resultados muestran variaciones significativas de la anomalía de la gravedad a lo largo de los perfiles: con (i) una anomalía nula en la parte alta de los cerros, debido a la fractura de las rocas, (ii) una anomalía negativa asimétrica al oeste del trazo de la falla, debido a un depocentro (alrededor de 150 - 200 m) de depósitos aluviales no consolidados en la cuenca, y (iii) variabilidad en los depósitos aluviales en la cuenca que sugiere una segmentación a lo largo de la zona PFZ. Las mediciones de resistividad eléctrica y las características de las aguas subterráneas (profundidad de la napa freática, conductividad eléctrica y ubicación de los manantiales) permiten definir tres posibles dominios hidrogeológicos: roca fracturada (de diferente intensidad), sedimentos y bandas subverticales de baja resistividad. Además, estas bandas subverticales, corroboradas con estudios geológicos, permiten un mapeo de fallas en profundidad. Finalmente, se propone un modelo conceptual para la Cuenca del Aconcagua en el borde de la PFZ, donde esta zona de falla es heterogénea y segmentada, por lo que la permeabilidad es variable a lo largo de la falla. El núcleo de falla es impermeable, debido a la presencia de salbanda rica en arcilla, mientras que las zonas de daño permiten el almacenamiento y el flujo del agua

subterránea. Aunque este estudio se enfocó en la PFZ, la relación entre fallas y manantiales en otras partes de Chile sugiere que estas conclusiones pueden ser extrapoladas a otras zonas de fallas.

ABSTRACT

In arid regions, groundwater plays a critical role for the development of socio-economic and human activities. Mountainous areas provide a large part of the groundwater through different mechanisms to the basins, where the populations are mainly concentrated. Fault zones determines the circulation of groundwater, due to the modification of the intrinsic permeability of the fresh rock, in particular when located at the transition between mountain fronts and basins. This research focus on the influence of the boundaries and geometry of fault zones on groundwater flow from mountainous areas adjacent to sedimentary basin. As a case study it was studied the Pocuro Fault Zone (PFZ), located in Central Chile (32.5S). To accomplish thus task it was used a geophysical approach using gravity and resistivity measurements constrained by geological and hydrogeological data. Results show show significant gravity anomaly variations along profiles: with (i) a null anomaly up the hill due to fractured rocks, (ii) an asymmetric negative anomaly to the west of the fault trace due to a thick depocenter (around 150 – 200 m) of non-consolidated alluvial deposits in the basin, and (iii) variability in the alluvial deposits in the basin that suggests a segmentation along PFZ. Electrical resistivity measurements and groundwater features (water table depth, electrical conductivity and spring locations) allow to define three possible hydrogeological domains: fractured rock (with different intensity), sediments and low resistivity subvertical bands. Furthermore, these subvertical bands, corroborated with geological surveys, allow a mapping of faults in depth. Finally, it was proposed a conceptual model for Aconcagua Basin in PFZ limit, where this fault zone is heterogenous and segmented, so permeability is variable along the fault. Fault's core are impermeable boundaries due to presence of gouge clay-rich, while damage zones allow to store and flow groundwater. Although this study focused on PFZ, the relationship between faults and springs in other parts of Chile suggests that these conclusions can be extrapolated to other fault zones.

Keywords: Groundwater, Fault Zone, Western Andean Front, Gravity, Electrical resistivity.

1. INTRODUCTION

Understanding fluid transport processes in fractured rocks on mountain fronts and their consequent role in the recharge of sedimentary basins is fundamental to quantify and efficiently manage water resources. The architecture of a fault zone controls groundwater circulation due to the modification of the intrinsic permeability of rocks. Springs in the piedmont are the surface manifestation of this intricate system, that link lithology, fault zones, and hydrogeological processes.

In Chile, geomorphology is largely controlled by subduction, and is characterized by three large domains: Principal Range, Central Depression, and Coastal Range. In the contact between the Principal Range and the Central Depression, several springs and hot springs related to fault zones (Hauser 1997) are evidence of groundwater flow in these mountainous areas. In the face of the water scarcity suffered in Central Chile (Valdés-Pineda *et al.* 2014; Garreaud *et al*. 2017, 2019), fault zones in mountainous areas could help to mitigate in part the effects of the growing drought resulting from climate change, because they are not affected by climatic variability.

In this thesis, the relation between fault zones and groundwater flow is addressed through a geophysical approach comparing geological, geomorphological and hydrogeological surveys. The first chapter of this thesis consists in a brief introduction of hydrogeological and structural geology concepts and the theoretical background of the methodology used. In addition, the statement of the problem, the research questions, the objectives and the hypothesis are also included in this chapter. The development and outcome of this research are presented in chapter 2 consistent of the article name *Advances in the characterization*

of Western Andean Front aquifers recharge processes by a multidisciplinary analysis (Central Chile), by Figueroa *et al*., submitted to *Journal of Hydrology (January 2020).*

1.1 Conceptual framework

1.1.1 Groundwater flow

Groundwater is a key source for drinking water, because of the total of 1380 million km^3, water on earth only 2.8 % is freshwater, while groundwater comprises more than 98% of the available freshwater (Schwartz and Zhang 2003). Generally, groundwater is found in aquifers which can store and transport water. An aquifer is a volume of sediment or rock that is sufficiently permeable to supply water to a well. Groundwater available in aquifers is a key resource during periods of drought, because it can remain in the subsurface from days to thousands of years depending on their origin (Fetter 2001).

Water circulates on the Earth from the oceans to the atmosphere to land and back to the oceans, this cyclic process is illustrated in Figure 1-1 and is called the hydrologic cycle. Water is evaporated from the surface on the oceans and in a gaseous state moves to the atmosphere. When the atmospheric conditions are suitable, water vapor condensates and form water droplets that fall to the oceans or onto land. Water precipitates on the land as a liquid or solid. If it is solid, it can temporarily accumulate as snow or ice. Precipitation drain through the land to a stream channel. If the surface is porous o fractured some surface water seeps into the ground, a process called infiltration. Infiltrated water may be evaporated and/or transpired (through plants), if kept in the partially saturated zone or vadose zone. Water that infiltrates deeper reaches the saturated zone and this water stored in this zone is called groundwater. Groundwater flows through the rock or soil, usually at

very slow rates (even thousands of years), until it discharges as springs, in a stream, in a lake, or ocean. When surface water o groundwater come to oceans, or lakes, the above processes begin again.

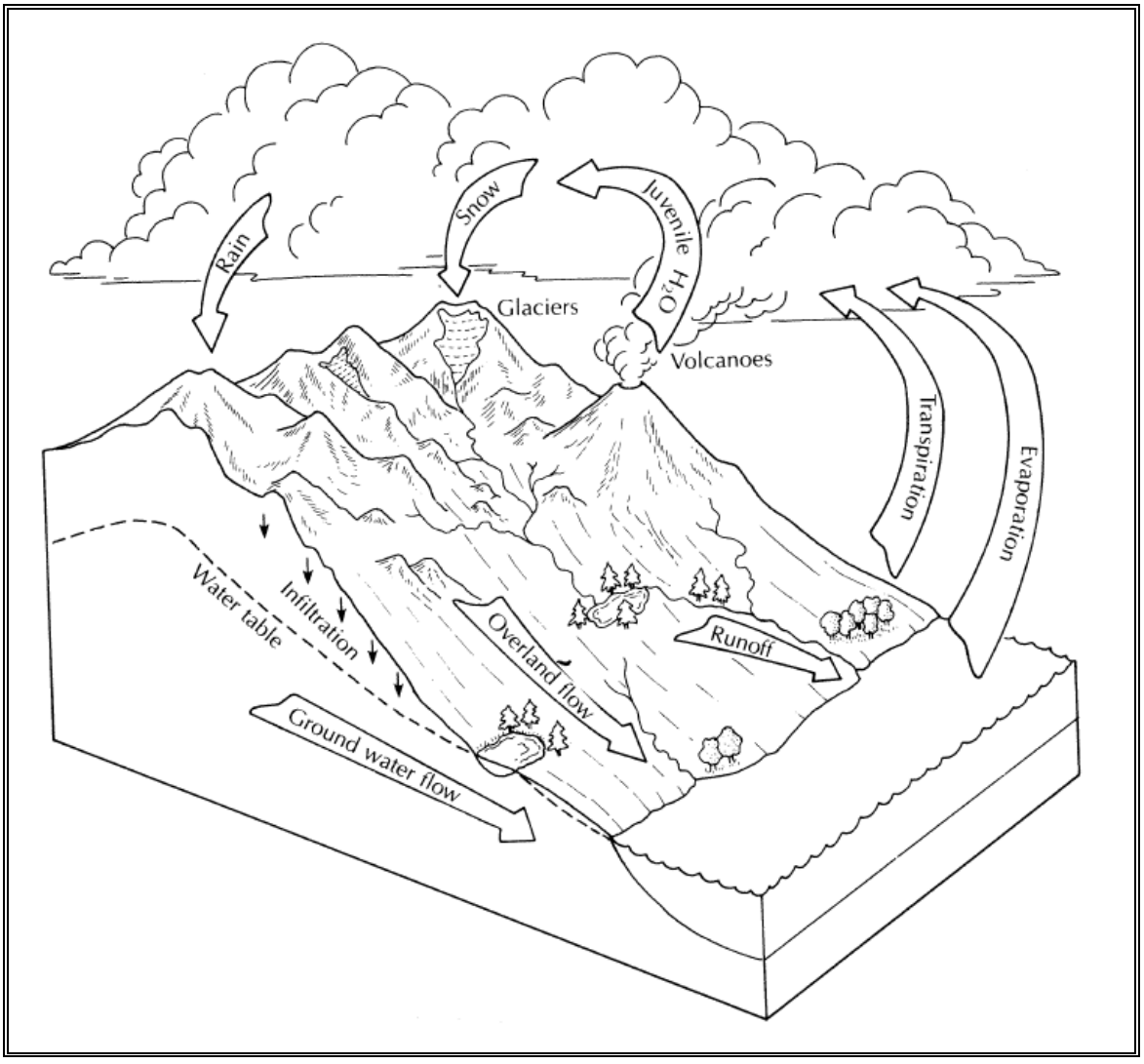

Figure 1-1. Hydrologic cycle (from Fetter, 2001)

Groundwater flows in sediments or rocks through open and connected spaces, called pore spaces. Porosity is defined as the ratio of the void volume to the total volume of soil or rock, mathematically can be written as

$$n = \frac{V_v}{V_T} = \frac{V_T - V_s}{V_T} \tag{1.1}$$

where n is the porosity, V_v is the volume of voids, V_s is the volume of solids, and V_T is the total volume. Also, porosity can be expressed in terms of the density, taking account density of dry soil or rock medium ρ_d, and the density of solids ρ_s

$$n = 1 - \frac{\rho_d}{\rho_s} \tag{1.2}$$

Groundwater can flow through primary and/or secondary porosity of rocks. Primary porosity is that associated with the voids that were created when the rock or soil was formed, such as pores in soil or sedimentary rocks, vesicles, lava tubes and cooling fractures in volcanic rocks. Secondary porosity is produced by processes subsequent to the formation of the rock, such as fracturing by faults or metamorphism, and dissolution of carbonate and other soluble rocks. Nevertheless, not all pores participate in the fluid flow due to non-connectivity between pores, or by molecular and capillary forces (e.g. in clays). The effective porosity is used when referring to groundwater flow, as it only considers the pore space in which the fluid flows.

The hydraulic conductivity is a parameter that describes the ease with which a fluid flows through a porous medium. Darcy´s Law (1856) defines hydraulic conductivity as a constant of proportionality, which relates the flow of water (discharge or flow) with the

difference of hydraulic head (hydraulic gradient) between two points. Mathematically, Darcy´s Law is expressed as

$$q = K\,i \leftrightarrow Q = K\,i\,A \tag{1.3}$$

where K is hydraulic conductivity [m s^{-1}], i is hydraulic gradient [m m^{-1}], A is the transverse area through which the fluid flows [m^2], q is the specific discharge or Darcy velocity [m s^{-1}], and Q is the flow rate [m^3 s^{-1}]. When the properties of the fluid (density and viscosity) change, hydraulic conductivity also change so it is best to consider the intrinsic permeability which is a property of the medium itself. Although density and viscosity of the water are relative constant, in the case of mixtures of fluids or polluted waters it is better to consider the intrinsic permeability. Hydraulic conductivity is expressed in terms of the intrinsic permeability as

$$K = \frac{k\,\rho_f\,g}{\mu_f} \tag{1.4}$$

where k is the intrinsic permeability [m^2], ρ_f is the fluid density [kg m^{-3}], g is the gravity acceleration (9.81 m s^{-2}), and μ_f is the dynamic viscosity of the fluid [kg m^{-1} s^{-1}]. Table 1-1 shows representative values of hydraulic conductivity and permeability for different mediums, taking account a dynamic viscosity of 0.001003 [kg m^{-1} s^{-1}] and a density 998.29 [kg m^{-3}] for water at 20°C.

Table 1-1. Representative values of hydraulic conductivity and permeability for different rocks and soil types (Schwartz and Zhang, 2003).

Material	Hydraulic Conductivity Log(m/s)	Intrinsic Permeability Log(m^2)
Sediments		
Gravel	-4 – -2	-11 – -9
Coarse sand	-7 – -3	-14 – -10
Medium sand	-7 – -4	-14 – -11
Fine sand	-7 – -4	-14 – -11
Silt, loess	-9 – -5	-16 – -12
Till	-12 – -6	-19 – -13
Clay	-11 – -9	-18 – -16
Sedimentary Rocks		
Karst and reef limestone	-6 – -2	-13 – -9
Limestone, dolomite	-9 – -6	-16 – -13
Sandstone	-10 – -6	-17 – -13
Siltstone	-11 – -8	-18 – -15
Salt	-12 – -10	-19 – -17
Anhydrite	-13 – -8	-20 – -15
Shale	-13 – -9	-20 – -16
Crystalline Rocks		
Permeable basalt	-7 – -2	-14 – -9
Fractured igneous rocks	-9 – -4	-16 – -11
Weathered granite	-6 – -5	-13 – -12
Weathered gabbro	-7 – -6	-14 – -13
Basalt	-11 – -7	-18 – -14
Unfractured igneous rocks	-14 – -10	-21 – -17

The permeability and effective porosity of the media are directly related to the productivity and availability of the aquifer. Two geometrically equivalent aquifers (thickness of the water column, lateral and vertical dimensions), but with different hydrogeological properties (permeability and effective porosity) should be managed differently due to their productivity. The lower the permeable aquifer (Figure 1-2.a), the lower the productivity, and the greater the water table depression around the well, the higher the permeable

aquifer, the higher the productivity, and the less significant depression in the water table when extracting water (Figure 1-2.b). Consistently, the effective porosity is inversely proportional to the radius of influence that the water table suffers when extracting water from a well. If the effective porosity is low, the radius of influence when extracting water by pumping will be large (Figure 1-2.c), whereas it will be a limited radius of influence if the porosity is high (Figure 1-2.d) (Freeze and Cherry, 1979).

As the hydraulic properties depend of the type of rocks or sediments, aquifers will be characterized by geology and water availability. An aquifer is defined by its capacity to store and transmit water; it depends directly on the hydraulic conductivity. Thus, an aquifer is bounded by a medium that is impermeable or of low hydraulic conductivity. For example, the aquifer volume in a basin with high permeability (if there is a water source), is bounded by areas of low or impervious permeability, like outcropping basement in the surrounding areas. When basement rocks are fractured, medium porosity increases, thus boundaries of the aquifer will be greater, extending the occurrence of groundwater towards the fractured rock on the adjacent mountain. So, the different geological units and deformation processes control the hydraulic properties, that define the geometry and boundaries of the aquifer. Both of them directly impact on the volume of groundwater, and on the extraction capacity to which the aquifer can be subjected.

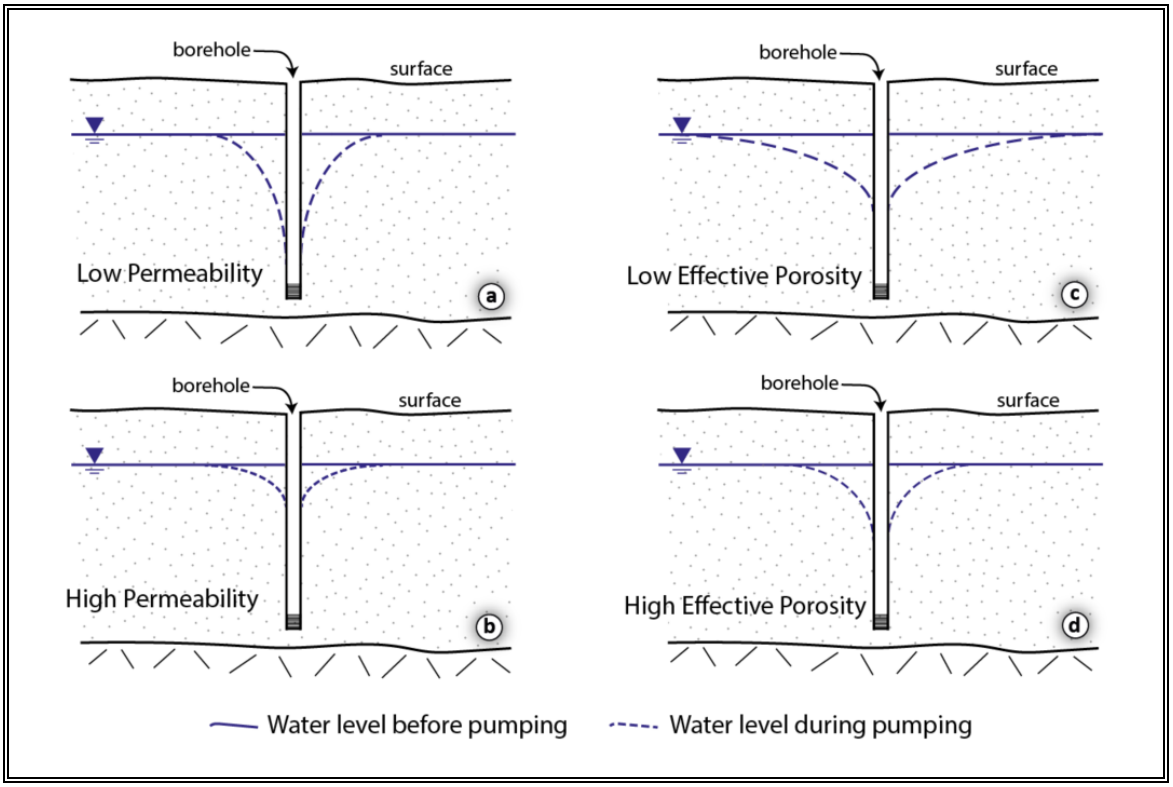

Figure 1-2. Comparison of the influence of water level on the pumping of an aquifer a) low permeability, b) high permeability, c) low storage and d) high storage (modified from Freeze and Cherry, 1979).

1.1.2 Regional groundwater flow

Groundwater flows when a hydraulic head gradient is observed, from high to low hydraulic head, or physically, from areas of recharge to areas of discharge. The recharge refers to water that infiltrates and enters the aquifer. On the other hand, the discharge refers to water volume detached from the dynamic flow of groundwater, either by stream baseflow, springs, seepage areas, or evapotranspiration. Recharge areas are usually in topographical high places, while discharge areas are located in topographic lows. Figure 1-3 shows a regional steady-state flow of groundwater an upland to nearby streams in an isotropic and homogeneous medium, which exemplifies a groundwater basin with flow

lines, the recharge area, and the discharge areas. Equipotential lines represent a surface of same hydraulic head, so if there is a gradient of equipotential lines there would be flow.

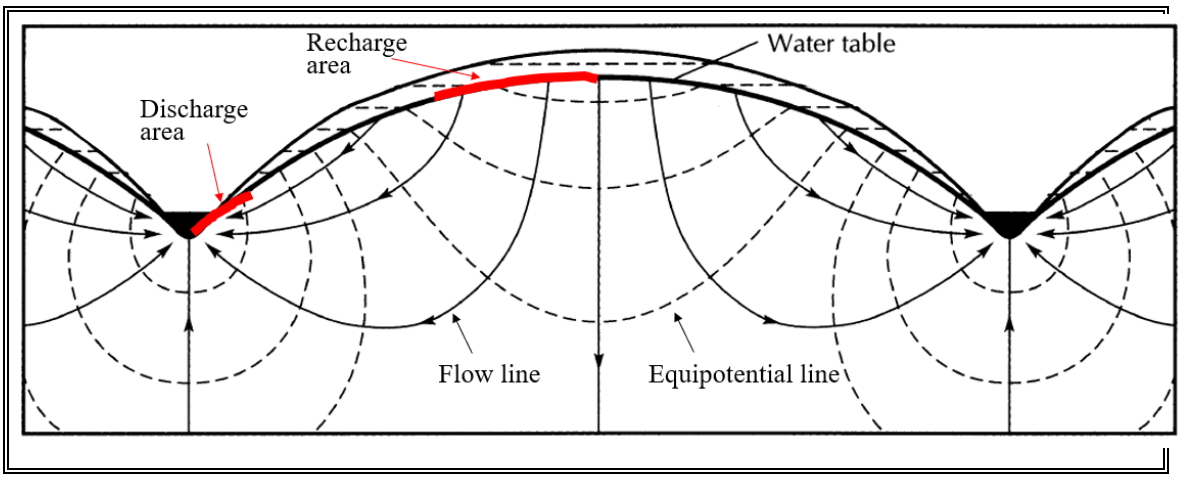

Figure 1-3. Cross-sectional flow pattern controlled by topography. (from Hubbert, 1940 in Fetter, 2002).

It is important to emphasize that groundwater flow is a three-dimensional phenomenon, but for simplicity is usually represented in two dimensions. Although the example of the Figure 1-3 is a simple case where the medium is isotropic and homogeneous, where discharge and recharge areas are focalized, but the reality is normally very different. As stated above, groundwater flow depends of the hydraulic gradient and the permeability of the medium (or hydraulic conductivity), so groundwater flow is largely controlled by the geology/lithology of the medium, and the geological processes that shape the geomorphology and modify the primary permeability of the rocks and deposits. Figure 1-4 shows a conceptual model of the hydrogeological system of the Utah basin, US (Robson and Banta 1995), where it can be recognized different recharge processes to the basin, such as infiltration from the surface (by precipitation, streamflow, and mountain-front),

and underground flows (from mountains or in the same basin). In addition, discharges areas could be multiples points (or surfaces), such as evaporation, withdrawal by wells, or seepage flows.

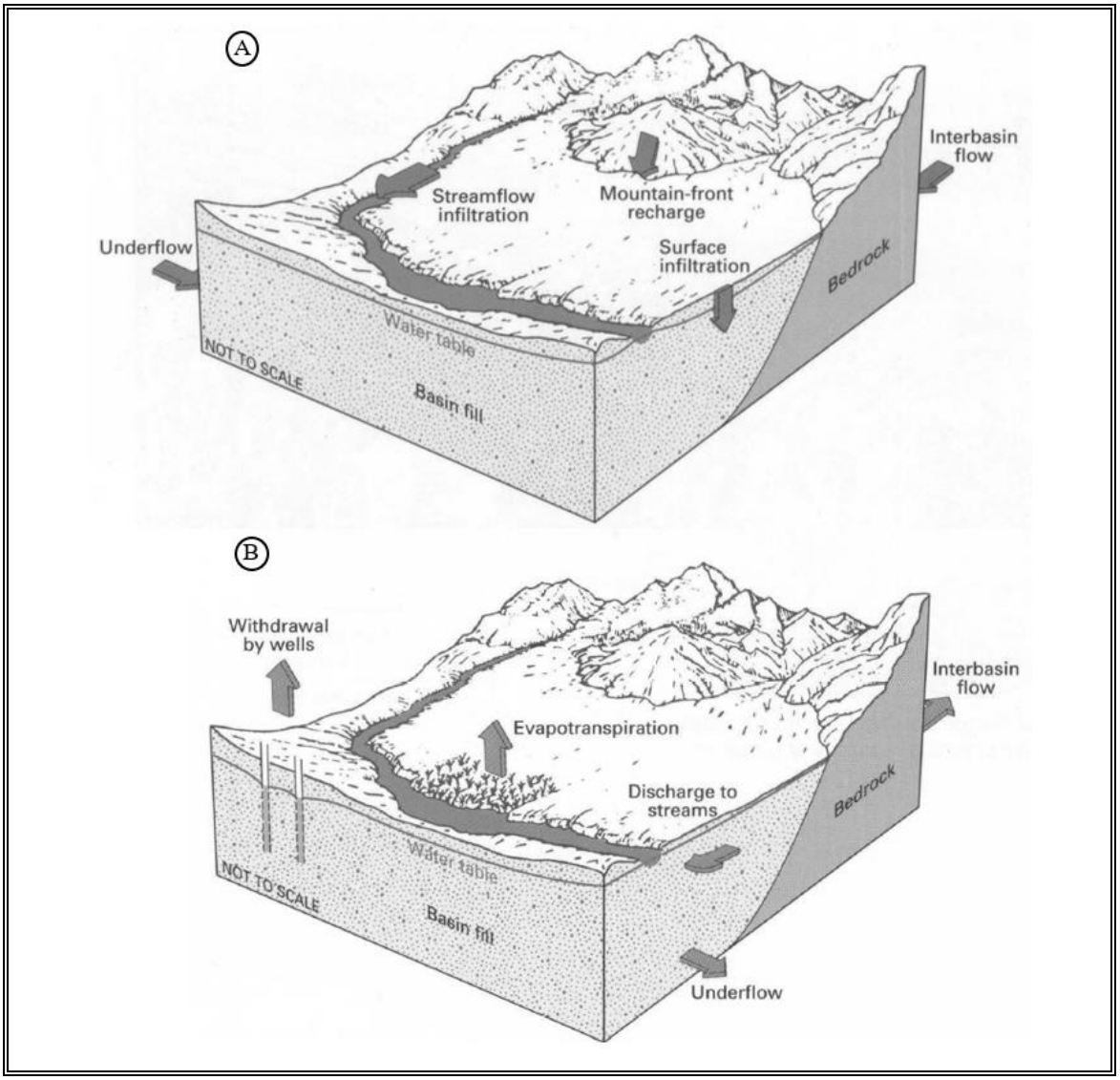

Figure 1-4. Basin and mountainous area setting. Aquifer in basin with (a) component of groundwater recharge, and (b) components of groundwater discharge (from Robson and Banta, 1995).

In arid or semiarid environments, mountain regions have a key role in the contribution of groundwater supply to aquifers in adjacent basins. A mountainous area (mountains, elevated areas, mountain range) receive more precipitation than on basin surface (rain and snow). In addition, the evapotranspiration is less, due to lower temperatures and a larger surface albedo (Wilson and Guan 2004). According to Viviroli *et al*. (2003), the water contribution of mountains, by unitary surface, to annual river basin discharge is about 4 times that of the basin.

Mountain system recharge (MSR) is the processes of recharge to alluvial basin in semi-arid climate and Range zones (Wilson and Guan 2004; Wahi *et al*. 2008). MSR (Figure 1-5) consists of water runoff on mountains that infiltrates at mountain front (mountain front recharge (MFR)). Furthermore, it could exist a contribution to the basin through deep groundwater that is percolated in the mountain bedrock (mountain block recharge (MBR)) (Wahi et al., 2008). In an MSR is possible to recognize four groundwater contribution from mountainous areas to the basin (Wilson and Guan, 2004):

1) *Focused shallow contributions*, which represents input from stream runoff and groundwater transmitted by alluvial fans.

2) *Diffuse shallow contributions*, this input occurs along slope through ephemeral surface runoff that produce small and thin channels called rills.

3) *Focused deep contribution*, this is groundwater transmitted along bedrock openings, such a crevices, fractures and faults that connect from the mountain-block to the basin aquifer.

4) *Diffuse deep contribution*, when the bedrock permeability is high (such as tuff, conglomerate, sandstone, fractured rock), there is a flow from the mountain block to the sediment of the basin aquifer.

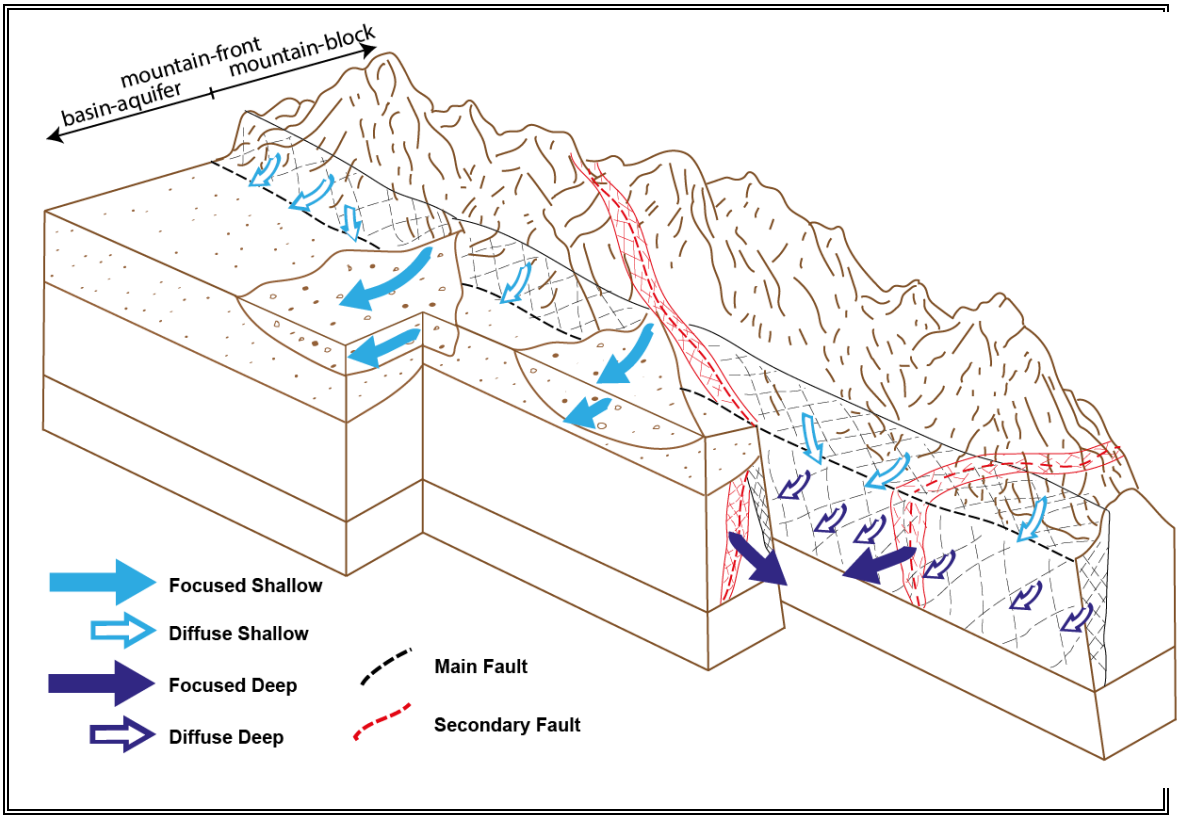

Figure 1-5. Conceptual model MSR groundwater contribution from mountain to the basin (modified from Wilson and Guan, 2004).

The time scale between all these processes are very different, while surface runoff occurs over a period of days to weeks, the recharge on the basin by groundwater circulation could take hundreds to thousands of years (Sanford 2002; Manning and Solomon 2005). Groundwater plays a key role for long periods of drought where surface runoff is considerably less because it becomes the available resource. Therefore, groundwater

recharge is very relevant. In an arid or semiarid climate, the surface water is easily evaporated due to the solar radiation, in contrast, the groundwater is not affected by solar radiation and thus being preserved and transmitted along bedrock openings (Wilson and Guan 2004; Bense *et al*. 2013; Roques *et al*. 2014; Bense *et al*. 2016). The surface evidence of groundwater flow under mountainous areas are springs. The changes in topography perturb the water table configuration. In particular, under high permeability conditions of fault zones, groundwater can flow through fractures emerging on the surface. Thus, fault zones can exert strong controls on the hydraulics properties and groundwater circulation, due to potential changes to the intrinsic permeability of the bedrock. Figure 1-6 shows some examples where, as a result of a fault zones, springs emerge on piedmont of mountainous region as a result of: (a) the formation of a hydrogeological barrier, (b) topographical and low permeability condition combination, or (c) by the formation of a preferential pathways for groundwater circulation.

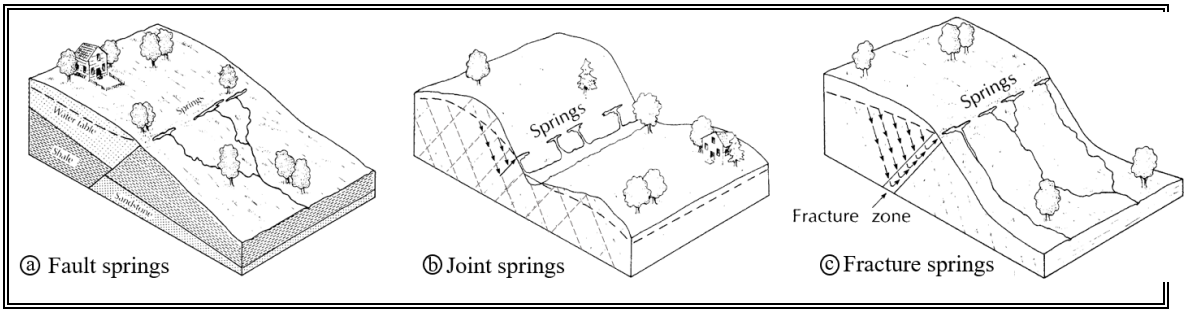

Figure 1-6. Types of spring in fractured media by faulting (from Fetter, 2001).

1.1.3 Fault zone architecture

Fault zones and fracture systems can control groundwater flows at the local and regional scales, acting as fractured aquifer, creating preferential pathways for groundwater circulation, or acting as hydrogeological barriers that prevent the fluid flow (e.g., Garven 1995; Bense *et al*. 2013). Fault zone architecture and associated processes (Figure 1-7) strongly controls the groundwater flow, by increasing or decreasing the intrinsic permeability of the host rock. A fault zone can be divided in two permeability domains, a fault core and a damage zone (Caine *et al*. 1996; Faulkner *et al.* 2010). The fault core is a volume where slip and strain concentrate, usually, there is clay-rich gouge development, grain-size reduction, and cementation and mineralization by fluid-rock interaction, which produces a less permeable domain compared to the bedrock. However, the less strained damage zone domain, which surrounds the fault core, provides a more favorable path for water flow, due to the presence of fractures and faults that increases the permeability.

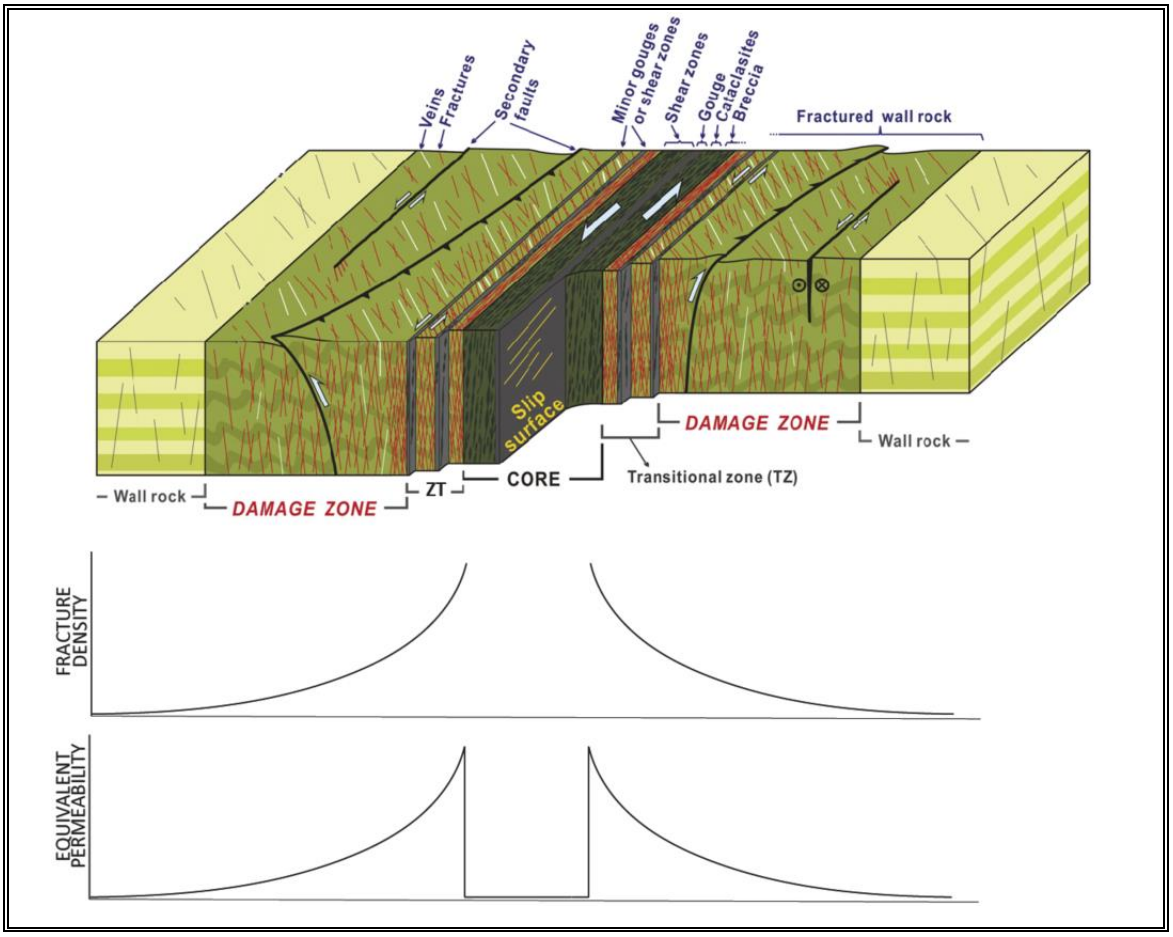

Figure 1-7. Schematic of a fault zone architecture and physical properties related to its structure (from Faulkner *et al.* 2010, Choi *et al.* 2016).

However, it is relevant to specify the state of evolution of the fault zone, as its equivalent permeability may vary (Bruhn *et al.* 1994). The core could act as a preferential pathway for fluid flow during the slip and as a barrier when fractures are filled by minerals precipitating after the slip (Chester and Logan 1986). Studies in the Dixie Valley fault zone (Bruhn *et al.* 1994) indicates that the fault core acted as a short-lived conduit for fluid flow, which was quickly sealed to form a barrier to flow. Normally, the permeability of a fault zone, either a barrier, conduit, or both, cannot be determined, because the lack a of a full exposure. Also, permeabilities measured in-situ do not necessarily represent the

permeability of the fault zone as a whole, given its depth extension of several to hundreds of meters. On the other hand, pumping tests, commonly used to determine the hydraulic conductivity of the medium, are difficult and costly. Besides that, it requires a large number and distribution of boreholes to characterize the medium (Bense *et al*. 2013). Geophysical techniques, such as electric and electromagnetic methods, seismic reflection, self-potential and geo-radar have been shown to be efficient in characterizing hydrogeological domains, indicating areas of greater or lesser permeability and thus also the water table level. So, characterizing and defining the influence of a fault zone on fluid circulation is a critical condition for the study of groundwater because it could be a boundary condition for fluid circulation and/or modify the medium to form preferential pathways for circulation and storage of water resources.

1.1.4 Freshwater availability in Chile

In Chile, according to World Bank (2011), mean water availability per person is 53000 $m^3\,hab^{-1}\,yr^{-1}$, much more than the internationally defined minimum value for sustainable development (2000 $m^3\,hab^{-1}\,yr^{-1}$) (Valdés-Pineda *et al.* 2014). However, natural water availability per person is unequally distributed, while from Santiago to the north of the country, where more than 60% of population is concentrated (Table 1-2), water availability is 800 $m^3\,hab^{-1}\,yr^{-1}$. On the contrary, south of Santiago where water availability exceeds 10000 $m^3\,hab^{-1}\,yr^{-1}$ (World Bank 2011 in Valdés-Pineda *et al.* 2014).

Table 1-2. Population and water availability per person by region in Chile. Total water availability is the national average. Regions highlighted in color are part of Central Chile. *these values consider two regions (Arica y Parinacota and Tarapaca, Los Ríos and Los Lagos)

Region	Estimate Population	Percentage of Population [%]	Water Availability [$m^3\,hab^{-1}\,yr^{-1}$]
Total	18,373,917	100.00	53,953
Arica y Parinacota*	247,129	1.34	854
Tarapaca	352,712	1.92	
Antofagasta	640,950	3.49	52
Atacama	320,799	1.75	208
Coquimbo	794,359	4.32	1,020
Valparaiso	1,859,672	10.12	801
Metropolitana	7,482,635	40.72	525
O´Higgins	934,671	5.09	6,829
Maule	1,057,533	5.76	23,978
Biobío	2,141,039	11.65	21,556
La Araucanía	1,001,975	5.45	49,273
Los Ríos*	410,097	2.23	136,207
Los Lagos	853,663	4.65	
Aysén	110,288	0.60	2,993,535
Magallanes	166,395	0.91	1,959,036

Water availabity per person distribution depends largely on the topography factors, climate, and distribution of population throughout Chile. In the chilean territory is possible to distinguish three major geomorphological domains: Principal Range, Central Depression and Coastal Range (Figure 1-8a). In general, the territory is domanted by mountainous areas, and only around 20% of the territory is flat (INE, 2011 in Valdés-Pineda et al., 2014). In turn, the highest concentrations of population is in Central Chile (between 30° - 38°S) which correspond to the regions of Valparaiso, Metropolitana, O'Higgins, Maule and Biobío (Table 1-2). In addition, the highest water consumption in these regions is on flat terrains along the Central Depresion (Rivera et al., 2016).

In addition, the climate and precipitation patterns in Chile are mostly controlled by topographic effects and location at the Pacific coast of South America (Marchant *et al.* 2007; Muñoz *et al*. 2007). This provokes a variety of climates along of the country (Figure 1-8b), with hyper-arid and arid climates in Northern regions, semiarid with winter rain in Central Chile, humid climates in Southern regions, and humid cool-temperature and polar climates in the Andes Mountains (Marchant *et al.* 2007; Valdés-Pineda *et al.* 2014). So, the precipitation and evaporation along Chile are distributed in accordance with the local climate. While in Northern regions the precipitations are practically zero, the Southern regions can exceed 3000 mm per year. In the other hand, the evaporation in Northern regions, due to the temperature, runoff, and water bodies, are very poor compared to the Southern regions (Muñoz *et al.* 2007). Figure 1-9 shows the spatial distribution of mean annual precipitation in Chile, latitudinally and longitudinally. In regions where the annual rainfall is low or almost non-existent, groundwater is the main source of this resource.

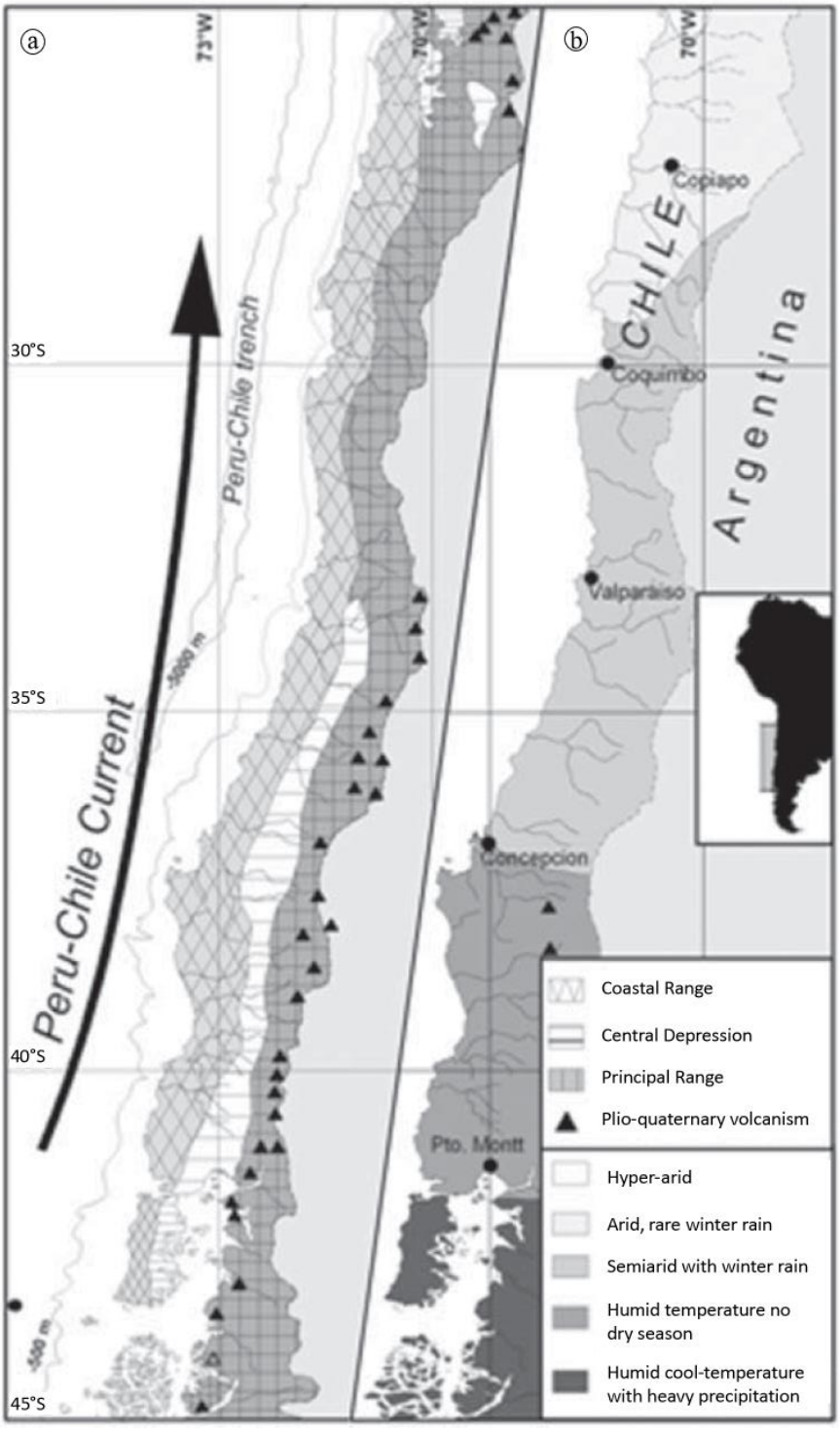

Figure 1-8. Major geomorphology domains and climatic zonation of Chile (Marchant *et al.* 2007).

According to the National Hydrogeological Maps (1: 1000000 and 1: 1250000), developed by Dirección General de Aguas – DGA, the main aquifers and groundwater are concentrated in alluvial basins in the Central Depression, with sediments of moderate to high permeability (Muñoz *et al.* 2007; Valdés-Pineda *et al.* 2014). These aquifers are bounded by low permeability rocks from the Principal Range to the east and the Coastal Range to the west. So, most of the wells are located in the Central Depression in alluvial-plain aquifers and considering basement rock as impermeable domains.

Numerous uncertainties exist regarding the groundwater circulation, from the Andean mountain block up to the Central Depression, despite is today highly relevant for the correct management of groundwater resources. Indeed, the increasing water demand for agriculture, mining and drinking over the last decades (Rivera *et al*. 2016; Valdés-Pineda *et al.* 2014), together with a megadrought that has been going on since 2010 (Garreaud *et al.* 2017, 2019), have depleted the alluvial-plain aquifers of Central Chile.

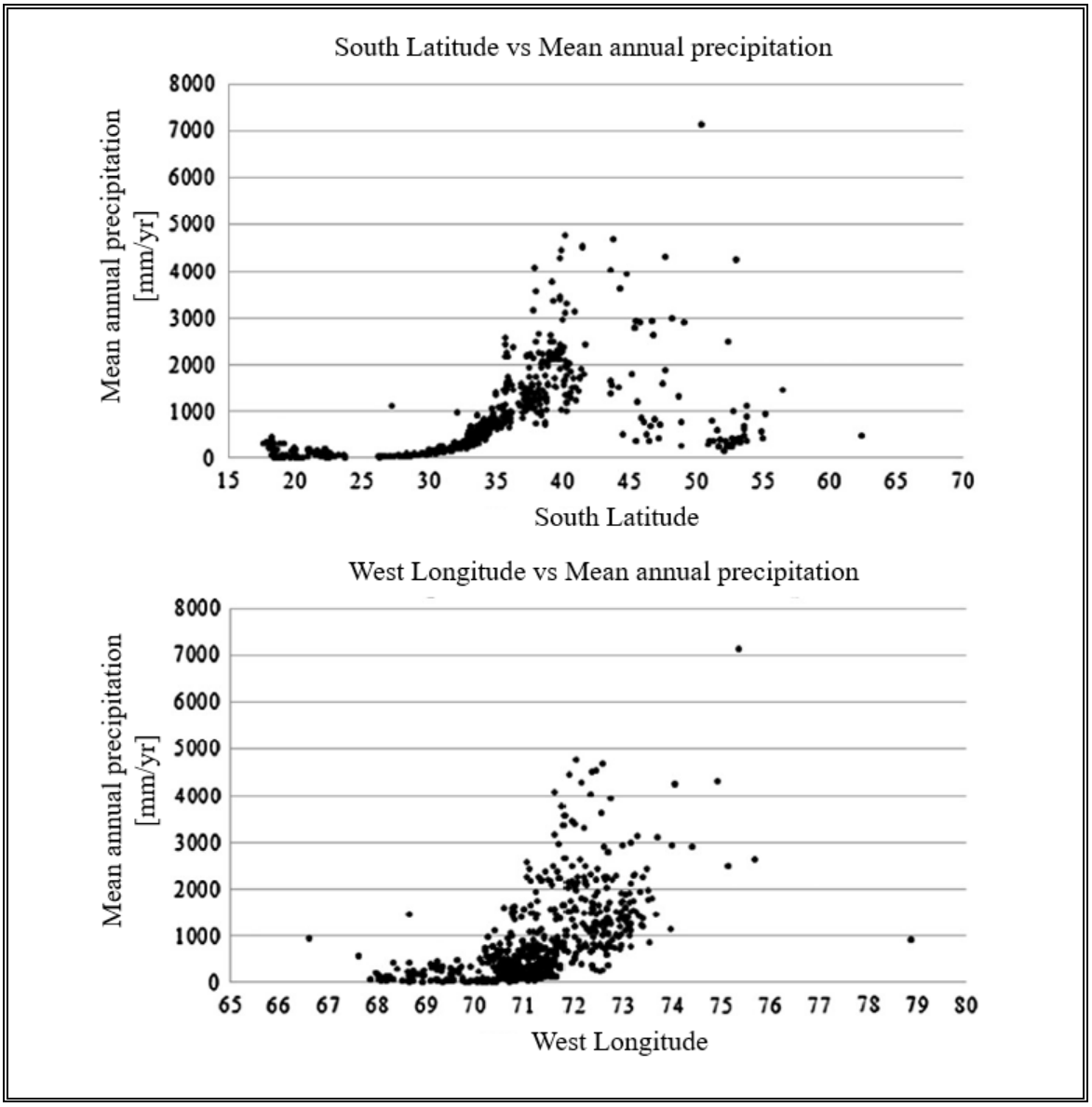

Figure 1-9. Spatial distribution of mean annual precipitation in Chile as a function of latitude and longitude (Valdés-Pineda *et al.* 2014).

1.2 Statement of the problem

Mountain ranges adjacent to sedimentary basins play a key role in the contribution of freshwater to aquifers in alluvial plains, especially in arid and semi-arid climates. This contribution of freshwater is commonly attributed to surface runoff through rivers, or by circulation of groundwater through permeable domains of sediment and/or rock. In mountainous areas, where the medium corresponds in general to low permeability rocks, the circulation of fluids could be improved/worsen considerably at fault zones. The development of extensive fracture networks increases the permeability, while when fractures are sealed by precipitation of minerals circulation is nil. So, it is relevant to assess whether and how fault zones on the mountain front are potential areas to contribute water from mountainous areas to sedimentary basins downwards.

It is known that the recharge of aquifers in sedimentary basins comes mostly from nearby mountainous areas, where rainfall can be at least four times greater (Wilson and Guan 2004). On the other hand, a fault zone modifies the hydrogeological properties of rocks, provoking changes in groundwater flow, inclusive variations in the piezometric level (Faulkner *et al.* 2010; Bense *et al.* 2013). Therefore, understanding the role of fault zones in mountainous areas adjacent to basin aquifers, would allow to focus/discard areas for a better use of the water resource.

In this context, the geometry and hydrogeological properties of the fault zones can have a strong control on the groundwater circulation in the first hundred of meters of the surface. This influence has an impact both on the mountain front (directly in the basin), and on adjacent mountain areas. Therefore, analyzing the potential of fault zones on the mountain

front to recharge alluvial basins is crucial for understanding, and then managing water resources.

This problem has great relevance due to the water scarcity that has affected Chile in the last decade. A better understanding of groundwater circulation in mountain areas provides new horizons in the management of this resource. Currently, in Chile, groundwater exploration and exploitation are only carried out in alluvial basins, while it has been demonstrated the feasibility to exploit this resource in fractured media (e.g., Roques *et al.* 2014; 2016). Due to the geomorphology of Chile, where the mountain front is in contact with the Central Depression, the groundwater contribution of the Western Andean Front to the over demanded aquifers in the Central Depression can be significant.

The Pocuro fault zone (PFZ) corresponds to an excellent case-study to address the problem mentioned above, since the Aconcagua basin is adjacent to the western front of the Andes mountain range. This contact involves an area of high degree of fracture where several springs are observed on the mountain front. However, the kinematics and seismic activity of the PFZ are beyond the scope of this research.

1.3 Objectives

The main purpose of this research is to evaluate the potential of the Western Andean Front to contribute to the recharge of aquifers in the Central Depression. Specific aims are: 1) to determine geometries, hydrogeologic boundary conditions and recharge processes on the Western Andean Front, 2) to understand the role of a fault zone in groundwater circulation on the Western Andean Front, and 3) to evaluate the hydrogeologic influence on the groundwater circulation of the PFZ as a case study.

1.4 Hypothesis

The working hypothesis is that the Western Andean Front contributes to the recharge of aquifers in the Central Depression. This geological process would involve the faults and fractures present in the mountain front that generate conduits through which groundwater may circulate, connecting the mountain block to the Central Depression. The proposed mechanism can be inferred through changes in physical properties, such as resistivity and gravity, which can be measured at the field. These observations allow to distinguish the heterogeneity along the fault zone and the preferential circulation paths

1.5 Study case: Pocuro fault zone

The Aconcagua basin (Fig. 1-10 and 1-11) is located in Valparaiso region, which is part of Central Chile, it is one of the most populated regions and it has water availability deficit. The Aconcagua river flows from the Principal range, crosses the Central Depression and discharges into the Pacific Ocean. Aconcagua basin is bounded to the east by the Pocuro fault zone (PFZ), which puts in contact the Central Depression with the Principal range.

The presence of springs on the eastern mountain front and the different outcrops in this area, make the PFZ an ideal study area for understanding the groundwater circulation in a fault zone.

1.5.1 Geological framework

PFZ is a north-south striking fault zone, which 150 km long and 2 km wide. In the landscape, PFZ puts Andes range and the Oligocene-Miocene volcano-sedimentary sequences (Abanico Fm.) in contact with the quaternary alluvial deposits of the Aconcagua Basin to the west. Also, the northern portion of the occidental block of the fault is composed of Upper Cretaceous volcanic-sedimentary rocks (Las Chilcas Fm.) (Rivano *et al.* 1993).

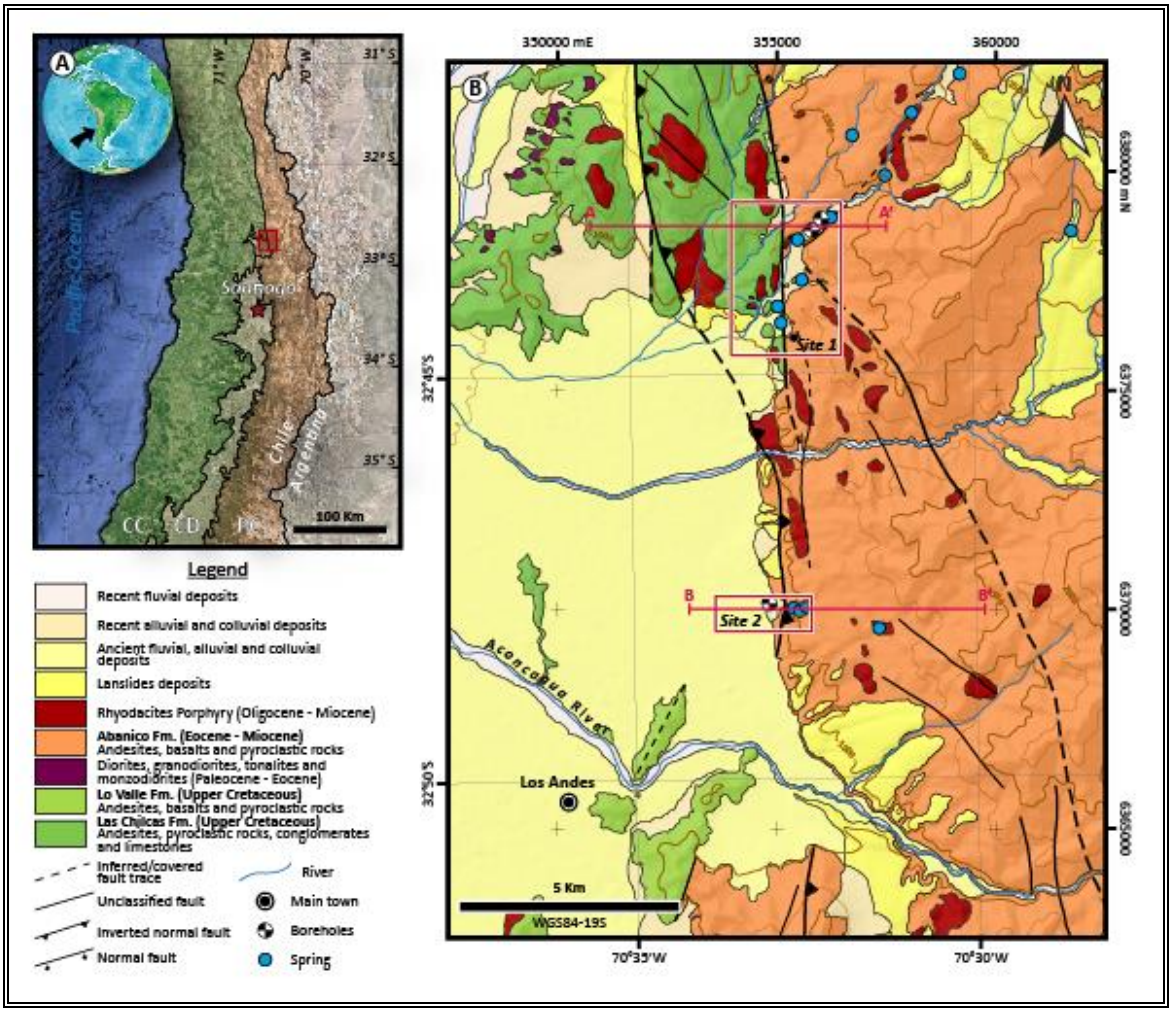

Figure 1-10. Maps showing A the geomorphology of Chile Central and the study area in Los Andes. B is a geological map which shows the PFZ.

The PFZ is a structure composed by high-angle reversed faults with east dip and north-south strike, including associated structures with strike N50W and N60E to E-W (Carter and Aguirre 1965; Rivano *et al.* 1993; Jara and Charrier 2014). The PFZ has probably being active at least until Early Miocene (Jara and Charrier 2014). During the Cenozoic, this fault zone has two stages of activity: first, a normal movement associated to formation of Abanico Basin, and after, its inversion in the form of a strike-reverse slip (Fuentes *et al.* 2004; Jara and Charrier 2014).

1.5.2 Hydrology and climate context

The Aconcagua Basin is characterized by a semi-arid climate, with mild wet winters and dry summers. The summers are semi-permanently affected by the blocking of a high-pressure cell over the southeast Pacific Ocean, precipitation is close to zero, the humidity is low and the solar radiation very intensive (Pellicciotti *et al.* 2007; Ragettli and Pellicciotti 2012). During the summer months, from November to March, the water contribution is mainly from snowmelt and ice melt, in addition, in years of drought snow and ice contribute up to 60% of the river flows (Peña and Nazarala 1987; Ragettli and Pellicciotti 2012). During the winter, mainly concentered between May to September, this region is affected by a frontal and orographic precipitation. The precipitation at high altitudes (above 2500 m a.s.l.) fluctuates between 700 - 800 mm year $^{-1}$ (Azócar and Brenning 2010; Bown *et al.* 2008).

The San Felipe aquifer (DGA 2015) is defined in the alluvial deposits of the Aconcagua basin. As DGA pointed out, the aquifer is limited to the east by the Principal Range, and by the Coastal Range to the west, which are mostly cretaceous rocks of low to null permeability. However, there are several perennial springs outflow from fractured rock on the mountain front (Hauser 1997; Bustamante *et al.* 2012) that could be related to the PFZ. Moreover, the Aconcagua river is considered the main source of water resources in the basin and it is considered the main mechanism for recharging the aquifer of the basin, together with the recharge coming from the precipitations in the basin (DGA 2015, 2016). During years 2010 to 2018 there was a series of years of drought, with annual rainfall deficit reaching up to 45% in Central Chile (Garreaud *et al.* 2017, 2019) shown in Figure

1-11. This extensive dry event occurred during El Niño Southern Oscillation neutral conditions. However, it is estimated that a quarter of the rainfall deficit during these years has an anthropogenic origin (Boisier *et al.* 2017). The deficit of precipitation decreased the cover snow causing decreases in the river flows and groundwater levels along the Central Chile. On the other hand, the extensive vegetation cover together with the high temperatures increase the potential for evapotranspiration causing less or no infiltration to the aquifers (Garreaud *et al*. 2017, 2019).

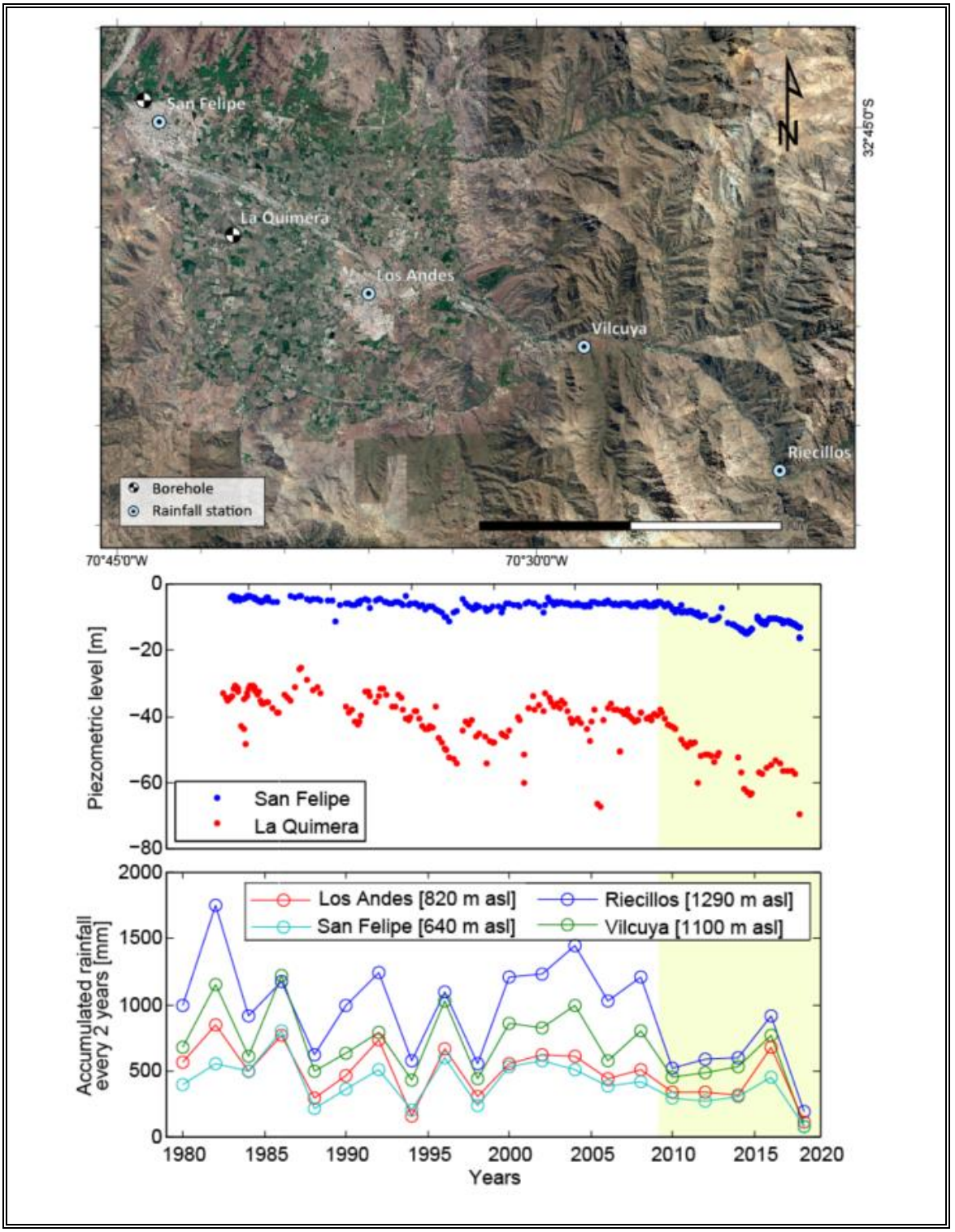

Figure 1-11. Rainfall distribution in Aconcagua basin and piezometric level in representative boreholes. From the year 2009 considered a period of drought. Available data at DGA web site (DGA, 2019).

1.6 Methodology

Gravity and geoelectrical data were acquired and modeled for the purpose of characterizing the subsurface in terms of density and electrical resistivity. This characterization was compared with spring locations, piezometric level in observation boreholes, and geomorphological-geological surveys, in order to carry out an integrate interpretation of the study area. Gravimetric method allows to discriminate density contrast between different mediums through small variations in the gravitational field, which makes it ideal for inferring the contact geometry between the basement and the sedimentary infilling. Electrical methods allow the identification of domains where water content is higher by interpreting electrical resistivity. Domains with higher water content will respond as a relative conductor, while domains with lower water content will respond as a relative resistive.

1.6.1 Gravity method

The gravity method is a geophysical technic that uses the variations of the gravitational field to identify excess or defects of mass in the crustal earth (Telford *et al.* 1990). Appendix A illustrates the physics and fundamentals of the gravity method.

In this work, 400 gravity stations were measured in four profiles at the wester front of the Andes. The gravity data were acquired using a relative gravimeter Scintrex CG-5 with a resolution of 5 μGal. One of these profiles was deployed in a valley within the mountain, where the gravity stations were measured along the valley. The other three profiles were E-W located on piedmont from the mountain to the basin, crossing the main trace of the PFZ. The spacing between gravity station was 100 m, except on the center of the three

profiles at piedmont where the spacing was 50 m, every gravity point considers two measurements of one minute each one. The gravimetric method requires very accurate location of stations, so it is necessary the have high-precision GPS measurements. For that purpose, a Trimble R4 GPS in differential mode was used, with records of 3 min. The locations of gravity experiments are shown in Figure 1-12.

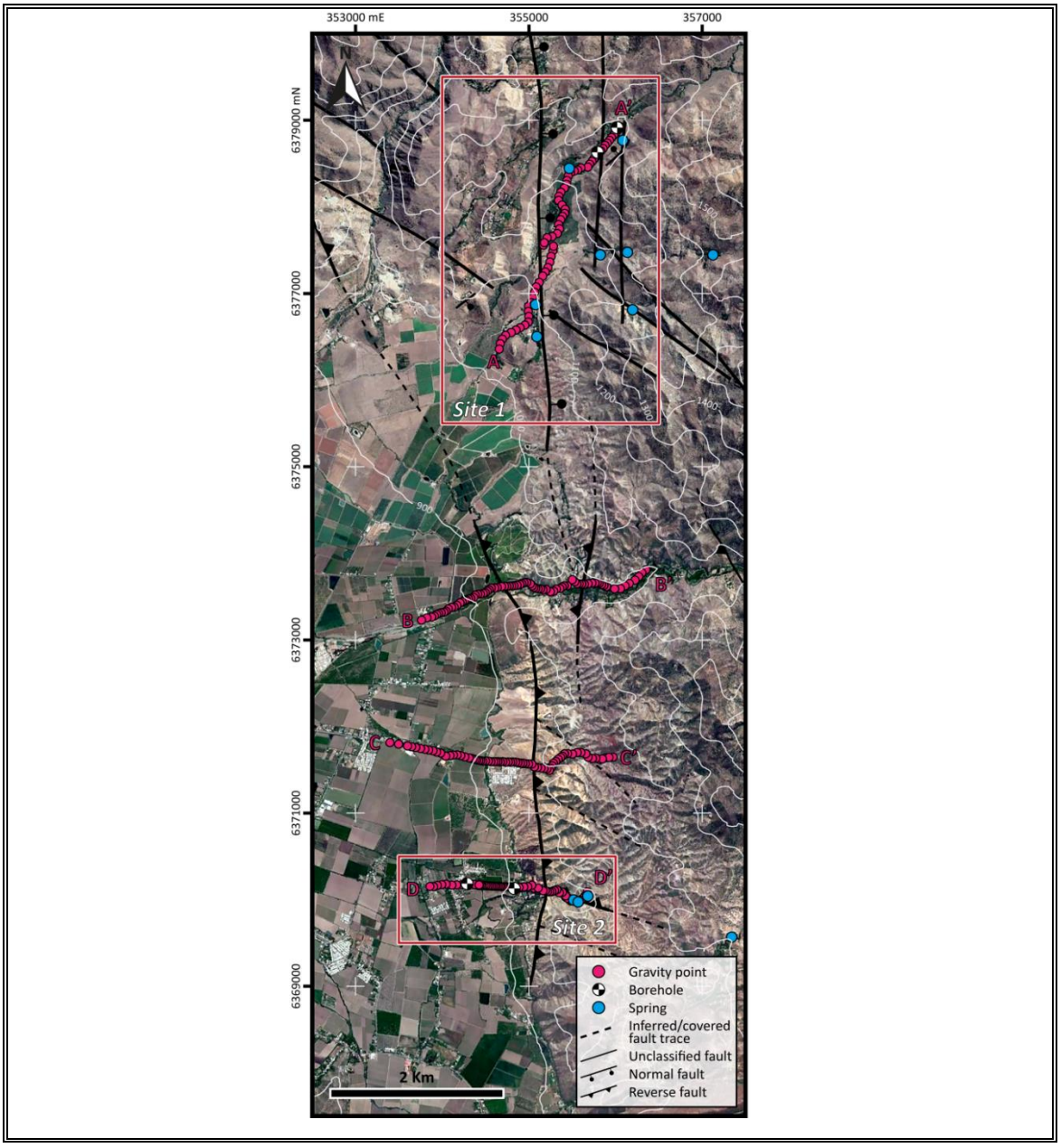

Figure 1-12. Gravity data location

After the acquisition of all the gravity stations, they were processed to determine the residual anomaly, used for geological interpretation. Data processing include the following steps: (0) gravity-GPS link ; 1) instrumental drift, 2) daily drift, 3) earth tide correction (ETC), 4) conversion to absolute value, 5) latitude correction, 6) free-air

correction, 7) bouguer correction, 8) terrain correction, and 9) regional effect. For details of gravity processing see Appendix A.

Once the residual anomaly values have been obtained, each profile was modelled using the software Model Vision. This modelling was carried out considering a density contrast $\Delta\rho = 0.5$ [g/cm^3] between the basement rock and the sedimentary infilling. This density contrast is supported by in-situ measurement of density in 6 rock samples (three from Abanico Fm. and three from Las Chilcas Fm.) and considering density values from Bustamante *et al.* (2012). In addition, gravity models were calibrated with resistivity models in sites 1 and 2. Gravity models are further constraints by geological and geomorphological observations.

1.6.2 Electrical resistivity tomography

An Electrical Resistivity Tomography (ERT) is a geophysical method that use the Ohm´s law and the Maxwell´s equation to obtain an electrical resistivity of the subsurface (Telford *et al.* 1990). ERT allows a two-dimensional interpretation of the resistivity distribution, depending on the depth z and the horizontal position x. Appendix B illustrates about the fundamentals of the ERT.

In this work, eight ERT were measured, cumulating *ca*. 10 km. length in two sites. In the first site, in the valley on the mountain, one profile was deployed along the valley and four were orthogonal to the former. In the second site, on the piedmont, three ERT profiles were deployed: one E-W profile from the mountain to the basin, and two N-S profiles, one of them on the mountain and the other on the basin (Figure 1-13).

The electrical measurements were acquired using the multi-electrode device Terrameter LS2. This equipment has 48 electrodes that can be separated every 20 m., having a maximum length of 940 m. The field installation in both sites is shown in Figure 1-13, using the dipole-dipole arrangement. For profiles compounds between two or more lines (each line is 940 m) it was used an overlap of 50% (for example two lines are overlapping 460 m and their total length is 1400 m). Generally, the dipolar distance was 20 m, except in the site 1 B-B' and C-C' profiles where 9 and 7 m were used, respectively.

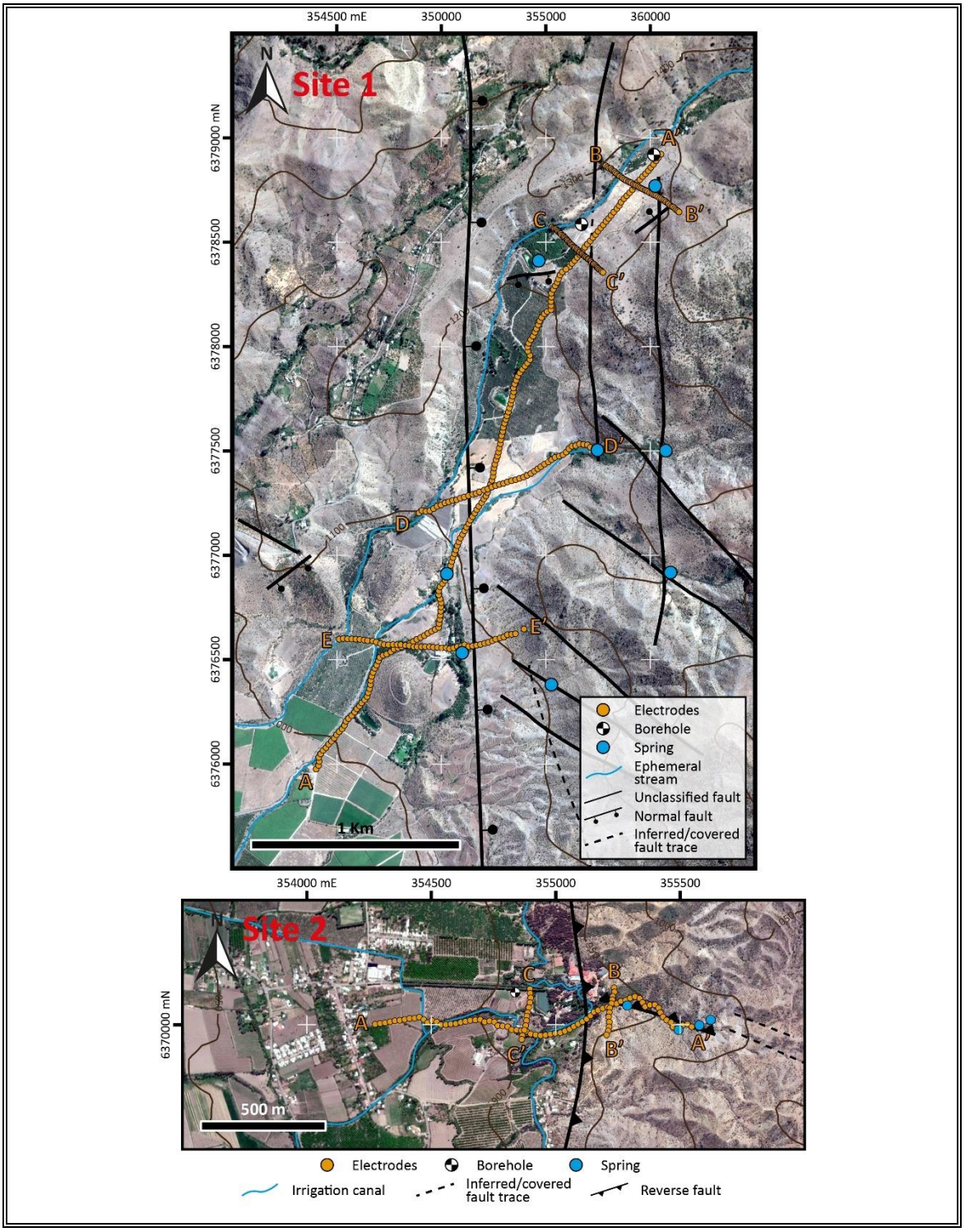

Figure 1-13. ERT locations for site 1 and 2.

Due to topographical irregularities and standard-GPS location inaccuracies of each electrode along the line, geometrical factor misses correct the apparent resistivity at each site. The approach adopted to fix this problem is described in Appendix C (electrode location) and D (recalculate apparent resistivity).

The resistivity modelling was carried out using the software ZonRes2D (Kaminsky 2010), through forward and inverse models, considering different parameters (view in Appendix E). Final resistivity models were obtained by the software Oasis-Montaj to interpolate compound profiles. The analysis of the resistivity models considers a comparison with spring locations, piezometric level in observation boreholes, groundwater electrical conductivity measurements, and geomorphological-geological surveys.

2. ADVANCES IN THE CHARACTERIZATION OF WESTERN ANDEAN FRONT RECHARGE PROCESSES BY A MULTIDISCIPLINARY ANALYSIS (CENTRAL CHILE).

Submitted to Journal of Hydrology (January, 2020).

2.1 Introduction

In arid regions, groundwater plays a key role for the development of socio-economic activities and the increase of human well-being (Scanlon *et al.* 2006; Siebert *et al.* 2010; Gleeson *et al.* 2012). Unlike surface water resources, groundwater resources are less vulnerable to abrupt hydroclimatic changes (*e.g.* drought) and enable to support the water demand during dry periods (Gehrels and Gieske, 2003). But long-term withdrawals exceeding aquifer recharge rates increase the risk of groundwater resource depletions. Sustainable management policies are then necessary to secure over years the different water uses (*e.g.* drinking water supply). But efficient policies depend on a thorough understanding of the functioning of aquifer systems, especially the groundwater recharge processes (Simmers *et al.* 1997; Kresic and Mikszewski, 2012).

In arid mountain ranges, the precipitation increases with elevation and the mountain front zones (transition zone between the mountain range and the downstream alluvial basin) are strategic areas where indirect recharge processes and groundwater circulation feed adjacent alluvial aquifers (Wilson and Guan, 2004; Bresciani *et al.* 2018; Peng *et al.* 2018; Markovich *et al.* 2019). Mountain front zones may contribute up to 50% of the recharge of adjacent alluvial aquifers (Markovich *et al.* 2019). However, due to difficult accesses (irregular topography) and an expected low permeability domain (flows in

fractures), mountain front zones have a lower density of observation boreholes compared to the sedimentary basins. The subsequent lack of hydrogeological information leads to numerous inaccuracies regarding the characterization of hydraulic boundary conditions, which results in an oversimplification of the hydrogeological conceptual models in mountain front and piedmont areas (Viguier *et al.* 2019). Therefore, to cope with the lack of observation boreholes, it is necessary to propose efficient solutions to improve the understanding of hydrogeological systems.

In Central Chile (32°-36°S; Fig. 1a), the hydrogeological studies were exclusively focused on alluvial aquifers contained in Central Depression and valleys (Muñoz *et al.* 2007). According to former studies (DGA, 2015, 2016), the renewal of Central Depression alluvial aquifers would result from river seepage and diffuse infiltration of precipitation. But such hydrogeological view omits potential groundwater resources in adjacent fractured rocks (*e.g.* Principal Cordillera) as well as the existence of mountain block recharge processes originating from the Western Andean Front. Indeed, the Western Andean Front, which separates the Principal Cordillera from the Central Depression by a complex thrust system (Armijo *et al.* 2010; Farias *et al.* 2010), is fixed as a no-flux boundary condition in regional hydrogeological conceptual models (DGA, 2015, 2016). Such oversimplification results from a misunderstanding of the aquifer systems in the Western Andean Front, due to the quasi-absence of observation boreholes in this area. However, in addition to several springs (some of them thermal) located in the Western Andean Front (Hauser 1997; Bustamante *et al.* 2012; Benavente *et al.* 2016), recent studies analyzing the groundwater geochemistry and isotopes (Taucare *et al.* under

revision-a) and the fracture network in the Western Andean Front (Taucare *et al.* under revision-b) reveal that groundwater circulation in the mountain block may recharge the Central Depression aquifers.

Currently, an ongoing depletion of the alluvial aquifers occurs in Central Chile, as a result of the increment of groundwater extraction since the late 1980s (Rivera *et al.* 2016; Valdés-Pineda *et al.* 2014) together with persistent dry years since 2010 (*i.e.* megadrought; Garreaud *et al.* 2017, 2019). Thus, a better characterization of the hydrogeological conceptual models (geometry, boundary conditions and recharge processes) is required in Central Chile, especially between the Andean mountain block and the Central Depression (*i.e.* Western Andean Front). Such characterization will be useful for the water resource stakeholders and the development of groundwater resource sustainable management policies.

Therefore, to overcome the lack of direct observation points, hydrogeological conceptual models must be addressed by indirect surveys. The present study provides an original hydrogeophysical exploration of the Western Andean Front and determines intern geometries, hydrogeological boundary conditions and recharge processes. Present study also presents the analysis of the hydrodynamic behaviour of a perched alluvial aquifer into the Western Andean Front against natural and man-influenced conditions. Through this study we characterize the hydrogeological capacity of the Western Andean Front to be able to transfer groundwater from the Andean mountain block up to alluvial aquifers at the downstream.

2.2 Study Area

The hydrogeological exploration of the Western Andean Front was carried out in the Aconcagua Basin at 32°50'S (Fig. 1a). In this area, the Pocuro Fault Zone shapes the Western Andean Front and separates the Principal Cordillera from the exploited San Felipe Aquifer in the Central Depression (Fig. 1b). We selected this area because it displays both physical settings and water resource issues that are representative of other Western Andean Front areas in Central Chile. The characterization of intern geometries and hydrogeological boundary conditions, at two different sites (*see below*), will enable us to determine the hydrogeological properties and the recharge processes. Such properties and processes are replicable to the rest of the Western Andean Front in Central Chile.

2.2.1 Geological setting

The Andean mountain range results from the crust shortening related to the subduction of the Nazca Plate beneath the South American Plate, since the Jurassic to the present day (Coira *et al.* 1982; Mpodozis and Ramos, 1989; Charrier *et al.* 2007; De Celles *et al.* 2009). In Central Chile (32°-36°S), the Andean orogenesis has been developed through several NS oriented crustal faults (*e.g.* Pocuro Fault Zone) and controlled by inherited oblique basement faults (Giambiagi *et al.* 2003; Cembrano *et al.* 2007; Piquer *et al.* 2017). Central Chile is divided in three major continental domains, from West to East (Fig. 1a): The Coastal Cordillera that rises up to 2000 m a.s.l, the Central Depression with an average elevation of ~550 m a.s.l and the Principal Cordillera with highs rising up to 5000-6000 m a.s.l. This morphotectonic setting ends from 33°S northward (Fig. 1a) due

to the change of subduction angle leading to an absence of the Central Depression and active volcanism between 28°-33°S (Yáñez *et al.* 2001, 2002; Yáñez and Cembrano, 2004; Tassara *et al.* 2006).

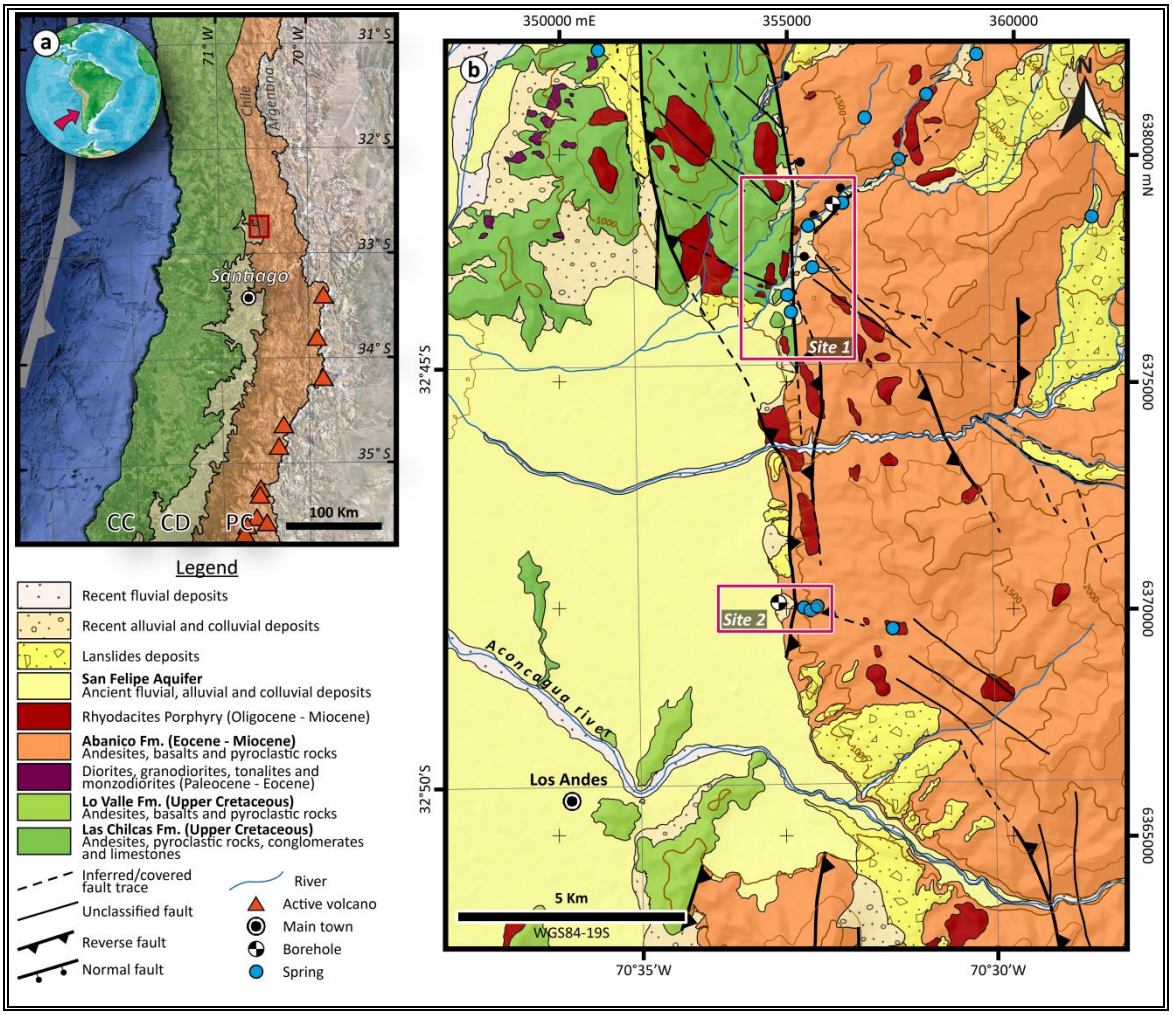

Figure 2-1. a) Localization of the study area (red area) in Central Chile and the main Andean morphotectonic domains: Coastal Cordillera (CC), Central Depression (CD) and the Principal Cordillera (PC). b) Geological map of the study area (after Rivano *et al.* 1993; Jara and Charrier, 2014; Boyce, 2015) and the study sites. Mapped fault belongs to the PFZ.

In the study area (Fig. 1b), the Coastal Cordillera is made up of Late Cretaceous volcano-sedimentary sequences (Las Chilcas and Lo Valle Fm.) locally intruded by coeval plutonic rocks (Wall *et al.* 1999; Boyce, 2015). The Central Depression is filled by ca. 350 m of Quaternary alluvial deposits (Yañez *et al.* 2015). The Principal Cordillera is composed by folded and fractured Eocene-Miocene volcano-sedimentary sequences (Abanico and Farellones Fm.) deposited in the paleo Abanico Basin. Those sequences are locally intruded by Oligo-Miocene plutonic rhyodacites (Fuentes *et al.* 2002, 2004; Jara and Charrier, 2014; Piquer *et al.* 2017). The West Vergent Thrust System in the study area is represented by the Pocuro Fault Zone (PFZ; Carter and Aguirre, 1965). PFZ is a NS brittle deformation zone of 150 km long and 4 km wide, which records different tectonic events resulting in a well-connected fractured network (Taucare *et al.* under revision-b). Those tectonic events are related to the extension of the Abanico basin during the Eocene-Oligocene periods and to the inversion of the Abanico basin between the Miocene and the early Pliocene (Godoy *et al.* 1999; Jordan *et al.* 2001; Charrier *et al.* 2002).

2.2.2 Hydroclimate and hydrogeological settings

In the Aconcagua Basin, which is one of the major basins of Central Chile (7300 km^2), the climate is semi-arid and displays historic mean annual precipitation (1960-2010) averaging ~280 mm/yr in the Central Depression and ~620 mm/yr in the Principal Cordillera (DGA, 2019). Most of precipitation occurs during the austral winter and are related to wet fluxes originating from the Pacific Ocean (Fig. 2a and 2b; Barret *et al.* 2009). The interannual variability is governed by ENSO (El Niño Southern Oscillations):

wet and dry periods occur during La Niña phases and El Niño, respectively (Fig. 2a; Montecinos and Aceituno, 2003). During dry periods, the perennial discharge in the Aconcagua River is supported by snowmelt in highs (Waylen and Caviedes, 1990; Cortés *et al.* 2011, Ohlanders *et al.* 2013) and groundwater discharge.

But due to an uninterrupted sequence of dry years since 2010, classified as "megadrought" and uncorrelated with the ENSO (Fig. 2a and 2b), the mean annual precipitation rates dropped by around 30% (Boisier *et al.* 2016; Garreaud *et al.* 2017). This impacted the availability (up to -90%) of surface-water resources in Central Chile (Boisier *et al.* 2016; Garreaud *et al.* 2017). To support the intensive agriculture activities, groundwater extraction in the Central Depression from the Quaternary alluvial San Felipe Aquifer increased by ~200% between 2010 and 2020 triggering an alarming decline of the groundwater levels (Fig. 2c and 2d). San Felipe Aquifer was classified as a restricted area since 2011 (Valdés-Pineda *et al.* 2014), highlighting the strong risk of aquifer depletion. According to regional conceptual models (DGA, 2015, 2016), the recharge of San Felipe Aquifer exclusively originates from the Aconcagua river seepage and the direct infiltration of rain. The PFZ is fixed as a no-flux boundary condition. But in the Western Andean Front, perennial springs with a low thermal component have been described a few decades ago (Darwin 1939; Hauser, 1997; Bustamante *et al.* 2012; Benavente *et al.* 2016). These springs outflow from fractured rocks and suggest the existence of groundwater circulation into the mountain block (Taucare *et al.* under revision-a,b). In the Western Andean Front, low-discharge springs (~1.0 L/s) are locally used for agriculture and

drinking water purposes, while high-discharge springs (~4.0 L/s at Jahuel) are used for thermal baths and mineral water bottling.

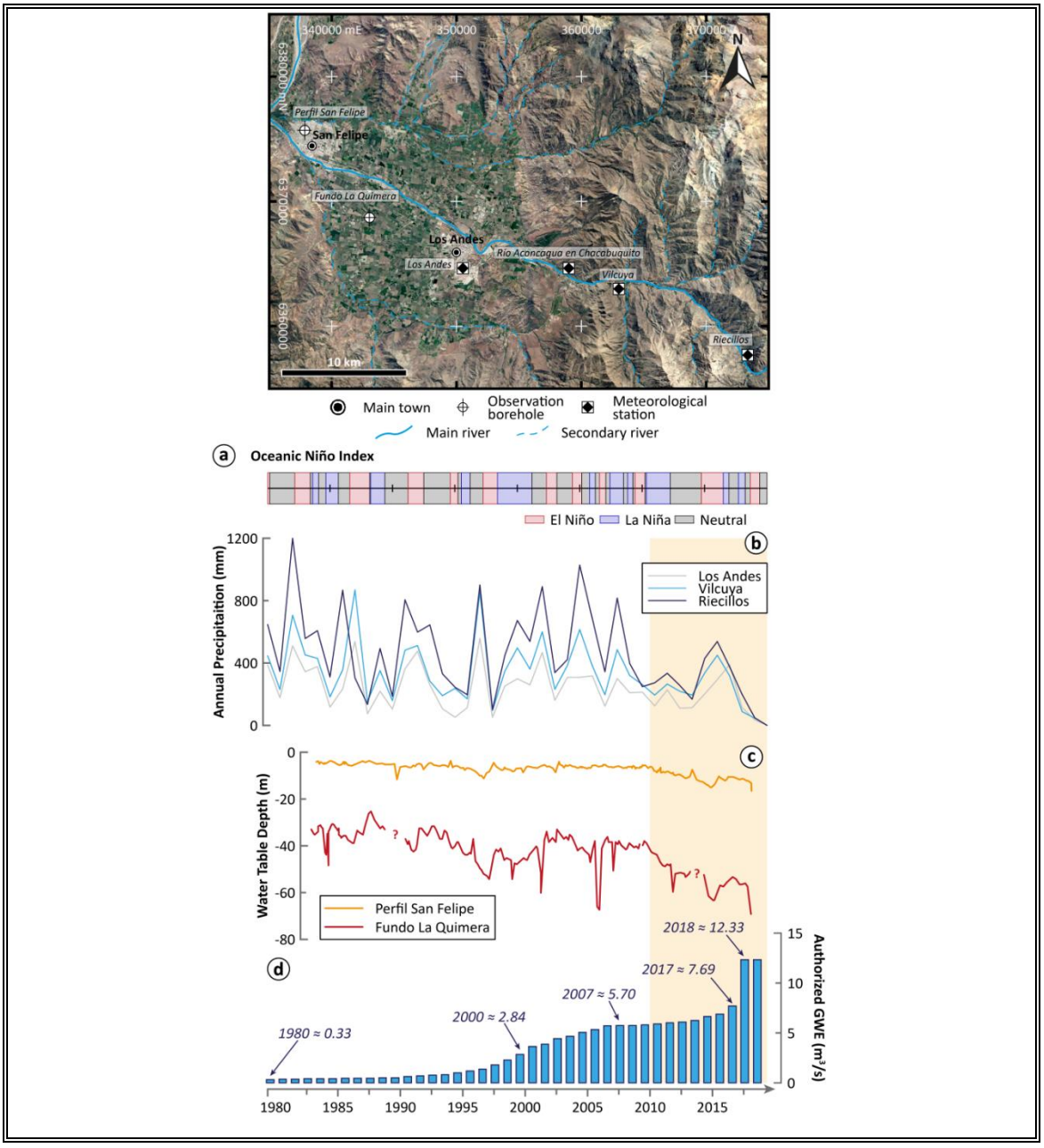

Figure 2-2. Location of meteorological station and observation boreholes in the Aconcagua Basin. a) Oceanic Niño Index (NOAA/National Weather Service, 2019; http://origin.cpc.ncep.noaa.gov/products/analysis_monitoring/ensostuff/ONI_v5.php) b) Annual precipitation at "Los Andes" (820 m a.s.l.), "Vilcuya" (1100 m a.s.l.) and "Riecillos" (1290 m a.s.l.) meteorological stations. c) Water table variation at the "Perfil San Felipe" (634 m a.s.l.) and "Fundo La Quimera" (704 m a.s.l.) observation boreholes. d) Authorized groundwater extraction in the San Felipe aquifer. In pale orange is highlighted the "Megadrought" of Central Chile. b), c), and d) available data at DGA web site (DGA, 2019).

2.2.3 Study sites

To explore the hydrogeological setting of the Western Andean Front at Aconcagua Basin, measurements and interpretations were focused in two sites within the PFZ, which were selected according to their respective geomorphological peculiarities (Fig 2-1):

- Site 1 is a NE-SW oriented perched valley located into the PFZ (Fig. 1b and 3a). It is limited by Las Chilcas Fm. to the West and the Abanico Fm. to the East. A major NS oriented normal fault and secondary NW-SE and NE-SW oriented faults, identified during field surveys, have likely contributed to shape the valley morphology. The drainage system is composed by a principal longitudinal gully (ephemeral stream) connected with several lateral gullies coming from adjacent highs. Ephemeral streams are fed by precipitation runoff and snowmelt. In addition, at least 8 perennial springs outflow (0.2-2.0 L/s) from the fractured volcano-sedimentary rocks of Abanico Fm. at the eastern side of the valley. There is one borehole in alluvial deposits (Fig. 2-3b) with water table depth measured at 20 m below the ground surface on September 2018. The water table variations and atmospheric pressures were recorded to characterize the hydrodynamic behavior of groundwater in the alluvial deposits of the perched valley (*see Sect. 3.4*). The electrical conductivity of groundwater range from 460 to 580 μS/cm (17.0-21.0 ohm-m) with temperature between 21 and 26°C in springs, while in the borehole is 410 μS/cm (24.5 ohm-m) and 17°C, respectively. Note that mean annual air temperature in the study area is 15°C.

- Site 2 is an abrupt transition zone between the fractured rocks of the Abanico Fm. to the East and a paleo-alluvial fan to the West (Fig. 2-3c and 2-3d). The abrupt transition between the alluvial basin and the fractured hard rocks is a major NS oriented reverse fault, expressed at the ground surface by a knickpoint of 5 m high. Four perennial springs (~0.2 L/s) outflow from fractured rock along a N70W oriented reverse fault. The electrical conductivity of groundwater ranges from 400 to 580 μS/cm (17.0-25.0 ohm-m) with temperatures between 20° to 24°C. Also, a borehole of 145 m depth is located in the paleo-alluvial fan to the West of the main NS fault. Water table depth averaged 100 m below ground surface in 2018 (it was not possible install a water level probe in this borehole). The measured electrical conductivity in groundwater 700 μS/cm (14.3 ohm-m) at 18.6 °C, respectively. In addition, irrigation canals conducting water from the Principal Cordillera up to agriculture fields in the Central Depression about 50 m to the observation borehole.

Figure 2-3. Photographs of the study sites. a) Panoramic view of the perched valley, and b) a borehole located at the bottom of the valley in the alluvial deposits. c) Panoramic view of the contact between the Principal Cordillera and the Central Depression, to the East and to the West of the reverse fault, respectively. d) Typical outcrop of NS reverse faults in the PFZ.

2.3 Methodology

To assess the influence of the geometry and boundary conditions of PFZ on the groundwater flows - and cope with the low density of observation points - we used a multidisciplinary approach based on hydrogeophysical and hydrogeological exploration of the Western Andean Front (Fig. 2-4).

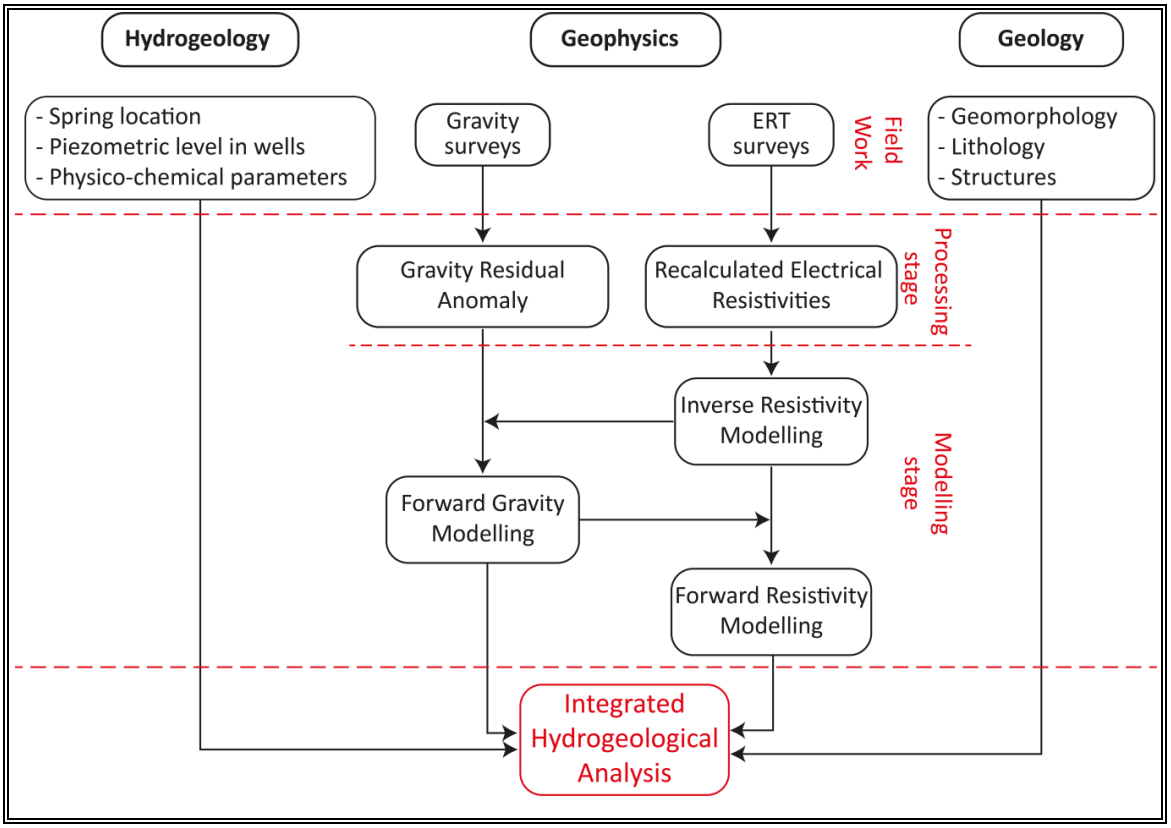

Figure 2-4. Methodology flow chart. Dotted red lines separated the different stages: field work, processing and modelling stages.

2.3.1 Geophysical field surveys

Geophysical surveys were completed by gravimetric and geoelectrical analyses.

On one hand, the gravimetric method is a simple and economical technique that enables the delineation of the contact between the basement and the overlaying alluvial deposits, due to gravity variations associated to density contrast between both domains (Telford *et al.* 1990; Murty and Raghavan, 2002; Stěpančíkova *et al.* 2011; Yañez *et al.* 2015; Estay *et al.* 2016). We carried out the gravity measurements using a Scintrex-CG5 relative-gravimeter (5 µGal resolution) together with a differential GPS Trimble R4 for precising the location of each measurement point (< 15 cm of lateral and vertical uncertainties). We performed 460 measurements spaced from 50 to 100 m apart and distributed on 4 profiles of 2-3 km long in PFZ.

On the other hand, the geoelectrical analysis has been widely used in hydrogeology to characterize the aquifer geometry, main lithological variations and water table extent (Guérin *et al.* 2001; Francese *et al.* 2009; Ball *et al.* 2010; Boiero *et al.* 2010; Descloitres *et al.* 2013; Casado *et al.* 2015; Kazakis *et al.* 2016; Viguier *et al.* 2018; Avilés *et al.* 2020; Carriere *et al.* 2020). We conducted the electrical resistivity surveys using the Terrameter LS2 resistivity meter (resolution 3 nV) of 48 channels (stainless-steel electrodes) and 4 simultaneous readings. Geoelectrical profiles were realized using a dipole-dipole measurement setting with the maximum length configuration: 940 m long with electrode spacing of 20 m. We realized at Site 1 one ~3400 m long longitudinal profile (composed of seven profiles with 50% of overlap) and four transversal profiles; and at Site 2 one

~1500 m long profile (composed of two profiles with 50% of overlap) and two transversal profiles.

2.3.2 Processing stages

Gravity and electrical resistivity measurements were processed to obtain the gravity residual anomalies (i) and the recalculated apparent resistivities (ii), respectively (Fig. 2-4):

(i) Gravity data were processed according to the standard procedure described in Telford *et al.* (1990), including corrections for tidal variations given by the gravimeter and instrumental drift by means a fix base station at Los Andes town in the Central Depression. Absolute gravity values were obtained by translating the base station at *Pontificia Universidad Católica de Chile*, in Santiago de Chile (979405.513 mGal; 33°29'57.49" S; 70°36'52.66" W). Latitude correction was realized using the WGS84 reference ellipsoid model. We realized the Free Air, Bouguer and Terrain corrections using the altitude from GPS data (WGS84 Datum). Also, for Bouguer and Terrain corrections we considered a mean density of 2.67 g/cm^3. In addition, for the Terrain correction we used a digital elevation model with 12.5 m resolution (obtained from https://www.asf.alaska.edu/). Then, to get the gravity residual anomalies from the previous corrected signal (*see above*), we removed the regional gravity field caused by the isostatic compensation of Andean crust (Tassara *et al.* 2006).

(ii) About the electrical resistivity data, the pre-processing phase consisted to remove values of apparent resistivity with an error greater than 50% of the standard deviation (higher errors are associated with outliers compared to the neighbour resistivity). Then,

due to the geographic irregularities that prevented straight profiles in the field, apparent resistivity was recalculated according to each transmitter-receptor dipole configuration (Fig. 2-5a and 2-5b). The geometrical factor was recalculated using the real location of each electrode (Fig. 2-5c) as well as the location of each measurement point because the current circulation is neither symmetric nor 2D. Then, according to the spatial distribution of all measurement points along a profile, these latter were projected on a straight line by means of an adjustment of minimum squares for a later modelling as 2D section.

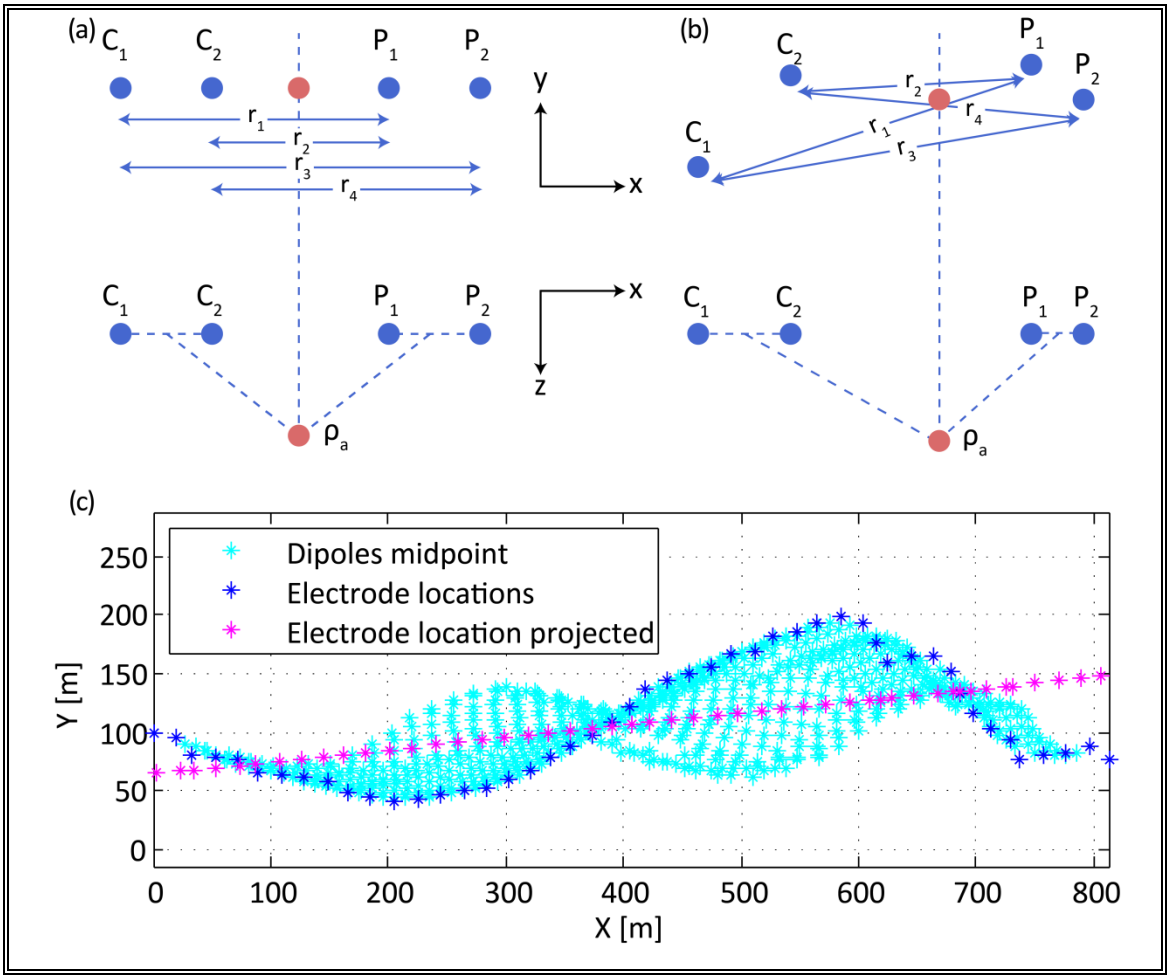

Figure 2-5. a) and b) show the dipole-dipole setting for ERT where C_1 and C_2 represent current electrodes, P_1 and P_2 are potential electrodes, and ρ_a is the location of the apparent resistivity measurement. a) Represents an ideal situation where electrodes are aligned and equidistant, while b) represents a real situation where electrodes are not aligned, nor equidistant. c) An example of irregularly traced profile, where cyan points represent the location of resistivity measurements.

2.3.3 Modelling stages

For data modelling we proceed in the following order (Fig. 2-4):

(i) First resistivity sections were obtained by inverse modelling of previously recalculated apparent resistivities (*see Sect. 3.2*). We used the code ZonRes2D (Kaminsky,

2010) numerical modelling of resistivity, which minimizes an objective function according the misfit between measurements and the model response, also a factor that regulate the mathematical solution favouring smooth models.

(ii) The alluvial sediment thickness and basement geometry were characterized through a forward modelling of the previously calculated gravity residual anomalies (*see Sect. 3.2*). Gravity modelling was completed using ModelVision software. The contact depth between sedimentary deposits and basement rocks depends on the density contrast between both domains. An appropriate density contrast was calculated through an iterative process comparing the model responses with the gravity residual anomalies. In the study area, basement density averages 2.54 g/cm^3 and 2.62 g/cm^3, for Abanico Fm. and Las Chilcas Fm., respectively (Bustamante *et al.* 2012). At Site 2, the basement is only composed of Abanico Fm. unlike at Site 1. Thus, the value of density contrast was characterized first at Site 2. It was constrained by a first estimation of the basement geometry resulting from inverse resistivity models (Fig. 2-4). We found that the most suitable density contrast is 0.50 g/cm^3 (sedimentary deposits and volcanic rock). As a result, the sediment density values range between 2.04 and 2.11 g/cm3 in agreement with the results of the Santiago Basin that is also composed of well stratified and unconsolidated coarse sands and silts (Yáñez *et al.* 2015). We assumed a similar density contrast (0.50 g/cm^3) over the whole study area for modelling other profiles.

(iii) Finally, the resistivity profiles were obtained through the forward modelling of the first resistivity sections (obtained by inverse modelling, *see above*). The apparent resistivities derived from the forward models were compared to the recalculated apparent

resistivities (*see Sect. 3.2*) for validating the forward models. The related RMS errors range between 5.0% and 11.8%. Although forward models are not typical for hydrogeological purposes, they are useful to consider known geometric features (e.g. faults), unlike inverse models that are exclusively based on the resistivity surveys and do not consider known geological features. Indeed, geological field observations and gravity models were used to constrain the forward resistivity modelling, especially the fault orientations (*see example in* Fig. 2-6).

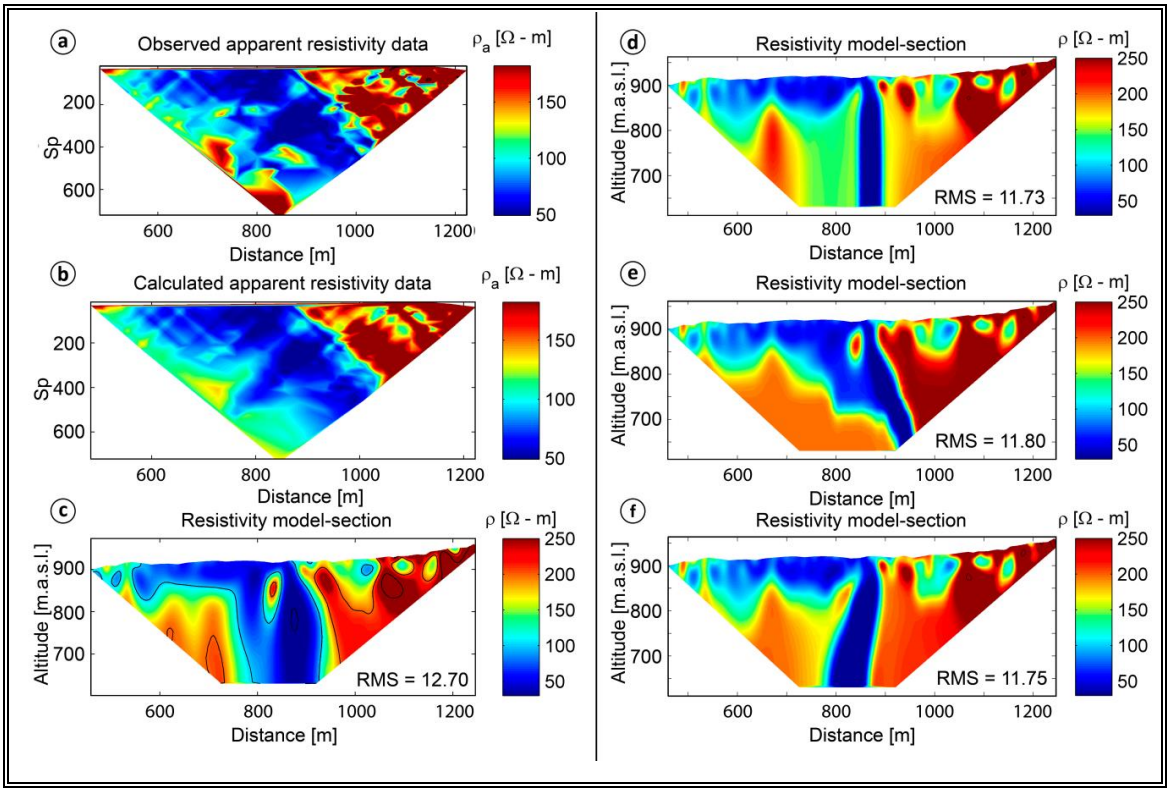

Figure 2-6. Examples of resistivity modelling. The left panel shows an inversion model where a) observed data, b) calculated data, and c) resistivity model-section. The right panel shows different forward models considering d) a vertical low resistivity band e), a subvertical dip east band, and f) a subvertical dip west band.

2.3.4 Hydrodynamic analyses

To characterize the behavior of groundwater resources in the alluvial infilling within the PFZ, we measured for 9 months (from October 2018 to June 2019) the water table variations (m a.s.l) in the unconfined alluvial aquifer of the perched valley at Site 1 (Fig. 2-3b). This latter is usually exploited for irrigation purposes. Water table variations were monitored in a well of 27 m total depth (Fig. 2-3b), located at 1284 m a.s.l (groundsurface), by a water-level pressure probe (levelogger Solinst) installed in the well at 24 m b.g.s (1260 m a.s.l). Water table variations were corrected by a barometric pressure probe (barologer Solinst) with a synchronized time-step of 10 min. In-situ pumping and local precipitation changes were considered for analyzing the behavior of groundwater resources in natural and human-influenced conditions. Due to the absence of meteorological station in the study area, we used as proxy the daily precipitation records of the "Rio Aconcagua en Chacabuquito" (hereafter RAC) meteorological station (*www.dga.cl*) located at 950 m a.s.l (Fig 2-2). Groundwater recharge triggered by precipitation events was estimated at different timescales (event, short-term and longer-term timescales) under natural transient state, through the analysis of the water table variations (Scanlon *et al.* 2002; Healy and Scanlon, 2010). Used specific yield ranges between 0.08 and 0.2 for silt and fine sand, respectively (Johnson, 1967). In addition, we performed a single well pumping test during ~7 hr for estimating the transmissivity in the unconfined alluvial aquifer at Site 1 (Fig. 2-3b), with a controlled steady-pumping rate of 4.79 m^3/h.

2.4 Results and Discussion

2.4.1 Basement and alluvial cover geometries derived from gravity analysis

Along gravity profiles (Fig. 2-7), the observed variations of residual gravity anomaly correspond to mass defect resulting from thickness variations of the unconsolidated alluvial deposits above the basement (i.e. Abanico Fm. and Las Chilcas Fm.). The more negative the residual anomaly, the greater the thickness of alluvial deposits.

At Site 1, a perched valley into the Western Andean Front (Fig. 2-1b), the AA' profile shows a negative residual gravity anomaly (up to -1.1 mGal) over the entire profile length (~ 3 km) and does not show a major amplitude signal. Modelling results reveal that the alluvial cover is continued from the upstream part of the perched valley up to the Central Depression at the downstream. But, the thickness of alluvial deposits is highly variable (from a few meters up to 50 m thick) due to irregular basement geometry, which likely results from the presence of faults (Fig. 2-7). Please note also that the location of some springs coincides with basement highs and thin alluvial cover thickness, which suggests the lower permeability of the basement compared to the alluvial cover.

At Site 2, located above the major NS oriented reverse fault of PFZ (Fig. 2-1b), the DD' profile displays significant residual gravity anomaly variations, which are strongly similar to those observed on the other areas of the reverse fault (see BB' and CC' profiles in Fig. 2-7). The residual gravity anomaly tends to be null to the East of the reverse fault, abruptly decreases at the level of the fault and is negative (from -1 to -3.5 mGal) in the paleo-alluvial fan to the West. Results from modelling validate in depth the major NS

oriented reverse fault of PFZ. In addition, they indicate that there is a thick depocenter of unconsolidated alluvial deposits, on the west side of the fault trace. The basement geometry is relatively smooth at BB' and CC' profiles and the sedimentary infilling ranges between 150 and 200 m thick. Contrariwise, the DD' profile (Site 2) shows an irregular and abrupt variations of the basement geometry and the sedimentary infilling thickness (between 50 to 180 m). Such changes let supposing that PFZ is shaped by a segmented fault with differential uplifts impacting the basement geometry at depth like proposed further south for the San Ramon Fault in the Santiago area (Estay et al. 2016).

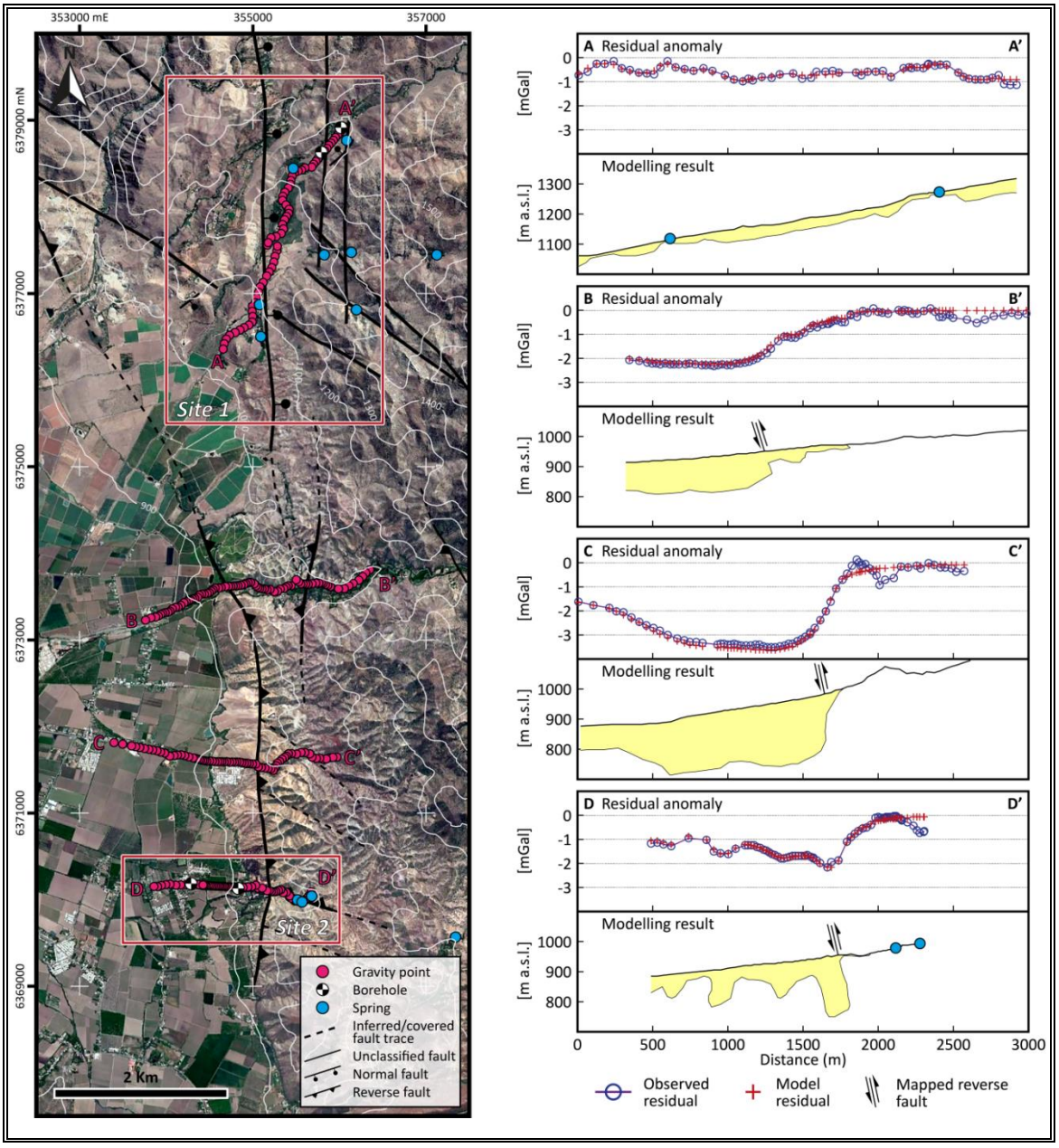

Figure 2-7. Left panel, satellite map showing the trace of each gravity profile in pink, the red squares are sites with geoelectrical data. Right panel, gravity profiles and model response (upper panel) and their corresponding inverse model (lower panel).

2.4.2 Hydraulic setting inferred from geoelectrical analysis

2.4.2.1 Geoelectrical domains

By analyzing electrical resistivities at sites 1 (Fig. 2-8) and 2 (Fig. 2-9), we identify different geoelectrical domains in terms of resistivity values that range from 7 up to 500 Ω-m. Considering the low range of electrical resistivity in groundwater (17-25 Ω-m), we assume that observed variations of electrical resistivity result from geological features in the PFZ. At both sites, the alluvial infilling contrasts with the underneath and irregular basement, which are illustrated by a conductive (from 50 up to 100 Ω-m) and a resistive domain (> 200 Ω-m), respectively. The intermediate domain (~150 Ω-m) suggests a geoelectrical transition layer, likely due to a higher weathering of the fractured basement. In addition, contrasting with the surrounding domain, well-defined low resistivity subvertical bands (LRSBs) are observed on the electrical resistivity profiles (Fig. 2-8 and 2-9).

For different domains we estimate the total porosity using the Archie's Law under saturated condition (Eq. 1) (Archie, 1942).

$$\rho_m = a \cdot \phi^{-m} \cdot \rho_w \qquad \text{(Eq.1)}$$

Where ρm and ϕ is the electrical resistivity and the total porosity of the medium, respectively. ρw is the electrical resistivity of groundwater. Both a and m are constant lithology-related parameters. Mean groundwater resistivity is 20 Ω-m in the study area. For alluvial infilling, we considered a = 0.88 and m = 1.37 (Keller, 1988). Total porosity value of the alluvial infilling ranges between 0.28 and 0.47. For the fractured basement,

we considered a = 0.62 and m = 1.95 (Keller, 1988). Total porosity of the fractured and fractured-weathered basement ranges between 0.24-0.34 and 0.15-0.24, respectively. The total porosity results appear to be overestimated while the lower limit of the porosity range seems to be more representative compared to the literature The total porosity results appear to be overestimated while the lower limit of porosity range seems to be more representative compared to the literature (Banton and Bangoy, 1997).

2.4.2.2 Geoelectrical analysis at Site 1

At Site 1 (Fig. 8), the longitudinal profile (AA' in Fig. 2-8) shows an irregular thickness of the alluvial deposits along the perched valley. Due to faults-related basement elevation variations, the alluvial cover appears to be discontinued along the perched valley. But thanks to transverse profiles (BB'; CC'; DD'; EE' in Fig. 2-8), we note a continuity of the alluvial cover along the ephemeral stream. The stream alluvial corridor constitutes a hydraulic continuity of high permeability, which enables the groundwater circulation from the upstream part of the perched valley up to the San Felipe Aquifer in the Central Depression.

Regarding the geological features producing LRSBs on electrical resistivity profiles, we observe that the main NS oriented normal fault (mapped in the field) coincides with LRSBs on the DD' profile at 350 m (~ 150 Ω-m), EE' profile at 650 m (~ 60 Ω-m) and AA' profile at 1250 m (~ 75 Ω-m) (Fig. 8). Moreover, other LRSBs are visible on the BB' profile at 280 m (< 20 Ω-m), AA' profile at 2800 m (< 20 Ω-m), and CC' profile at 100 m and 275 m (< 20 Ω-m), and are also topologically associated with major NS oriented alignments (Fig. 2-8). Finally, all identified LRSBs coincide with NS oriented structures,

such as faults and alignments that were identified by field mapping and satellite views analyses, respectively (Fig. 2-8). Outcrop surveys allowed validating that low resistivity values in the LRSBs are due to clay-rich fault gouges and related structures as well as to hydrothermal weathering-derived clay-minerals (e.g. laumontite, goethite), such as observed in fault zones (Fig. 2-10a). Because clay in saturated conditions has typical electrical resistivity values lower than 20 Ω -m (e.g. Descloitres *et al.* 2013), the observed variations of resistivity values in LRSBs (from < 20 up to 150 Ω-m) may be due to local differences of clay-enrichment into the core-zones.

In addition, in the eastern side of the perched valley, we note that springs outflowing from the fractured Abanico Fm are topologically associated with the intersection of NS oriented faults with oblique basement faults (Fig. 2-8). Within the fractured basement, groundwater appears to be drained within oblique basement faults (high-transmissivity axes) and then limited by NS oriented faults. These latter are sealed by a clay-enrichment and act as hydraulic barriers. Both fault systems control the groundwater circulation within the basement at PFZ.

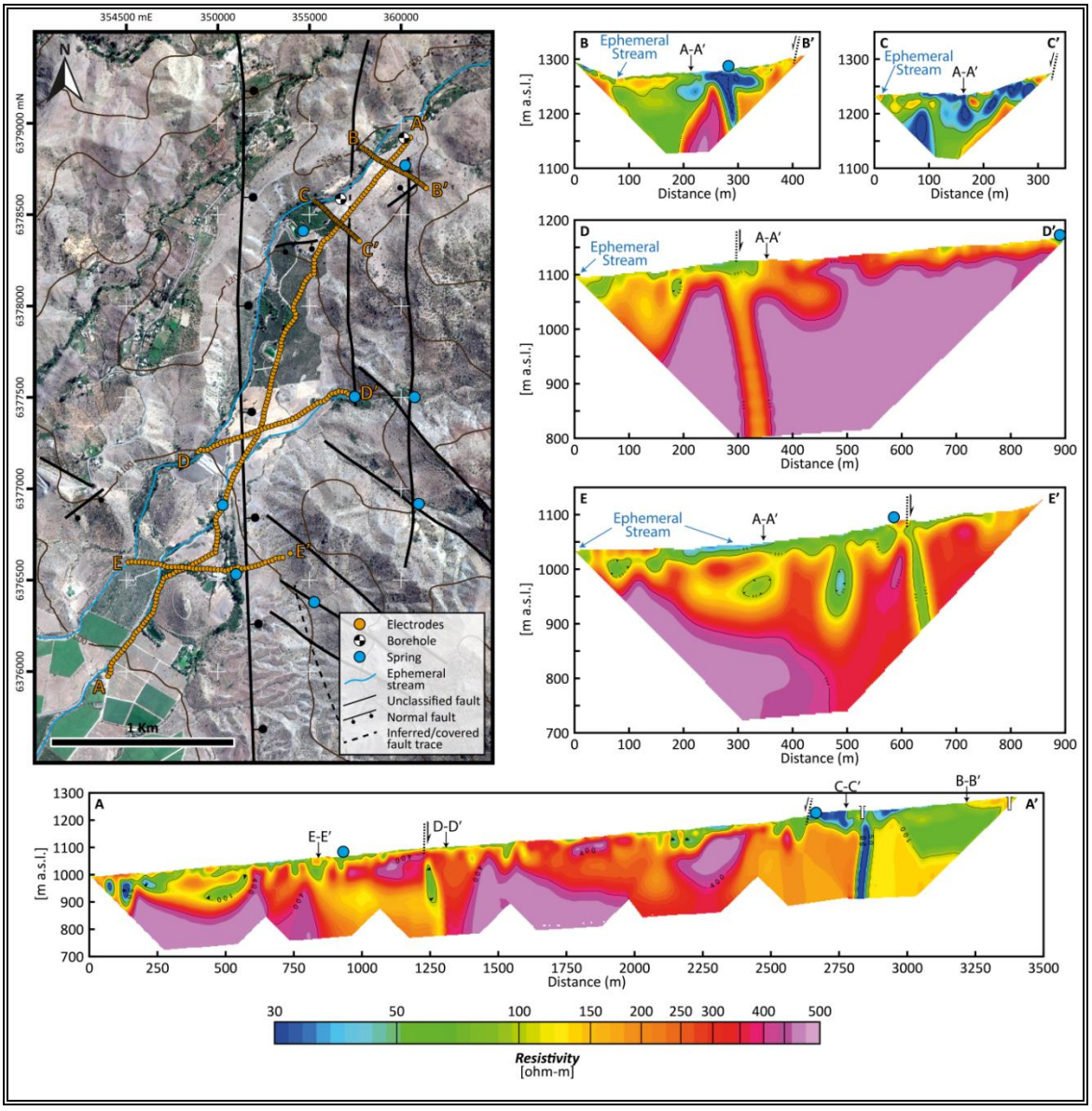

Figure 2-8. Site 1, satellite map with main faults, spring and geoelectrical profiles. Resistivity models of each profile. Every intersection between profiles is marked. Faults, stream and spring are also projected in its corresponding profile.

2.4.2.3 Geoelectrical analysis at Site 2

At Site 2 (Fig. 2-9), the longitudinal (AA') and transverse (BB' and CC') profiles (Fig. 2-9) show an absence of alluvial deposits to the East of the mapped reverse fault, and a variable alluvial infilling (from 50 up to 200 m) above the irregular basement paleosurface

to the West. These results agree with previous gravity modeling (DD' profile in Fig. 2-7). Within the alluvial infilling, we observe two low resistivity plumes (~ 40 Ω-m) underneath irrigation canals. Such plumes reveal the localized infiltration of surface-water driven in irrigation canals but also its role in the recharge of the San Felipe Aquifer. Considering the groundwater level and the borehole position (Fig. 2-9), we assume that a part of the pumped groundwater originated from irrigation canal losses.

The difference of resistivity values on both sides of the mapped reverse fault seems resulting from a weathering difference of the fractured basement likely due to fault influences. Indeed, two LRSBs are visible on the AA' profile at 525 m (~ 20-75 Ω-m) and at 950 m (< 15 Ω-m) (Fig. 2-9). This latter LRSB coincides with the main NS oriented reverse fault (Fig. 2-9). As validated at Site 1, we assume that the low resistivity value is due to the clay-enrichment of the core-zone. So far, only this main reverse fault separating the mountain block from the Central Depression was identified (Fig. 2-1b). But the AA' profile permits evidencing another fault below the alluvial cover (Fig. 2-9), which displays a similar geoelectrical response like other NS oriented faults. Current information does not allow establishing neither the fault kinematic nor its activity time (Eocene-Oligocene extensive or Miocene-Pliocene compressive phases).

About a hydrogeological point of view, those NS oriented faults seem acting as hydraulic barriers that limit the groundwater circulation originating from the mountain block. Indeed, several perennial springs are localized to the upstream of the intersection between a NS oriented fault and an oblique basement fault (Fig. 2-9). Despite we observed in the field the presence of this oblique basement fault, it is not visible on the BB' and

CC’ geoelectrical profiles (Fig. 2-9). Oblique basement faults are discrete fault planes, driving groundwater and without clay presence (Fig. 2-10b). Nevertheless, the resolution of geoelectrical survey does not permit to detect those discrete structures. At Site 2, the low resistivity values and the location of springs highlight the impervious hydraulic property of the NS oriented faults, as a result of the clay-rich core-zones. Like observed at Site 1, fault systems governed the groundwater circulation in the basement at PFZ.

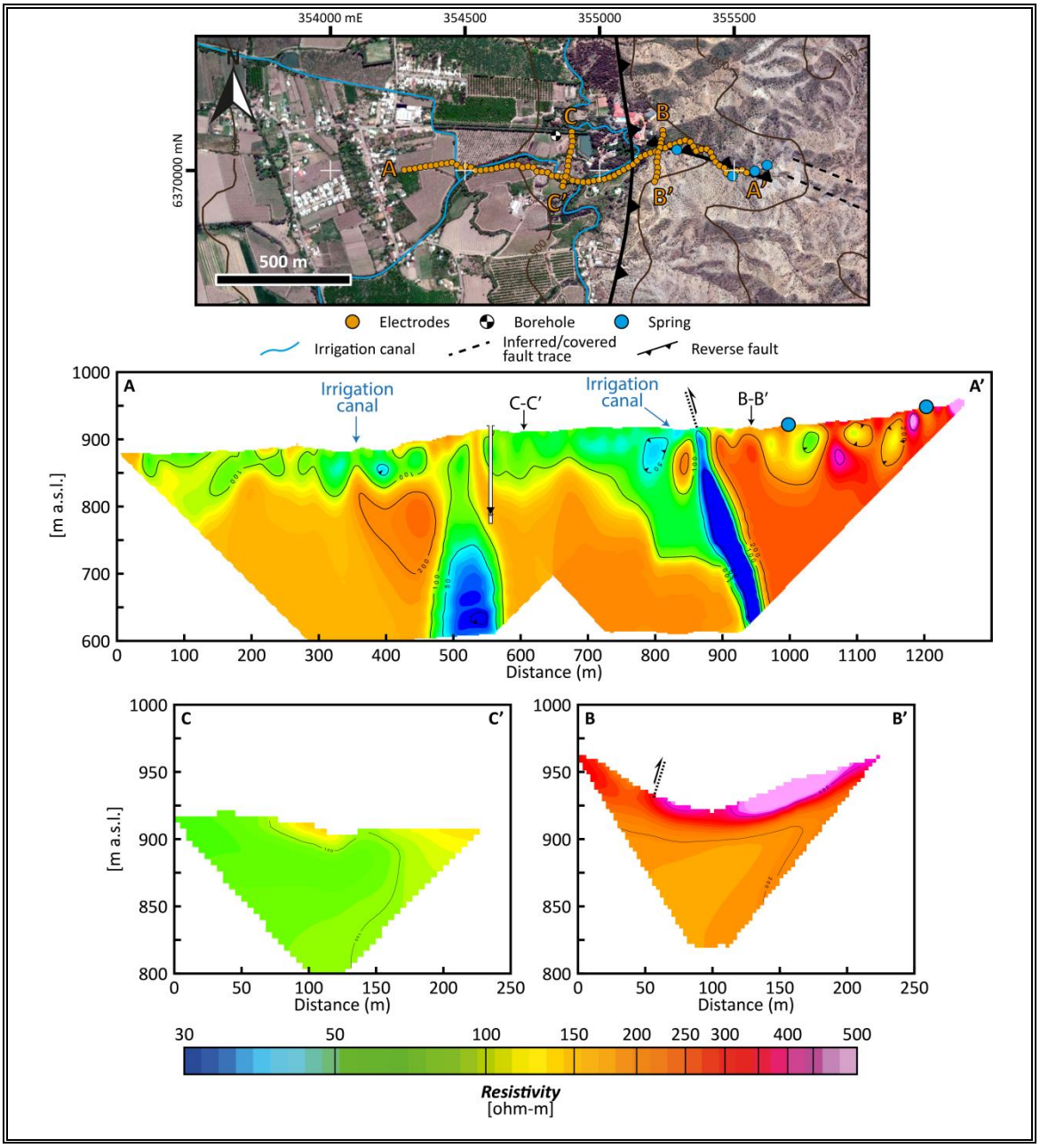

Figure 2-9. Site 2, satellite map with main faults, spring and geoelectrical profiles. Resistivity models of each profile. Every intersection between profiles is marked. Faults, irrigation canal and spring are also projected in its corresponding profile.

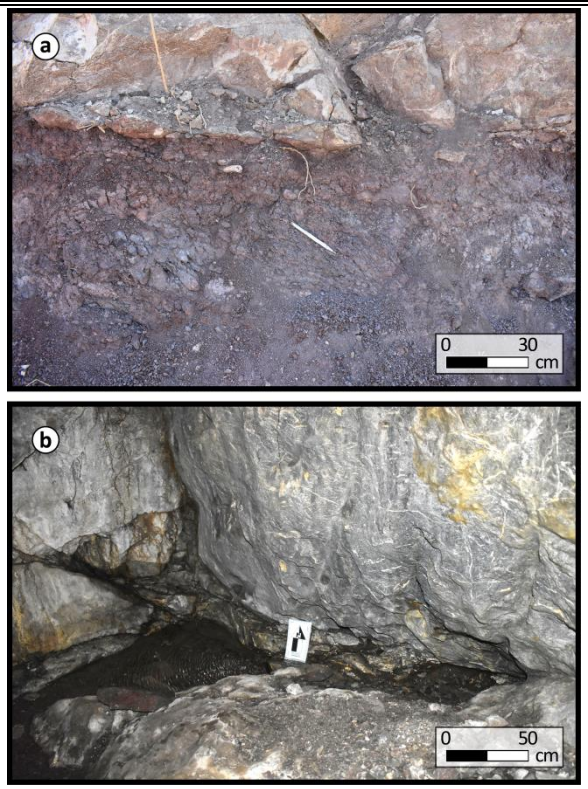

Figure 2-10. a) Evidence of gouge clay-rich fault in PFZ at Site 1. b) Spring outflowing from a discrete plane of oblique basement fault within the Abanico Fm. in PFZ.

2.4.3 Hydrodynamic analyses and recharge estimating

Water table variations in the unconfined alluvial aquifer of the perched valley at Site 1 (Fig. 2-3b) show two subperiods (Fig. 2-11a). The first subperiod (Fig 2-11a) is characterized by a natural transient state with at least 19 occasional short-term pumping and recharge events caused by precipitation (Fig. 2-11b). The second one is characterized by a man-influenced transient state that results from a long-term pumping (~5 m3/h) for irrigation purposes during the austral summer (Fig. 2-11a). This uninterrupted pumping caused an abrupt water table decline resulting in a measured water table drawdown of 3.5 m in 87 days. Given that water table dropped under 1260 m a.s.l (probe elevation), real

drawdown has not been recorded. Occasional water table rises, observed since April 2019, were caused by power interruptions. The observed behavior allows highlighting the high vulnerability of alluvial aquifers in the perched valley against excessive withdrawals, especially during uninterrupted dry years where the precipitation-related recharge is declining.

During the first subperiod (Fig. 2-11b), recorded water table rises coincide with precipitation events at RAC meteorological station (used as proxy) (Fig. 2-2). In addition to groundwater arrivals from the fractured bedrock and oblique basement faults, alluvial aquifer recharge in the perched valley is mainly governed by focused indirect recharge processes triggered by runoff infiltration in ephemeral stream (or gully) coarse deposits (Fig. 2-3b). We analyze at different timescales the recharge events that occurred between October 10th and 20th, after a total precipitation events of 24 mm (Fig. 2-11b). Resulting from two distinct rainstorms in the Western Andean Front, two recharge events are visible. At the event timescale, recharge rates range from 8.1 to 22.6 mm/d (Fig. 2-11b). Considering the two events as one, the recharge rate ranges from 4.2 to 10.4 mm/d at a short-term timescale. At a longer-term timescale (suitable for water resource management), we estimate that groundwater recharge in the alluvial aquifer of the perched valley is between 1.2 and 2.9 mm/d.

Focused indirect recharge rates correspond to 5% and 12% of the precipitation of the rainy events. In general, the ratio between the focused indirect recharge and the precipitation is higher than that between the long-term diffuse recharge and the precipitation (< 5%, Scanlon *et al.* 2006 and references therein). For example, in Atacama Desert (Northern

Chile), Houston (2002) estimated that flood-related recharge in the apex area of alluvial fans can reach 34% of the precipitation event. Indeed, in arid mountain front zones, focused indirect recharge processes (underneath ephemeral streams) are greater than diffuse processes, which are more sensitive to subsurface evapotranspiration (Simmers, 1997; Hogan *et al.* 2004). Focused indirect recharge processes concentrate the runoff from a broad watershed toward an ephemeral stream (gully) where the high permeable deposits (or fractured rocks) promote the rapid and deep infiltration of the surface water. Considering the longer-term recharge rate estimating as well as the unconfined alluvial aquifer surface (285 000 m²), in the upstream part of the perched valley (Fig. 2-3a) above the impervious NS oriented fault (Fig. 2-8), we estimate that the recharged groundwater volume may range from 19 423 and 46 939 m^3. Those groundwater volumes are equivalent to 5.3 and 12.8 month of local pumping (5 m^3/h), respectively.

The analysis of the single well pumping test (Fig. 2-11c) allowed estimating the alluvial aquifer transmissivity (*i.e.* $1.37 \cdot 10^{-3}$ m²/s), with an accurate fitting of the Theis (1935) solution (blue color) on the drawdown data at intermediate and late times. Derivative data (red color) shows the influence of well-bore storage in early time, which agrees with the diameter of borehole (~ 1 m). At intermediate time due to the gravity delayed response caused by the unsaturated aquifer properties, the derivative decreases as the vertical groundwater flow component becomes important. Such behavior is also visible in the drawdown data that slightly deviates from the Theis (1935) solution. A derivative plateau is then reached indicating that the gravity drainage component is insignificant with respect to infinite-acting radial flows. At late time, derivative data seems revealing the influence

of a recharge boundary condition, while this latter it is not well defined. This results from the short duration of the pumping test (~ 7 hours).In order to better assess the aquifer properties and the influence of boundary conditions (faults, bedrock) on groundwater flows, a longer duration pumping test (several days) should be realized considering observation wells and an suitable pumping test solution.

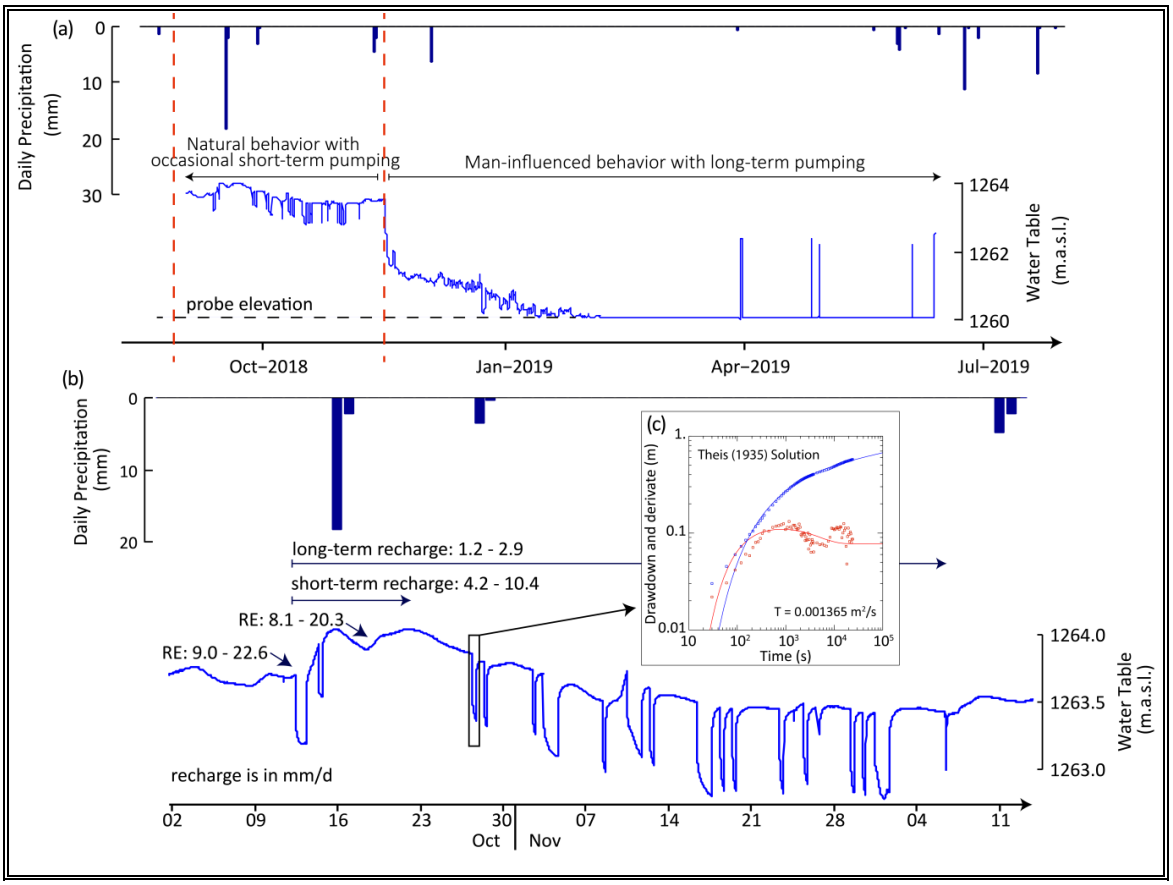

Figure 2-11. Comparison between daily precipitation (upper) and water table record (lower). a) Shows the complete period for 9 months. b) Specific sub-period of the total record (segment between red dotted lines in a). Two recharge events (RE) are identified, a short-term recharge and a long-term recharge. c) Corresponding a pumping test of sub-period b). Blue point is the drawdown and red point is the derivate, blue and red curves are the respectively modelling.

2.5 Conclusions and Perspectives: Conceptual models and future directions

The Western Andean Front is a morphotectonic transition zone between the Principal Cordillera and the Central Depression (Armijo *et al.* 2010; Farias *et al.* 2010) and it is shaped by NS oriented faults (Fig. 2-12a). We explored here the capacity of the Western Andean Front to be able to transfer groundwater up to Central Depression aquifers at the downstream. On one hand, our findings reveal that NS oriented faults are characterized by clay-rich fault core (gouges and hydrothermal clay-minerals) highlighted by the low resistivity (< 50 Ω-m) subvertical bands (LRSBs) on geoelectrical models. On the other hand, the presence of oblique basement faults and their intersections with the NS oriented faults are topologically related to springs, which reveals a contrast of permeability between both structures. In Central Chile, oblique basement faults were recently described as high-permeability axes conducting groundwater flows (Oyarzún *et al.* 2017; Piquer *et al.* 2019; Taucare *et al.* under revision-b). Similar observation was reported in different contexts, such as the Eastern Andean Front (Galetto *et al.* 2018) and the Pyrenees mountain range (Taillefer *et al.* 2018). In the Western Andean Front, oblique basement faults act as conduits, which drain groundwater from the fractured mountain block up to the adjacent alluvial aquifers. Such circulation permits a mountain block focused recharge of the Central depression aquifers (*e.g.* San Felipe Aquifer). The above-mentioned hydraulic properties of both type of faults (barriers and conduits) seem to be independent of the fault kinematic, suggesting that only the fault orientation governs the hydraulic properties. Further structural studies would be dedicated to describe the cross-cutting relationship between both faults in order to thoroughly characterize the fault-controlled

permeability at the intersection (mesoscale). The role of oblique basement faults in the focused recharge of adjacent alluvial aquifers has been also revealed in other mountain ranges (Wilson and Guan, 2004; Kebede et al. 2008; Walter *et al.* 2019). While mountain block diffuse recharge is proposed in typical conceptual models of mountain front zones (Wilson and Guan, 2004; Markovich *et al.* 2019), we reveals that NS oriented clay-rich faults are very low-permeability structures preventing that mountain block diffuse recharge process occurs along the Western Andean Front (Fig. 2-12c).

In this study, we explored also the capacity of perched valleys in the Western Andean Front to be able to transfer groundwater up to Central Depression aquifers at the downstream (Fig. 2-12b). In addition to the groundwater recharge coming from oblique basement faults, ephemeral streams (related to rainy events in the upstream part of the perched valley) mainly contribute to recharge the unconfined alluvial aquifers located in perched valleys (Fig. 2-12a). We estimated that the focused indirect recharge, derived from ephemeral stream infiltration (1.2 and 2.9 mm/d) represent between 5% and 12% of the total precipitation. In perched valley, ephemeral streams constitute high-permeability alluvial corridors ($1.4 \bullet 10^{-3}$ m^2/s) permitting a hydraulic continuity from the perched valley aquifers up to the Central Depression aquifers. The groundwater discharge from perched valley aquifers is an inter-basin groundwater flow that may support the renewal of the Central Depression aquifers during dry years. Considering the abrupt and ongoing decline of the precipitation in Central Chile (Garreaud *et al.* 2017, 2019), the current megadrought dramatically impacts the renewal of groundwater resources in perched valleys, but also the recharge of adjacent aquifers in the Central Depression. In addition, the perched

valleys are partially closed by low-permeability basement rocks and NS oriented faults (no-flow boundary conditions), which make groundwater resources vulnerable to excessive *in situ* withdrawals. By the identification of low resistivity plumes underneath irrigation canals, we highlighted the role of irrigation canal network in the artificial (but uncontrolled) focused indirect recharge of the Central Depression aquifers.

Consequently, given the advances in the characterization of aquifers recharge processes in the Western Andean Front (Central Chile), we state that regional conceptual models must be consider the role of oblique basement faults and perched valleys in the recharge of the adjacent Central Depression aquifers. Indeed, a pertinent mapping of NS oriented and oblique basement faults along the Western Andean Front will help for determining the suitable boundary condition to fix in further numerical modelling. Also, perched valleys could be stated as protected aquifer recharge areas where artificial recharge projects would be developed. In addition, while irrigation canal lining solutions can be presented as a suitable policy for reducing surface water losses and for efficiently managing the water resources, it will impact the recharge of Central Depression aquifers leading to an abrupt decline of the groundwater levels.

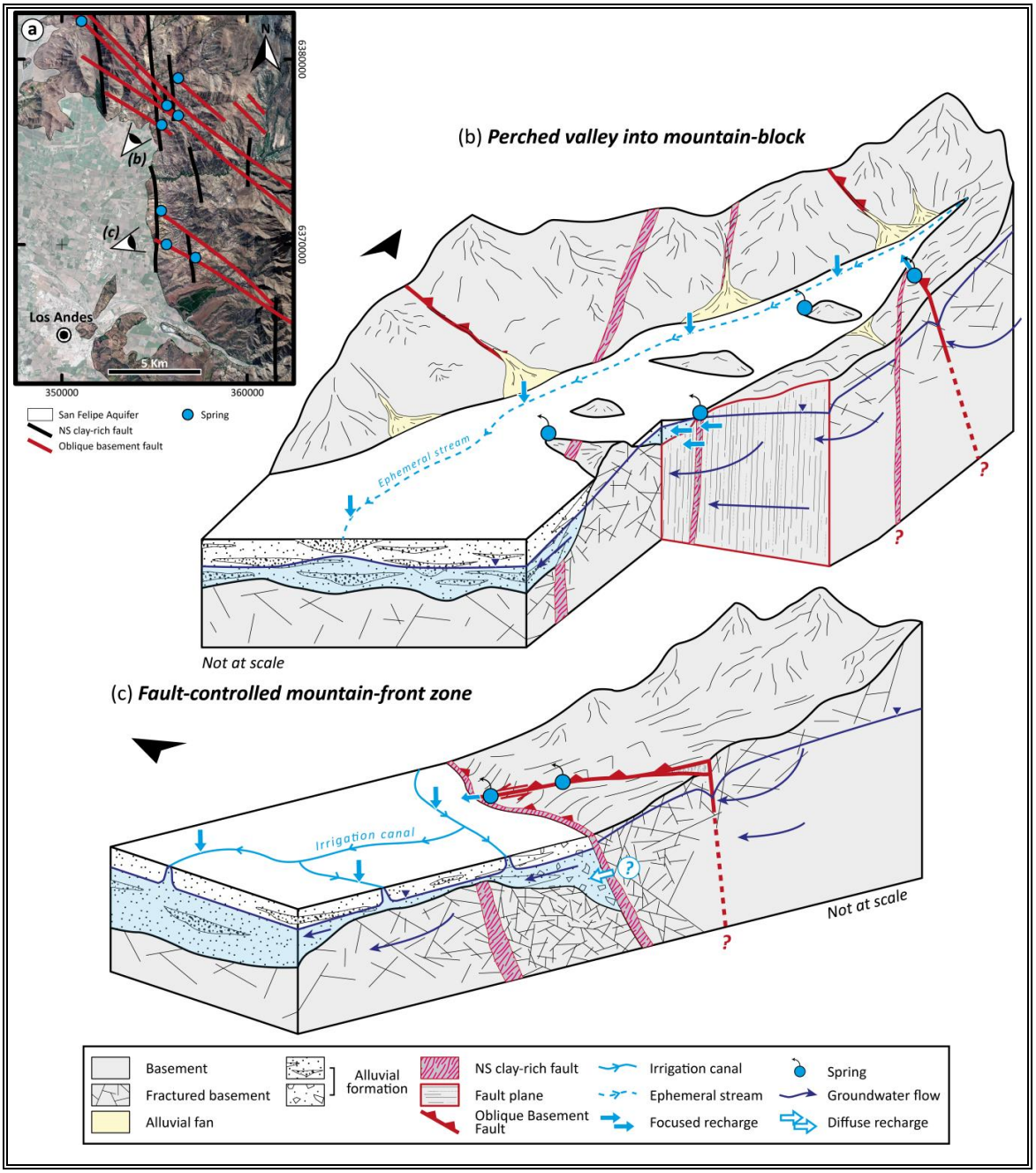

Figure 2-12. Groundwater circulation and recharge processes in the Western Andean Front. a) Map highlighting NS oriented faults and the oblique basement fault at Aconcagua Basin. b) Conceptual model of perched valley in the mountain-block. c) Conceptual model of fault-controlled mountain-front zone.

REFERENCES

Archie G.E. 1942. The Electrical Resistivity Log as an Aid in Determining Some Reservoir Characteristics. Society of Petroleum Engineers 146, 54-62. https://doi.org/10.2118/942054-G

Armijo R., Rauld R., Thiele R., Vargas G., Campos J., Lacassin R. & Kausel E. 2010. The West Andean Thrust, the San Ramón Fault, and the seismic hazard for Santiago, Chile. Tectonics 29 (2), TC2007. https://doi.org/10.1029/2008TC002427

Azócar G. F. & Brenning A. 2010. Hydrological and geomorphological significance of rock glaciers in the dry Andes, Chile (27°-33°s). Permafrost and Periglacial Processes, 21(1), 42–53. https://doi.org/10.1002/ppp.669

Ball L.B., Ge S., Caine J.S., Revil A. & Jardani A. 2010. Constraining fault-zone hydrogeology through integrated hydrological and geoelectrical analysis. Hydrogeology Journal 18 (5), 1057-1067. https://doi.org/10.1007/s10040-010-0587-z

Banton O. & Bangoy L.M. 1997. Hydrogéologie: multisciences environnementale des eaux souterraines, Presses de l'Université du Québec. 460 pp.

Barrett B.S., Garreaud R.D. & Falvey M. 2009. Effect of the Andes Cordillera on precipitation from a midlatitude cold front. Monthly Weather Review 137, 3092–3109. https://doi.org/10.1175/2009MWR2881.1

Benavente O., Tassi F., Reich M., Aguilera F., Capecchiacci F., Gutiérrez F., Vaselli O. & Rizzo A. 2016. Chemical and isotopic features of cold and thermal fluids discharged in the Southern Volcanic Zone between 32.5°S and 36°S: Insights into the physical and chemical processes controlling fluid geochemistry in geothermal systems of Central Chile. Chemical Geology 420, 97–113. https://doi.org/10.1016/J.CHEMGEO.2015.11.010

Bense V. F., Gleeson T., Loveless S. E., Bour O., & Scibek J. 2013. Fault zone hydrogeology. Earth-Science Reviews, 127, 171–192. https://doi.org/10.1016/j.earscirev.2013.09.008

Bense V. F., Shipton Z. K., Kremer Y., & Kampman, N. 2016. Fault zone hydrogeology: introduction to the special issue. Geofluids, 16(4), 655–657. https://doi.org/10.1111/gfl.12205

Boiero D., Godio A., Naldi M. & Yigit E. 2010. Geophysical investigation of a mineral groundwater resource in Turkey. Hydrogeology Journal 18 (5), 1219-1233. https://doi.org/10.1007/s10040-010-0604-2

Boisier J.P., Rondanelli R., Garreaud R.D. & Muñoz F. 2016. Anthropogenic and natural contributions to the Southeast Pacific precipitation decline and recent megadrought in

central Chile. Geophysical Research Letters 43 (1), 413–421. https://doi.org/10.1002/2015GL067265

Boughariou E., Allouche N., Jmal I., Mokadem N., Ayed B., Hajji S., Khanfir H. & Bouri S. 2018. Modeling aquifer behaviour under climate change and high consumption: Case study of the Sfax region, southeast Tunisia. Journal of African Earth Sciences 141, 118-129. https://doi.org/10.1016/j.jafrearsci.2018.02.006

Bown F., Rivera A. & Acuña C. 2008. Recent glacier variations at the Aconcagua basin, central Chilean Andes. Annals of Glaciology, 48 (2008), 43–48. https://doi.org/10.3189/172756408784700572

Boyce D. 2015. Modelo de evolución tectónica y paleogeográfica del margen andino en Chile Central durante el cretácico medio - tardío: El registro estructural y sedimentario en la formación Las Chilcas (MSc Thesis). Universidad de Chile, Santiago, Chile.

Bresciani E., Cranswick R.H., Banks E.W., Batlle-Aguilar J., Cook P.G. & Batelaan O. 2018. Using hydraulic head, chloride and electrical conductivity data to distinguish between mountain-front and mountain-block recharge to basin aquifers. Hydrology and Earth System Sciences 22, 1629-1648. https://doi.org/10.5194/hess-22-1629-2018

Bruhn R. L., Parry W. T., Yonkee W. A., & Thompson T. 1994. Fracturing and hydrothermal alteration in normal fault zones. Pure and Applied Geophysics, 142(3), 609–644. https://doi.org/10.1007/BF00876057

Bustamante M., Lemus M., Cortés R., Vivallos J., Cáceres D. & Wall R. 2012. Exploración geológica para el fomento de la energía geotérmica: Área de Jahuel, Región de Valparaiso. Servicio Nacional de Geología y Minería (SERNAGEOMIN), Santiago, Chile.

Caine J. S., Evans J. P., & Forster C. B. 1996. Fault zone architecture and permeability structure. Geology, 24(11), 1025–1028. http://dx.doi.org/10.1130/0091-7613(1996)024%3C1025:FZAAPS%3E2.3.CO

Carmichael R. S. 1989. Practical handbook of physical properties of rocks and minerals. Boca Raton, Fla: Boca Raton, Fla. CRC Press.

Carrière S.D., Ruffault J., Pimont F., Doussan C., Simioni G., Chalikakis K., Limousin J.-M., Scotti I., Courdier F., Cakpo C.-B., Davi H. & MartiNStPaul N.K. 2020. Impact of local soil and subsoil conditions on inter-individual variations in tree responses to drought: insights from Electrical Resistivity Tomography. Science of The Total Environment 698, 134247. https://doi.org/10.1016/j.scitotenv.2019.134247

Carter W.D. & Aguirre L. 1965. Structural Geology of Aconcagua Province and its Relationship to the Central Valley Graben, Chile. Geological Society of America Bulletin

76 (6), 651-664. https://doi.org/10.1130/0016-7606(1965)76[651:SGOAPA]2.0.CO;2

Casado I., Mahjoub H., Lovera R., Fernández J. & Casas A. 2015. Use of electrical tomography methods to determinate the extension and main migration routes of uncontrolled landfill leachates in fractured areas. Science of The Total Environment 506-507, 546-553. https://doi.org/10.1016/j.scitotenv.2014.11.068

Cembrano J., Lavenu A., Yáñez G., Riquelme R., Garcia M., González G. & Hérail G. 2007. Neotectonics. In: Moreno T. & Gibbons W. (Eds.), The Geology of Chile. Geological Society of London, 21-114. https://doi.org/10.1144/GOCH.9

Charrier R., Baeza O., Elgueta S., Flynn J.J., Gans P., Ka S.M., Muñoz N., Wyss A.R. & Zurita E. 2002. Evidence for Cenozoic extensional basin development and tectonic inversion south of the flat-slab segment, southern Central Andes, Chile (33°-36°S.L.). Journal of South American Earth Sciences 15 (1), 117-139. https://doi.org/10.1016/S0895-9811(02)00009-3

Charrier R., Pinto L. & Rodríguez M.P. 2007. Tectonostratigraphic evolution of the Andean Orogen in Chile. In: Moreno T. & Gibbons W. (Eds.), The Geology of Chile. Geological Society of London, 21-114. https://doi.org/10.1144/GOCH.3

Chester F. M., & Logan J. M. 1986. Implications for mechanical properties of brittle faults from observations of the Punchbowl fault zone, California. Pure and Applied Geophysics, 124(1), 79–106. https://doi.org/10.1007/BF00875720

Coira B., Davidson J., Mpodozis C. & Ramos V. 1982. Tectonic and magmatic evolution of the Andes of northern Argentina and Chile. Earth-Science Reviews 18 (3-4), 303-332. https://doi.org/10.1016/0012-8252(82)90042-3

Cortés G., Vargas X. & McPhee J. 2011. Climatic sensitivity of streamflow timing in the extratropical western Andes Cordillera. Journal of Hydrology 405 (1-2), 93-109. https://doi.org/10.1016/j.jhydrol.2011.05.013

Darcy H. 1856. Les fontaines publiques de la ville de Dijon. Paris: Victor Dalmont, 659 p.

Darwin C. 1839. The voyage of the Beagle. Wordsworth, 733 p.

DeCelles P.G., Ducea M.N., Kapp P. & Zandt G. 2009. Cyclicity in Cordilleran orogenic systems. Nature Geoscience 2, 251-257. https://doi.org/10.1038/ngeo469

Descloitres M., Chalikakis K., Legchenko A., Moussa A.M., Genthon P., Favreau G., Le Coz M., Boucher M. & Oï M. 2013. Investigation of groundwater resources in the Komadugu Yobe Valley (Lake Chad Basin, Niger) using MRS and TDEM methods. Journal of African Earth Sciences 87, 71-85. https://doi.org/10.1016/j.jafrearsci.2013.07.006

DGA. 2015. Determinación de la Disponibilidad de Aguas Subterráneas en el Valle del Río Aconcagua. Dirección General de Aguas (DGA), Santiago, Chile.

DGA. 2016. Disponibilidad de Recursos Hídricos ára el Otorgamiento de Derechos de Aprovechamiento de Aguas Subterráneas en el Valle del Aconcagua: Sectores hidrogeológicos de San Felipe, Putaendo, Panquehue, Catemu y Llay Llay. Dirección General de Aguas (DGA), Santiago, Chile.

DGA. 2019. Inventario Público de Información Hidrológica y Meteorológica. Dirección General de Aguas (DGA), Santiago, Chile. http://snia.dga.cl/BNAConsultas/reportes

Estay N.P., Yáñez G., Carretier S., Lira E., & Maringue J. 2016. Seismic hazard in low slip rate crustal faults, estimating the characteristic event and the most hazardous zone: Study case San Ramón Fault, in southern Andes. Natural Hazards and Earth System Sciences 16 (2), 2511-2528. https://doi.org/10.5194/nhess-16-2511-2016

Farías M., Comte D., Charrier R., Martinod J., David C., Tassara A., Tapia F. & Fock A. 2010. Crustal-scale structural architecture in central Chile based on seismicity and surface geology: Implications for Andean mountain building. Tectonics 29 (3), TC3006. https://doi.org/10.1029/2009TC002480

Faulkner D. R., Jackson C. A. L., Lunn R. J., Schlische R. W., Shipton Z. K., Wibberley C. A. J., & Withjack M. O. 2010. A review of recent developments concerning the structure, mechanics abrund fluid flow properties of fault zones. Journal of Structural Geology, 32(11), 1557–1575. https://doi.org/10.1016/j.jsg.2010.06.009

Fetter, C. W. 2001. Applied Hydrogeology (4th edition). Upper Saddle River, N.J: Prentice Hall, 598 pp.

Flores-Avilés G.P., Descloitres M., Duwig C., Rossier Y., Spadini L., Legchenko A., Soruco Á., Argollo J., Pérez M. & Medinaceli W. 2020. Insight into the Katari-Lago Menor Basin aquifer, Lake Titicaca-Bolivia, inferred from geophysical (TDEM), hydrogeological and geochemical data. Journal of South American Earth Sciences 99, 102479. https://doi.org/10.1016/j.jsames.2019.10247

Francese R., Mazzarini F., Bistacchi A., Morelli G., Pasquarè G., Praticelli N., Robain H., Wardell N. & Zaja A. 2009. A structural and geophysical approach to the study of fractured aquifers in the Scansano-Magliano in Toscana Ridge, southern Tuscany, Italy. Hydrogeology Journal 17 (5), 1233-1246. https://doi.org/10.1007/s10040-009-0435-1

Freeze R. A., & Cherry J. A. 1979. Groundwater. Englewood Cliffs, N.J: Prentice-Hall, 604 pp.

Fuentes F., Vergara M., Aguirre L. & Féraud G. 2002. Contact relationships of Tertiary volcanic units from the Andes of Central Chile (33°S): a reinterpretation based on

$^{40}Ar/^{39}Ar$ dating. Revista Geológica de Chile 29 (2), 151-165.

Fuentes F., Aguirre L., Vergara M., Valdebenito L. & Fonseca E. 2004. Miocene fossil hydrothermal system associated with a volcanic complex in the Andes of central Chile. Journal of Volcanology and Geothermal Research 138 (1–2), 139-161. https://doi.org/10.1016/j.jvolgeores.2004.07.001

Galetto A., García V. & Caselli A. 2018. Structural controls of the Domuyo geothermal field, Southern Andes (36°38′S), Argentina. Journal of Structural Geology 114, 76-94. https://doi.org/10.1016/j.jsg.2018.06.002

Garreaud R.D., Alvarez-Garreton C., Barichivich J., Boisier J.P., Christie D., Galleguillos M., LeQuesne C., McPhee J. & Zambrano-Bigiarini M. 2017. The 2010–2015 megadrought in central Chile: impacts on regional hydroclimate and vegetation. Hydrology and Earth System Sciences 21 (12), 6307–6327. https://doi.org/10.5194/hess-21-6307-2017

Garreaud R.D., Boisier J.P., Rondanelli R., Montecinos A., Sepúlveda H.H. & Veloso-Aguila D. 2019. The Central Chile Mega Drought (2010–2018): A climate dynamics perspective. International Journal of Climatology, 1-19. https://doi.org/10.1002/joc.6219

Garven G. 1995. Continental-Scale Groundwater Flow and Geologic Processes. Annual Review of Earth and Planetary Sciences, 23(1), 89–117. https://doi.org/10.1146/annurev.ea.23.050195.000513

Gehrels H. & Gieske A.S.M. 2003. Aquifer dynamics. In: Simmers I. (Ed.), Understanding water in a dry environment. CRC Press, 211-247.

Giambiagi L.B., Ramos V.A., Godoy E., Alvarez P.P. & Orts S. 2003. Cenozoic deformation and tectonic style of the Andes, between 33° and 34° south latitude. Tectonics 22 (4), 1041. https://doi.org/10.1029/2001TC001354

Gleeson T., Wada Y., Bierkens M.F.P. & Van Beek L.P.H. 2012. Water balance of global aquifers revealed by groundwater footprint. Nature, 488, 197-200. https://doi.org/10.1038/nature11295

Godoy E., Yañez G. & Vera E. 1999. Inversion of an Oligocene volcano-tectonic basin and uplifting of its superimposed Miocene magmatic arc in the Chilean Central Andes: first seismic and gravity evidences. Tectonophysics 306 (2), 217–236. https://doi.org/10.1016/S0040-1951(99)00046-3

Grant F. S., & West G. F. 1965. Interpretation theory in applied geophysics. New York: McGraw-Hill.

Guérin R., Descloitres M., Coudrain A., Talbi A. & Gallaire R. 2001. Geophysical surveys for identifying saline groundwater in the semi-arid region of the central Altiplano, Bolivia.

Hydrological Processes 15 (17), 3287-3301. https://doi.org/10.1002/hyp.284

Hauser A. 1997. Catastro y caracterización de las fuentes de aguas minerales y termales de Chile. Servicio Nacional de Geología y Minería (SERNAGEOMIN), Santiago, Chile.

Healy R.W. & Scanlon B.R. 2010. Estimating Groundwater Recharge. Cambridge University Press, 245 pp. https://doi.org/10.1017/CBO9780511780745

Hogan J.F., Phillips F.M., Scanlon B.R. 2004. Groundwater Recharge in a Desert Environment: the Southwestern United States, Volume 9. American Geophysical Union, 172 pp.

Hoke G.D., Aranibar J.N., Viale M., Araneo D.C. & Llano C. 2013. Seasonal moisture sources and the isotopic composition of precipitation, rivers, and carbonates across the Andes at 32.5-35.5°S. Geochemistry, Geophysics, Geosystems 14 (4), 962–978. https://doi.org/10.1002/ggge.20045

Houston J. 2002. Groundwater recharge through an alluvial fan in the Atacama Desert, northern Chile: mechanisms, magnitudes and causes. Hydrological Processes 16, 3016-3035. https://doi.org/10.1002/hyp.1086

Jara P. & Charrier R. 2014. New stratigraphical and geochronological constraints for the Mezo-Cenozoic deposits in the High Andes of central Chile between 32° and 32°30'S: Structural and palaeogeographic implications. Andean Geology 41 (1), 174–209. https://doi.org/10.5027/andgeoV41n1-a07

Johnson A. I. 1967. Specific yield - Compilation of specific yields for various materials. USGS Water-Supply Paper 1662-D. https://doi.org/10.3133/wsp1662D

Jordan T.E., Burns W.M., Veiga R., Pángaro F., Copeland P., Kelley S. & Mpodozis C. 2001. Extension and basin formation in the southern Andes caused by increased convergence rate: A mid-Cenozoic trigger for the Andes. Tectonics 20 (3), 308–324. https://doi.org/10.1029/1999TC001181

Kaminsky A.E. 2010. ZondRes2D. Software for two-dimensional interpretation of DC resistivity and IP data. Zond Geophysical Software, Saint-Petersburg (Russia).

Kazakis N., Vargemezis G. & Voudouris K.S. 2016. Estimation of hydraulic parameters in a complex porous aquifer system using geoelectrical methods. Science of The Total Environment 550, 742-750. https://doi.org/10.1016/j.scitotenv.2016.01.133

Kebede S., Travi Y., Asrat A., Alemayehu T., Ayenew T. & Tessema Z. 2008. Groundwater water origin and flow along selected transects in Ethiopian rift volcanic aquifers. Hydrogeology Journal 16 (1), 55-73. https://doi.org/10.1007/s10040-007-0210-0

Keller G.V. 1988. Rock and mineral properties. In: Nabighian M.N. (Ed), Electromagnetic methods in applied geophysics. SEG Publ., 13-51.

Kresic N. & Mikszewski A. 2012. Hydrogeological conceptual site models: Data analysis and visualization (1st ed.). CRC Press, 600 pp. https://doi.org/10.1201/b12151

Manning A. H., & Solomon D. K. 2005. An integrated environmental tracer approach to characterizing groundwater circulation in a mountain block. Water Resources Research, 41(12), 1–18. https://doi.org/10.1029/2005WR004178

Marchant M., Cecioni A., Figueroa S., González H., Giglio S., Hebbeln D., Kaiser J., Lamy F., Mohtadi M., Pineda V. & Romero, O. 2007. Marine geology, oceanography and climate. In: Moreno T. & Gibbons W. (Eds.), The Geology of Chile. Geological Society of London. https://doi.org/10.1144/GOCH.11

Markovich K.H., Manning A.H., Condon L.E. & McIntosh J.C. 2019. Mountain-block Recharge: A review of Current Understanding. Water Resources Research, 55. https://doi.org/10.1029/2019WR025676

McCarter W. J. 1984. The electrical resistivity characteristics of compacted clays. Geotechnique, 34, 263–267. https://doi.org/10.1680/geot.1984.34.2.263

Mitchell J. K. 2005. Fundamentals of soil behavior. (K. Soga, Ed.) (3 ed.). Hoboken: Hoboken : John Wiley & Sons.

Montecinos A. & Aceituno P. 2003. Seasonality of the ENSO-related rainfall variability in central Chile and associated circulation anomalies. Journal of Climate 16, 281–296. https://doi.org/10.1175/1520-0442(2003)016<0281:SOTERR>2.0.CO;2

Mpodozis C. & Ramos V. 1989. The Andes of Chile and Argentina. In: Ericksen G.E., Cañas-Pinochet M.T. & Reinemund J. (Eds.), Geology of the Andes and its relation to hydrocarbon and mineral resources. Circum-Pacific Counsil for Energy and Mineral Resources, 59–90.

Muñoz J.F., Fernández B., Varas E., Pastén P., Gómez D., Rengifo P., Muñoz J., Atenas M. & Jofré J.C. 2007. Chilean water resources. In: Moreno T. & Gibbons W. (Eds.), The Geology of Chile. Geological Society of London, 21-114. https://doi.org/10.1144/GOCH.8

Murty B.V.S. & Raghavan V.K. 2002. The gravity method in groundwater exploration in crystalline rocks: A study in the peninsular granitic region of Hyderabad, India. Hydrogeology Journal 10 (2), 307-321. https://doi.org/10.1007/s10040-001-0184-2

NOAA/National Weather Service. 2019. El Niño Southern Oscilation (ENSO): Historical El Niño/La Niña episodes (1950-present). https://origin.cpc.ncep.noaa.gov/products/analysis_monitoring/ensostuff/ONI_v5.php

Ohlanders N., Rodriguez M. & McPhee J. 2013. Stable water isotope variation in a Central Andean watershed dominated by glacier and snowmelt. Hydrology and Earth System Sciences 17, 1035–1050. https://doi.org/10.5194/hess-17-1035-2013

Oyarzún R., Oyarzún J., Fairley J.P., Núñez J., Gómez N., Arumí J.L. & Maturana H. 2017. A simple approach for the analysis of the structural-geologic control of groundwater in an arid rural, mid-mountain, granitic and volcanic-sedimentary terrain: The case of the Coquimbo Region, North-Central Chile. Journal of Arid Environments 142, 31–35. https://doi.org/10.1016/J.JARIDENV.2017.03.003

Pellicciotti F., Burlando P., & Van Vliet K. 2007. Recent trends in precipitation and streamflow in the Aconcagua River basin, Central Chile. International Association of Hydrological Sciences, (318), 1–22. https://doi.org/10.3189/172756408784700572

Peng T.R., Zhan W.J., Tong L.T., Chen C.T., Liu T.S. & Lu W.C. 2018. Assessing the recharge process and importance of montane water to adjacent tectonic valley-plain groundwater using a ternary end-member mixing analysis based on isotopic and chemical tracers. Hydrogeology Journal 26 (6), 2041-2055. https://doi.org/10.1007/s10040-018-1741-2

Peña H., & Nazarala B. 1987. Snowmelt-runoff simulation model of a central Chile Andean basin with relevant orographic effects. International Association of Hydrological Sciences, 166(166), 161–172.

Piquer J., Hollings P., Rivera O., Cooke D.R., Baker M. & Testa F. 2017. Along-strike segmentation of the Abanico Basin, central Chile: New chronological, geochemical and structural constraints. Lithos 268–271, 174–197. https://doi.org/10.1016/j.lithos.2016.10.025

Piquer J., Yañez G., Rivera O. & Cooke D.R. 2019. Long-lived crustal damage zones associated with fault intersections in the high Andes of Central Chile. Andean Geology 46, 223-239. https://doi.org/10.5027/andgeoV46n2-3106

Ragettli S., & Pellicciotti F. 2012. Calibration of a physically based, spatially distributed hydrological model in a glacierized basin: On the use of knowledge from glaciometeorological processes to constrain model parameters. Water Resources Research, 48(3), 1–20. https://doi.org/10.1029/2011WR010559

Rivano S., Sepúlveda P., Boric R. & Espiñeira D. 1993. Hojas Quillota y Portillo, Escala 1:250.000. Servicio Nacional de Geología y Minería (SERNAGEOMIN), Santiago, Chile.

Rivera D., Godoy-Faúndez A., Lillo M., Alvez A., Delgado V., Gonzalo-Martín C., Menasalvas E., Costumero R. & García-Pedrero A. 2016. Legal disputes as a proxy for regional conflicts over water rights in Chile. Journal of Hydrology 535, 36-45. https://doi.org/10.1016/j.jhydrol.2016.01.057

Robson S. G., & Banta E. R. 1995. Ground Water Atlas of the United States: Segment 2, Arizona, Colorado, New Mexico, Utah. Hydrologic Atlas. https://doi.org /10.3133/ha730C

Roques C., Bour O., Aquilina L., Dewandel B., Leray S., Schroetter J. M. & Mougin, B. 2014. Hydrological behaviour of a deep sub-vertical fault in crystalline basement and relationships with surrounding reservoirs. Journal of Hydrology, 509, 42–54. https://doi.org/10.1016/j.jhydrol.2013.11.023

Roques C., Bour O., Aquilina L., & Dewandel B. 2016. High-yielding aquifers in crystalline basement: insights about the role of fault zones, exemplified by Armorican Massif, France. Hydrogeology Journal, 24(8), 2157–2170. https://doi.org/10.1007/s10040-016-1451-6

Samouëlian A., Cousin I., Tabbagh A., Bruand A., & Richard G. 2005. Electrical resistivity survey in soil science: a review. Soil and Tillage Research, 83(2), 173–193. https://doi.org/https://doi.org/10.1016/j.still.2004.10.004

Sanford W. 2002. Recharge and groundwater models: An overview. Hydrogeology Journal, 10(1), 110–120. https://doi.org/10.1007/s10040-001-0173-5

Scanlon B.R., Healy R.W. & Cook P.G. 2002. Choosing appropriate techniques for quantifying groundwater recharge. Hydrogeology Journal 10 (1), 18-39. https://doi.org/10.1007/s10040-001-0176-2

Scanlon B.R., Keese K.E., Flint A.L., Flint L.E., Gaye C.B., Edmunds W.M. & Simmers I. 2006. Global synthesis of groundwater recharge in semiarid and arid regions. Hydrological Processes 20 (15), 3335–3370. https://doi.org/10.1002/hyp.6335

Schwartz, F. W., & Zhang, H. 2003. Fundamentals of ground water. New York: Wiley, 592 pp. https://doi.org/10.2113/11.3.285

Siebert S., Burke J., Faures J.M., Frenken K., Hoogeveen J., Döll P. & Portmann F.T. 2010. Groundwater use for irrigation – a global inventory. Hydrology and Earth System Sciences 14 (10), 1863-1880. https://doi.org/10.5194/hess-14-1863-2010

Simmers, I. 1997. Groundwater recharge principles, problems and developments. In: Simmers I. (Ed.), Recharge of phreatic aquifers in (semi-)arid areas. CRC Press, 1-18.

Stěpančíkova P., Dohnal J., Pánek T., Łój M., Smolková V. & Šilhán K. 2011. The application of electrical resistivity tomography and gravimetric survey as useful tools in an active tectonics study of the Sudetic Marginal Fault (Bohemian Massif, central Europe). Journal of Applied Geophysics 74 (1), 69-80. https://doi.org/10.1016/j.jappgeo.2011.03.007

Taillefer A., Guillou-Frottier L., Soliva R., Magri F., Lopez S., Courrioux G., Millot R.,

Ladouche B. & Le Goff E. 2018. Topographic and Faults Control of Hydrothermal Circulation Along Dormant Faults in an Orogen. Geochemistry, Geophysics, Geosystems 19 (12), 4972-4995. https://doi.org/10.1029/2018GC007965

Tassara A., Götze H.J., Schmidt S. & Hackney R. 2006. Three-dimensional density model of the Nazca plate and the Andean continental margin. Journal of Geophysical Research 111 (B9), B09404. https://doi.org/10.1029/2005JB003976

Taucare M., Daniele L., Viguier B. & Vallejos A. *Under revision-a*. Groundwater resources and recharge processes in the Western Andean Front of Central Chile. Science of the Total Environment.

Taucare M., Viguier B., Daniele L., Heuser G. & Arancibia G. *Under revision-b*. Assessing the Western Andean Front boundary condition by a topological approach (Aconcagua Basin, Central Chile). Hydrogeology Journal.

Telford W.M., Geldart L.P. & Sheriff R.E. 1990. Applied Geophysics (2nd edition). Cambridge University Press, 770 pp. https://doi.org/10.1017/CBO9781139167932

Theis C.V. 1935. The relation between the lowering of the piezometric surface and the rate and duration of discharge of a well using groundwater storage. Transactions America Geophysical Union 16, 519-524.

Valdés-Pineda R., Pizarro R., García-Chevesich P., Valdés J.B., Olivares C., Vera M., Balocchi F., Pérez F., Vallejos C., Fuentes R., Abarza A. & Helwig B. 2014. Water governance in Chile: Availability, management and climate change. Journal of Hydrology 519 (C), 2538-2567. https://doi.org/10.1016/j.jhydrol.2014.04.016

Vargas G., Klinger Y., Rockwell T.K., Forman S.L., Rebolledo S., Baize S., Lacassin R. & Armijo R. 2014. Probing large intraplate earthquakes at the west flank of the Andes. Geology 42 (12), 1083–1086. https://doi.org/10.1130/G35741.1

Viguier B., Jourde H., Yáñez G., Lira E.S., Leonardi V., Moya C.E., García-Pérez T., Maringue J. & Lictevout E. 2018. Multidisciplinary study for the assessment of the geometry, boundaries and preferential recharge zones of an overexploited aquifer in the Atacama Desert (Pampa del Tamarugal, Northern Chile). Journal of South American Earth Sciences 86, 366-383. https://doi.org/10.1016/j.jsames.2018.05.018

Viguier B., Daniele L., Jourde H., Leonardi V. & Yañez G. 2019. Changes in the conceptual model of the Pampa del Tamarugal Aquifer: Implications for Central Depression water resources. Journal of South American Earth Sciences 94, 102217. https://doi.org/10.1016/j.jsames.2019.102217

Viviroli D., Weingartner R., & Messerli B. 2006. Assessing the Hydrological Significance of the World's Mountains. Mountain Research and Development, 23(1), 32–40.

https://doi.org/10.1659/0276-4741(2003)023[0032:athsot]2.0.co;2

Wahi A. K., Hogan J. F., Ekwurzel B., Baillie M. N., & Eastoe C. J. 2008. Geochemical quantification of semiarid mountain recharge. Ground Water, 46(3), 414–425. https://doi.org/10.1111/j.1745-6584.2007.00413.x

Wall R., Sellés D. & Gana P. 1999. Área Tiltil-Santiago, región Metropolitana, Escala 1:100.000. Servicio Nacional de Geología y Minería (SERNAGEOMIN), Santiago, Chile.

Walter B., Géraud Y., Hautevelle Y., Diraison M. & Raisson F. 2019. Fluid Circulations at Structural Intersections through the Toro-Bunyoro Fault System (Albertine Rift, Uganda): A Multidisciplinary Study of a Composite Hydrogeological System. Geofluids, 20 pp. https://doi.org/10.1155/2019/8161469

Waylen P.R. & Caviedes C.N. 1990. Annual and seasonal fluctuations of precipitation and streamflow in the Aconcagua River basin, Chile. Journal of Hydrology 120 (1-4), 79-102. https://doi.org/10.1016/0022-1694(90)90143-L

Wilson J.L. & Guan H. 2004. Mountain-block hydrology and mountain-front recharge. In: Hogan J.F., Phillips F.M. & Scanlon B.R. (Eds.), Groundwater Recharge in a Desert Environment: The Southwestern United States. American Geophysical Union 9, 113–137.

World Bank. 2011. Chile. Diagnóstico de la gestión de los recursos hídricos. Departamento del Medio Ambiente y Desarrollo Sostenible, Region para América Latina y el Caribe. http://water.worldbank.org/node/83999

Yáñez G., Ranero C., von Huene R. & Díaz J. 2001. Magnetic anomaly interpretation across the southern central Andes (32°-34°S): The role of the Juan Fernandez Ridge in the late Tertiary evolution of the margin. Journal of Geophysical Research 106 (B4), 6325-6345. https://doi.org/10.1029/2000JB900337

Yañez G., Cembrano J., Pardo M., Ranero C. & Selles D. 2002. The Challenger–Juan Fernández–Maipo major tectonic transition of the Nazca–Andean subduction system at 33–34°S: geodynamic evidence and implications. Journal of South American Earth Sciences 15 (1), 23-38. https://doi.org/10.1016/S0895-9811(02)00004-4

Yáñez G. & Cembrano J. 2004. Role of viscous plate coupling in the late Tertiary Andean tectonics. Journal of Geophysical Research: Solid Earth 109 (B2), B02407. https://doi.org/10.1029/2003jb002494

Yáñez G., Muñoz M., Flores-Aqueveque V. & Bosch A. 2015. Gravity depth to basement in Santiago Basin, Chile: implications for its geological evolution, hydrogeology, low enthalpy geothermal, soil characterization and geo-hazards. Andean Geology 42 (2), 147-172. https://doi.org/10.5027/andgeoV42n2-a01

APPENDIX

APPENDIX A: "FUNDAMENTALS OF GRAVIMETRIC METHOD"

The gravimetric method involves measurements of variations in the earth gravitational field. These gravitational variations are due to excess of defects of mass that are produced by the contrast density of the different units of the earth. Gravity is a passive geophysical method, because it does not require an artificial source to observed it. Gravity is a potential method in which all the factors disturbing the acceleration of gravity are added together. The process of gravity data has the consequence of discounting all the effects that have nothing to do with the research objective, which in this particular case is the mass defect associated with the sedimentary basin.

A.1 Gravity and gravimetric method

The gravity force defined by the second Newton's Law correspond to the force F between two masses m_1 and m_2 which is inversely proportional to the square of the distance between both masses, and directly proportional to the product of the masses. Mathematically it is expressed as

$$F = - G \frac{m_1 m_2}{r^2} \hat{r} \qquad (A.1)$$

Where G is the universal gravitational constant (6.67259×10^{-11} [$m^3 kg^{-1} s^{-2}$]), r is the distance between both masses, and $\hat{r}$ is a unit vector directed from m_1 to m_2. When m_2 is the mass of the Earth M_e, and $r = R_e$ the Earth radius, $\hat{r}$ is directed toward the center of the Earth. In this case the acceleration of gravity g is given by

$$g = G \frac{M_e}{R_e^2} \hat{r} \qquad (A.2)$$

Gravitational fields are conservative, so it is possible to express it as the gradient of a scalar potential. Being a conservative field, it complies with the principle of superposition, so the gravity potential of a set of masses would be the sum of the gravitational forces of each mass individually. This can be written as

$$g(P) = -\nabla U(P) = G\int \frac{dm}{r^2} = G\int \frac{\rho(V)}{r^2}\, dV \qquad (A.3)$$

Where the integration is on the volume V, and $\rho(V)$ is the density distribution of the that volume. Then, the Eq. A.3 shows that the gravity generated by any mass distribution can be expressed in density terms.

The gravimetric method uses the principle of gravitational field of the Earth to study different geological problems measuring on surface the vertical component of the gravity acceleration. The measuring is through a gravimeter which used the miliGal [mGal] as the unit of measurement (1 mGal = 10^{-3} Gal = 10^{-5} m s^{-2}). To study the effect of the gravity signal of interest it is necessary to isolate it from signals that also have an effect on gravity, such as internal variations on the gravimeter, gravitational variations by the Moon and the Sun, positional influences by the latitude and altitude, and regional effects.

A.2 Data processing

As it was mentioned previously, in order to analyze the effect of the density contrast between the rock and the sediments, it is necessary to perform previously the following processing and corrections:

1) Instrumental drift C_{id}, this correction assumes that the equipment used has a variation in measurements due to the fatigue of the internal spring that measures the gravity value.

To correct this effect, gravity is measured twice in the same place at beginning (g_base_0) and the ending (g_base_f) of the day. The trend generated by these gravimetric readings represents the instrumental drift during the measurements time window, and it must be subtracted proportional to the time of the given measurement. Eq. A.4 calculates the instrumental drift, which used the initial and final time of the base, and the time of each measurement.

$$C_{id} = \left(\frac{g\_base_f - g\_base_0}{t\_base_f - t\_base_0}\right)(t_i - t\_base_0) \quad (A.4)$$

In addition, because the data were measured on different days, the drift between days was referenced to a single day.

2) Earth tide correction C_{et}, their corrects changes caused by gravitational attraction of the Moon and the Sun. This effect depends the on latitude and time of the measurement. The gravimeter used in this study record these changes automatically (in a variable called ETC), if location and time are properly set. To correct this effect, from gravity observations, this value should be subtracted.

3) Conversion to absolute value g_{abs}, as it was mentioned above, the gravity measured is a relative value and must be converted to an absolute value. For this, it is assumed that the gravity differences between two points are the same, if relative or absolute gravity is compared. So, knowing the absolute gravity value from a given point, it is possible to determine the absolute gravity value of a series on field observations. Eq. 5 allows to convert relative gravity g_{rel_i} to absolute values g_{abs}, using the relative and absolute value of the base station.

$$g_{abs} = \left(g_{rel_i} - g_{rel_{base}}\right) - g_{abs_{base}} \quad \text{(A.5)}$$

4) Latitude correction C_ϕ, compensates the effect generated by the irregular shape and rotation of the Earth. For this, the earth shape is approximated by a reference spheroid which is an oblate ellipsoid. There are many Geoid models that estimate the theorical value of gravity, for this case it was used the World Geodetic System 1984 (WGS84) model that uses the latitude ϕ (in radians). This value must be subtracted, and it is calculated as

$$C_\phi = 978032.67714 \frac{1+0.00193185138639 \sin\phi^2}{\sqrt{1-0.00669437999013 \sin\phi^2}} \text{ [mGal]} \quad \text{(A.6)}$$

5) Free-air correction C_{FA}, as it is shown in Eq. A.3 the gravity varies inversely with the square of distance, so it is necessary to compensate the elevation effects between the gravity measurement location and the center of the earth. However, the free-air correction does not consider the masses between the gravity station and the reference spheroid. The free-air correction is added to the observed gravity and it is obtained by the approximation of the Earth shape as a sphere. To apply this correction is necessary to know the station position precisely, specially the vertical component z, which is used in Eq. A.7

$$C_{FA} = 0.3086\ z \text{ [mGal] (with z in meters)} \quad \text{(A.7)}$$

6) Bouguer correction C_{bou}, considers the masses between the gravity station and the reference spheroid. For this, infinite plate model is used (Telford et al., 1990). The bouguer correction is applied in the opposite sense to free-air so it is subtracted to the observed gravity, and it is given by

$$C_{bou} = 2\,\pi\,G\,\rho\,z = 0.04192\,\rho\,z\ [\text{mGal}] \quad (A.8)$$

Where z is the altitude in [m] and ρ is the mean density of the crustal in [g/cm^3]. For this case it was used a mean density of crustal 2.65 [g/cm^3].

7) Terrain correction g_{ter}, a very significative correction in places where the topographic is very irregular, for example in valleys or mountains zone. As it was mentioned the bouguer correction considers a homogeneous block of infinite lateral extension, so the terrain correction compensates the irregularities that was not considered in the Bouguer correction. This correction is added to the observed gravity and it was calculated through of Oasis-Montaj software that uses a digital elevation model (DEM) to obtain it.

8) Regional effect g_{reg}, involves the gravity variations produced by the compensation of mountain ranges and lithological heterogeneities. In this study, the main Regional effect is caused by the compensation of the Andes mountain range that generates thicker crustal thickness underneath. In the case of Chile, the decrease in the gravity signal due to this effect tends towards the east (i.e.Tassara and Yáñez, 2003). The Regional effect was calculated manually in the ModelVision software and represented in MATLAB in Figure A-1.

In summary, the observed gravity in field must be corrected by temporal effects g_{NT} (C_{ET}, C_{id} and C_{dd}), producing an absolute value of gravity. The absolute gravity is in turn corrected by spatial effects ($C_{\phi}, C_{FA}, C_{bou}$and C_{ter}). Once obtained the bouguer gravity (g_{bou}) (without spatial effects), regional effects should be subtracted to obtain the residual gravity anomaly g_{res}. Mathematically, the following procedure must be followed

$$g_{NT} = g_{obs} - C_{ET} - C_{id} \rightarrow g_{abs} \quad \text{(A.9)}$$

$$g_{bou} = g_{abs} - C_{\phi} + C_{FA} - C_{bou} + C_{ter} \quad \text{(A.10)}$$

$$g_{res} = g_{bou} - g_{reg} \quad \text{(A.11)}$$

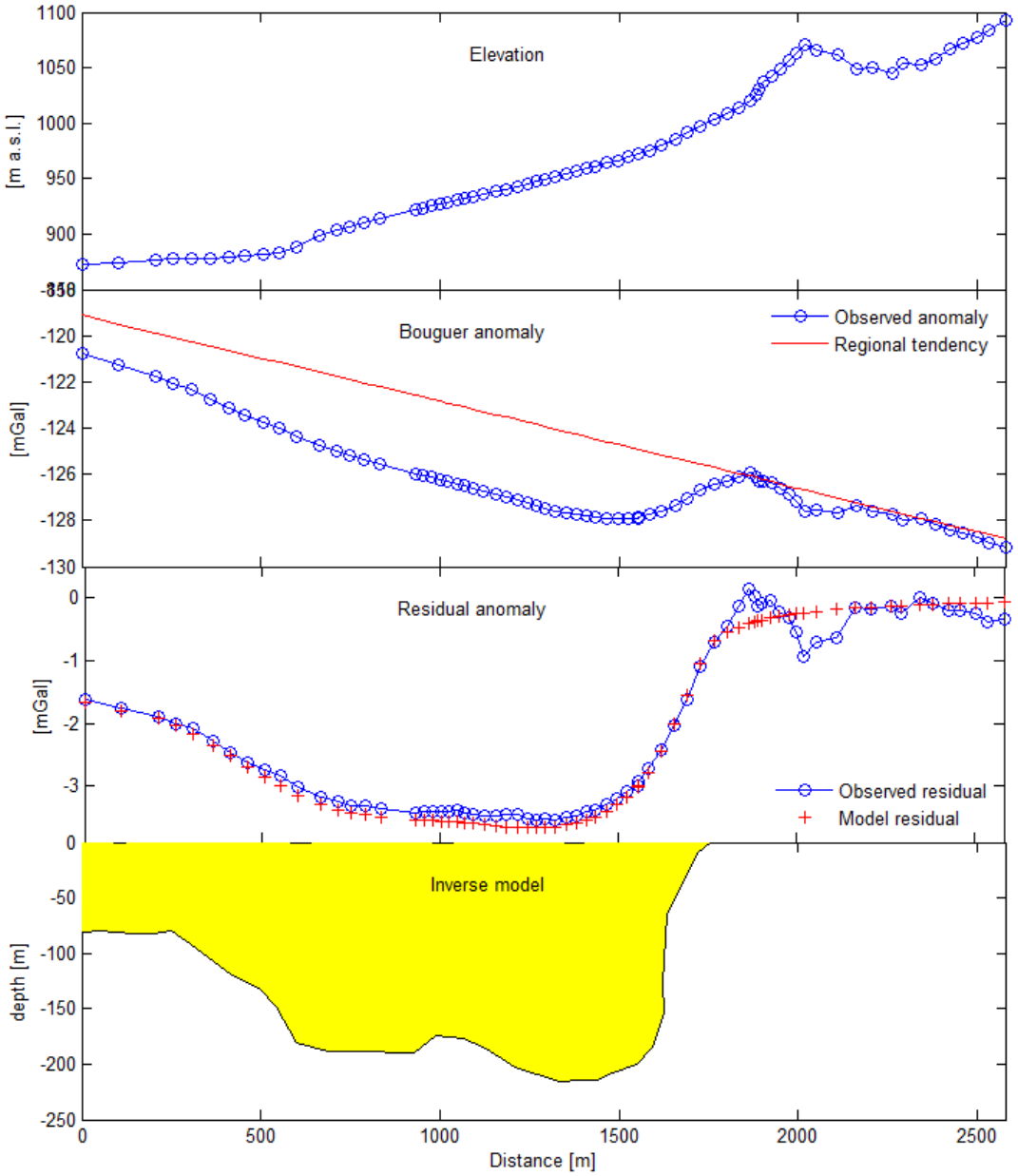

Figure A-1. shows an example of modelling, upper panel show the topography of the profile, second upper panel is the bouguer gravity and the regional effect, the regional effect was adjusted with the gravity trend on the rock (from 1900 to 2500 meters approximately). The third graph shows the residual gravity anomaly and the modeled gravity, and finally it is the modeled body which represent the geometry of the sedimentary infilling in depth.

A.3 Density of rocks and soils.

Density is physical property that changes in each type of rock or soil, according to its mineralogical composition and porosity. Knowing the density of rocks and soil allows a more accurate and robust modeling of gravity anomalies, even if they are samples taken on the surface.

In this work we measured 3 samples of the Las Chilcas Fm. obtained in site 1, and 3 samples of the Abanico Fm. obtained in site 2. In addition, I incorporate in this compilation the densities obtained by Bustamante et al., 2012, taken in samples of the same geological units. The density values of both the Abanico Fm. and Las Chilcas Fm. were compared with values obtained by Yáñez *et al.* (2015) further south, in the Santiago basin. Although the rocks correspond to the same unit, density variations may be due to local mineralogical changes and fracture intensity of the measured samples (Carmichael 1989). Table A.1 shows the mean density of both formations in g/cm^3. As can be seen, the densities obtained in this work are lower compared to the other two studies. This may be due to the fact that the samples selected had a considerable degree of alteration and a high degree of fracture, because all samples collected were taken close (less than 200 m) to the main trace of PFZ.

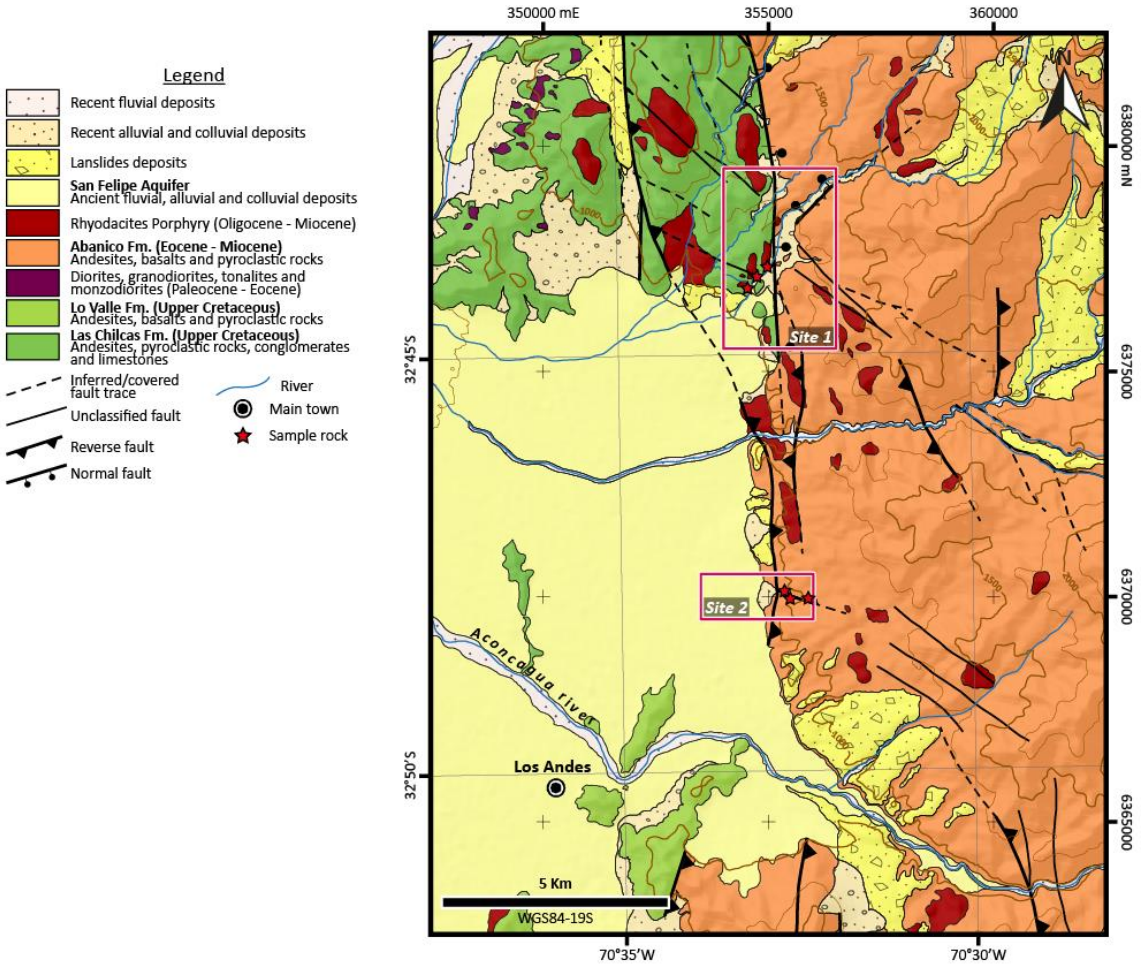

Figure A-2. Location of rock samples for density measurements.

On the other hand, the mean density of soils was estimate with density contrast in agreement with results in the Santiago Basin (Yáñez *et al.* 2015), in addition this value is consistent for this type of soil. Table A.2 shows the density variability for end member soil types. The wide range of values is due to the fact that a soil can present different percentages of a particle size that will make the soil more or less dense. The sediments observed in the field correspond to alluvial deposits, mostly poorly selected gravelly sands to graves.

Table A-1. Mean density of rocks of main geological formations in this study. Density in grams per cubed centimeter (g/cm3).

	This work	Bustamante et al., 2012	Yañéz et al., 2015
Abanico Fm.	2.45	2.64	2.62
Las Chilcas Fm.	2.57	2.70	2.63

Table A-2. Soil density according to particle size classification (from Carmichael 1989; Telford *et al.* 1990).

Soil type	Range (g/cm^3)	Average (g/cm^3)
Clay	1.6 - 2.6	2.2
Sand	1.7 - 2.3	2.0
Gravel	1.7 - 2.4	2.0

A.4 Modelling of anomalies

The residual gravity anomaly was modeled in ModelVision software by estimating the regional effect and computing the geometry of the sedimentary infilling. For each gravity profile, data was uploaded into the software (position X, Y and bouguer gravity), then through a process of forward modelling the basin geometry is determined. The forward modeling procedure considers a fixed density contrast, while the basin geometry is adjusted recursively until reaching a close match between the observed and modeled bouguer gravity.

Basement depth at sites 1 and 2 (Figure 2-7) was constrained by resistivity models which made it possible to estimate the density contrast between the basement and the sediment. Average adjustment error ~ 0.2 mGal, being less than ~0.15 in the basin. The segments of

the profile with the lowest adjustment occur in high frequency sections, corresponding to measurements made upstream of the main trace of the PFZ. This discrepancy could be associated with topographic effects not fully resolved by topographic corrections based on a DEM without enough resolution. As shown in Figure A-1, the sediment fill geometry (yellow body) is referenced to zero level, but in order to be interpreted in conjunction with the electrical model and geology, it was adjusted to the topography of the profile as shown in Figure A-2.

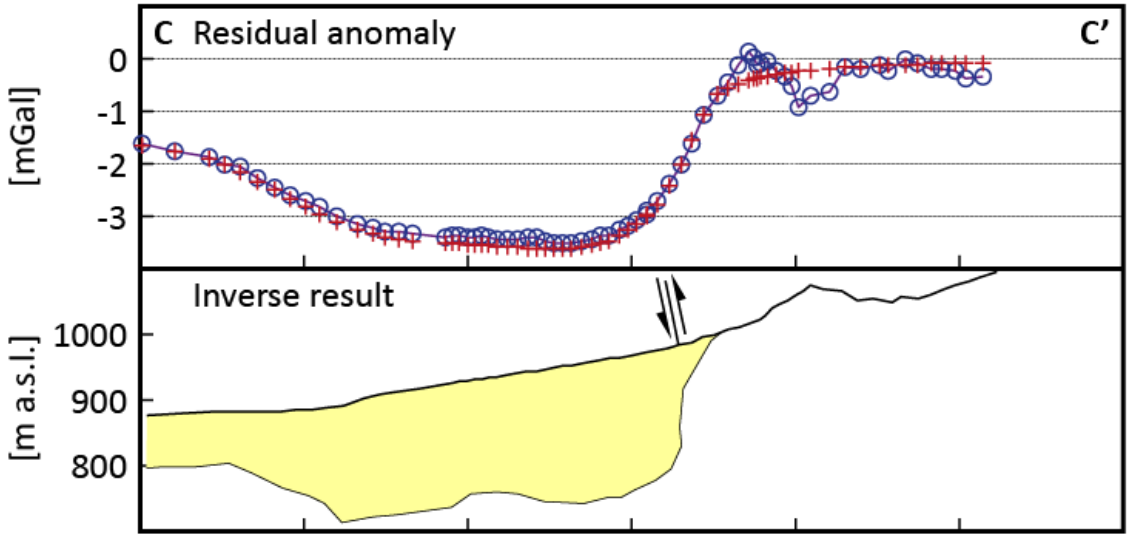

Figure A-3. Gravity Data. Residual gravity anomaly observed and modeled, and down geometry of contact between the sedimentary infilling and the basement.

APPENDIX B: "FUNDAMENTALS OF ELECTRICAL DC MEASUREMENTS"

This method is based on Ohm´s law and Maxwell´s equations, and provides a tool to determine the resistivity of the subsurface. This technic employs and artificial source of current, which is introduced into the ground through electrodes. In order to obtain the resistivity of the subsurface, potential voltage is measured at electrodes in the vicinity of the current injection, providing a mechanism to determine resistivity structure of the subsurface.

B.1 Current electrodes at subsurface

Consider a continuous current flowing in an isotropic homogeneous medium. If δa is an element of surface and J the current density in [A m^{-2}], then the current passing through δa is $J\cdot \delta a$. The current density J and the electric field E are related through Ohm´s Law, where E is in [V m^{-1}] and σ is the conductivity of the medium in [S m^{-1}] (Telford et al., 1990):

$$J= \sigma E \qquad (B.1)$$

As the electric field is the gradient of a scalar potential, and using the Eq. B.1

$$J= -\sigma \nabla V \qquad (B.2)$$

Considering continuity and without electrical sources, charge does not accumulate to any extent during current flow, therefore $\nabla\cdot J = 0$, so

$$\nabla\cdot (\sigma \nabla V)= 0 \qquad (B.3)$$

Applying some vector operations, the Eq. B.3 could be expressed as

$$\nabla \sigma \nabla V + \sigma \nabla^2 V = 0 \qquad \text{(B.4)}$$

If the conductivity σ is constant in all space, the Eq. B.4 simplifies to the Laplace´s equation, represented by a harmonic

$$\nabla^2 V = 0 \qquad \text{(B.5)}$$

Considering two boundary conditions that must hold at any contact between two mediums with different conductivity, 1) the electric field tangential to interface is continuous (n x ($E_1 + E_2$) = 0), and 2) the current density normal to interface is continuous (n · ($\sigma_1 E_1 + \sigma_2 E_2$) = 0), or in terms of electrical potential:

$$V_1 = V_2 \qquad \text{(B.6)}$$

To solve Eq. B.5 in a homogeneous medium, considering a point charge and using spherical coordinates, the potential V is function of the distance between two electrodes (r).

$$\nabla^2 V = \frac{\partial^2 V}{\partial r^2} + \frac{2}{r} \frac{\partial V}{\partial r} = 0 \qquad \text{(B.7)}$$

Multiplying by r^2 and integrating twice, it gets

$$V = -\frac{A}{r} + B \qquad \text{(B.8)}$$

Where A and B are constant determined by boundary conditions. Because V = 0 when r $\rightarrow \infty$, it gets B = 0. The total current flow on a spherical surface is $I = 4 \pi r^2 J$, and from Eq. B.2, the resistivity is $\rho = 1/\sigma$, and the first derivate of Eq. B.8, the solution A would be

$$I = 4\,\pi\,r^2\,J = -4\,\pi\,r^2\sigma\,\frac{\partial\,V}{\partial\,r} = -4\,\pi\,r^2\sigma\,A \rightarrow\ A = -\frac{2\,I\,\rho}{4\,\pi} \tag{B.9}$$

Replacing B.9 in Eq. B.8

$$V = \left(\frac{I\,\rho}{2\,\pi}\right)\frac{1}{r}\ \text{ or }\ \rho = \frac{2\,\pi\,r\,V}{I} \tag{B.10}$$

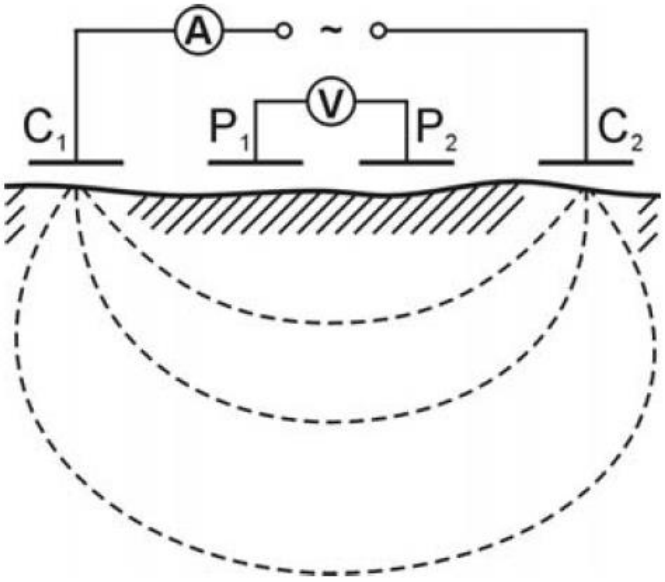

Figure B-1. Basic array electrode for resistivity DC method

When the distance between two electrodes is defined as in Figure B-1, the potential will be affected by both current electrodes. Thus, the total potential in P_1 of C_1 and C_2

$$V_1 + V_2 = \frac{I\,\rho}{2\,\pi}\left(\frac{1}{r_1} - \frac{1}{r_2}\right) \tag{B.11}$$

Introducing a second potential electrode P_2, the difference potential between P_1 and P_2 is

$$\Delta\,V = \frac{I\,\rho}{2\,\pi}\left(\left(\frac{1}{r_1} - \frac{1}{r_2}\right) - \left(\frac{1}{r_3} - \frac{1}{r_4}\right)\right) \tag{B.12}$$

B.2 Electrical resistivity of rocks and its relationship with permeability

The electrical resistivity of the medium (rock or soil) depends of the mineralogy, porosity, pore size distribution and connectivity, degree of water saturation and electrical resistivity of the fluid (solute concentration) (Grant and West 1965; McCarter 1984; Samouëlian *et al.* 2005). Both rocks and soils have a three-phase composite, solid particles, water, and air. The air medium is infinitively resistive, the water resistivity is a function of the ionic concentration dissolve in it, and the resistivity of the solid particles is related to the electrical charges density at the surface of the constituents (Samouëlian *et al.* 2005). The resistivity of a rock or soil will depend on the overall resistivity response of these three parts, so a rock or soil can have a very large range of electrical resistivity (e.g. in Table B.1).

Table B-1. Typical ranges of electrical resistivities of some rocks and soils (from Samouëlian et al., 2005)

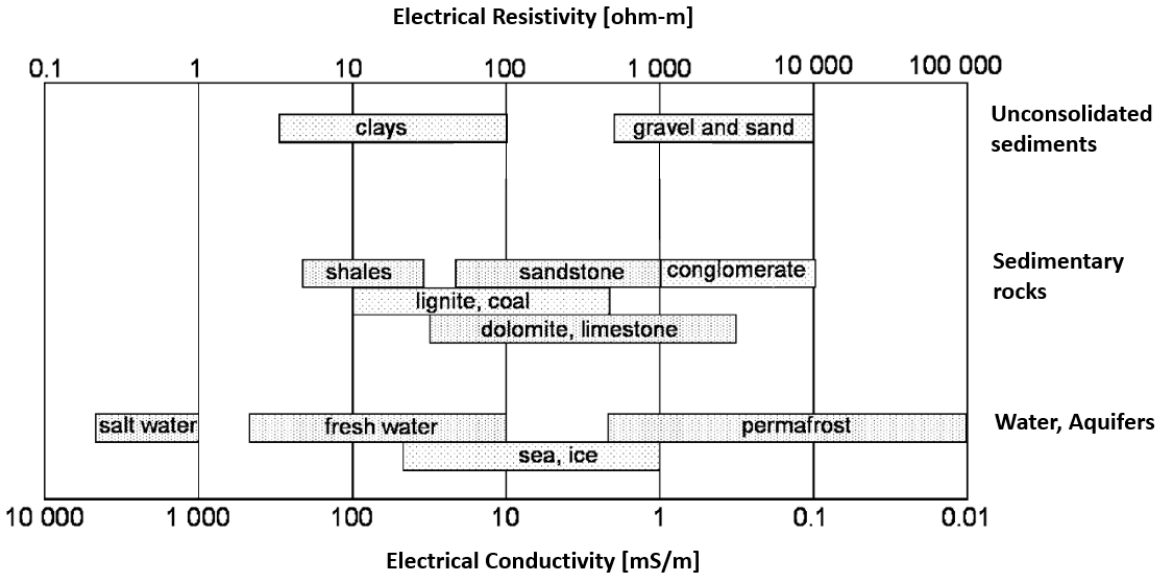

The geometry of the pores, both distribution and shape, determines the proportion of air and water that the medium have. The porosity can be obtained through the Archie´s law, which for a saturated rocks or soils (in absence of clay) is written as:

$$F = \frac{\rho}{\rho_w} = \alpha\, \phi^{-m} \qquad \text{(B.12)}$$

Where the proportionality factor F is called formation factor, ρ and ρ_w are the resistivity of the medium and the resistivity of the pore water, respectively, α and m are constants called coefficient of saturation and cementation factor, respectively, and ϕ is the porosity. The cementation factor depends directly on the geometry of the pores, as it depends on the size, shape, and connectivity of the pores. This value varies from 1.3 to 2.0, being values from 1.3 to 1.5 for unconsolidated sands, up to 1.8-2.0 for consolidated sandstones. Archie´s law is only applicable in the absence of clay, due to the fact that the presence of clay reduces the resistivity of the medium because clay minerals have an electrically active surface layer. The molecular structure of the clays contemplates tetrahedral and octahedral layers, where the substitution of Al^{+4}, Fe^{+2} or Mg^{+3} leaves a negative net charge. To maintain electrical neutrality, the clay particle attracts cations to its surface from its surroundings, which are not part of the crystalline structure of the clay (Samouëlian *et al.* 2005). These cations are extracted from the aqueous solution surrounding the clay and may be replaced by other ions when the clay is altered and/or the aqueous medium changes. While some of these released ions and polar water molecules hold firmly to the surface, others hold less tightly in a diffuse, but moving, layer that extends into the solution. These ions diffuse into the solution as a result of the concentration gradient but are also retained by the voltage gradient of the negatively charged clay surface. This

diffuse layer has a higher conductivity than the normal porous fluid and represents a parallel path of low resistivity for current flow along mineral surfaces. Clay particles have an enormous area per unit weight and, consequently, a relatively small amount of clay can considerably decrease the resistivity of the medium (Mitchell 2005).

On the other hand, the water content and resistivity of water can decrease the resistivity of the medium by up to 3 orders of magnitude. If the medium is completely saturated with water (pores 100% filled with water without air), it will facilitate the conduction of current having a lower resistivity than when the medium is partially saturated or dry. In addition, if the pore water has a greater dissolution of ions, it will transmit the current more easily, so that a saline water (high electrical conductivity) will cause the medium to have less resistive. Kalinski and Kelly (1993) (in Samouëlian et al., 2005), demostred that according to Archie´s law, pore water resistivity and water content influence the resistivity response of the medium. Figure B-2 shows graphically the effect of both factors.

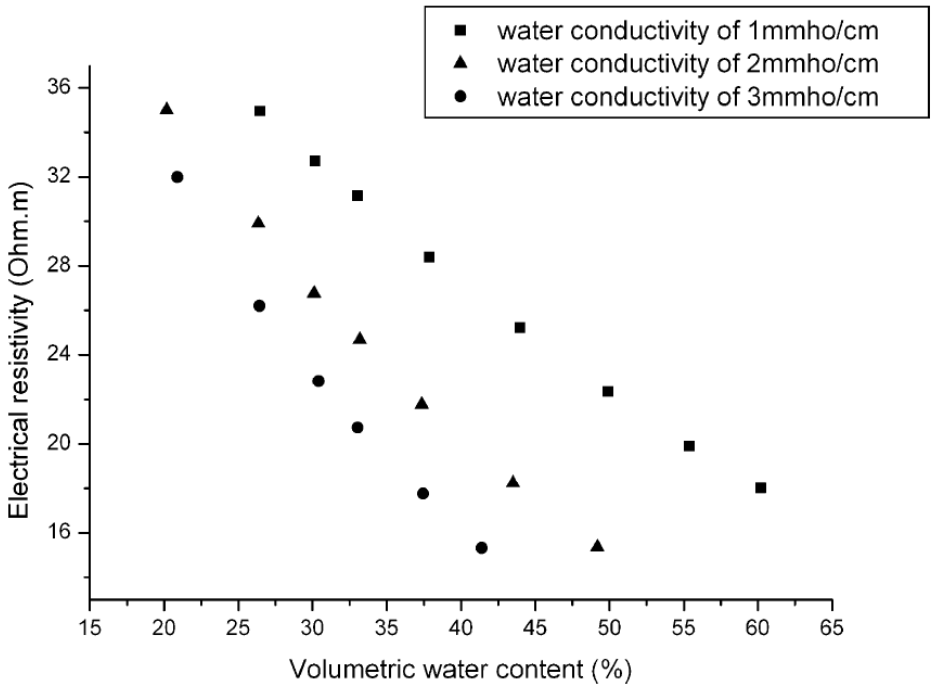

Figure B-2. Relationship between the volumetric water content and resistivity for different values of pore water conductivity (from Kalinski and Kelly (1993) in Samouëlian et al., 2005).

As mentioned above, the Archie´s law provides a mechanism to estimate the porosity of the medium from resistivity observation (bulk and water solution), and expected cementation factor. Given the link between porosity and permeability (providing that clay is not present), the estimate of the former allows a first order approximation on the medium permeability. Figure B-3 shows how the resistivity of a medium as a function of the porosity and cementation factor, where the greatest effect is due to the porosity of the medium which can affect resistivity by up to two orders of magnitude. On the other hand, the resistivity will increase directly with the cementation factor, but it will not generate a variation greater than half an order of magnitude.

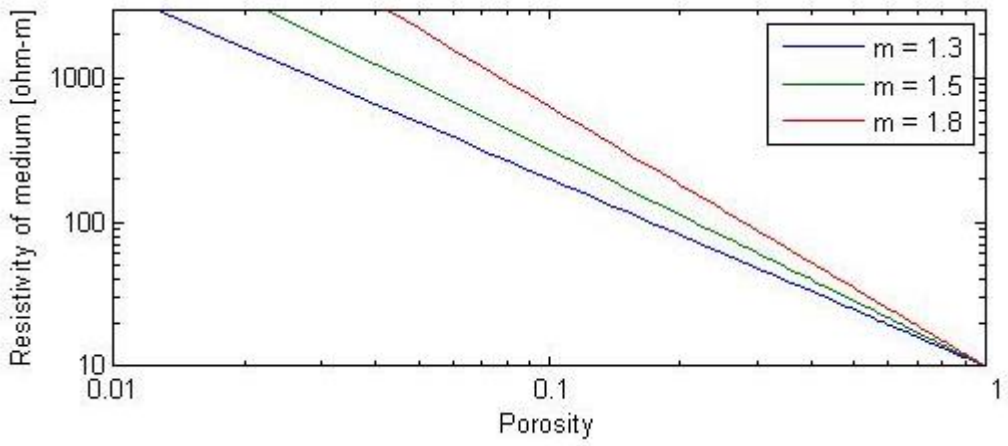

Figure B-3. Theorical resistivity of medium for different values of porosity, using Archie´s law with three different cementation factors and a resistivity of the pore water of 10 ohm-m.

B.3 Resistivity modelling

The term ρ of Eq. B.12 is known as apparent resistivity and it represents the subsurface when this is homogeneous isotropic for any electrode array. However, in nature the ground is heterogenous, and the apparent resistivity corresponds to the integral of the total current flow in all the pathway, so it should not be directly interpreted geologically. Then, in order to determine the distribution of resistivity of the subsoil, the apparent resistivity must be modeled.

Before to model the apparent resistivity, data were filtered because there were very high errors in some measurements. The measured data were analyzed according to the error of each measurement, and it was established to filter out the data with an error greater than 50 %. This error is directly associated with the contact resistance of the electrodes, when contact resistance is high, less current will inject the equipment, then the potential difference in the medium could be so low that the equipment could not detect it. In

addition, to characterize the resistivity distribution at greater depths it is necessary to inject greater current, to overcome the background noise. So, it is important to emphasize that in the field it is necessary to have contact resistances in each electrode as low as possible (lower than 500 ohm). Figure B-4 compares two examples where the influence of contact resistance on the frequency of higher errors is observed.

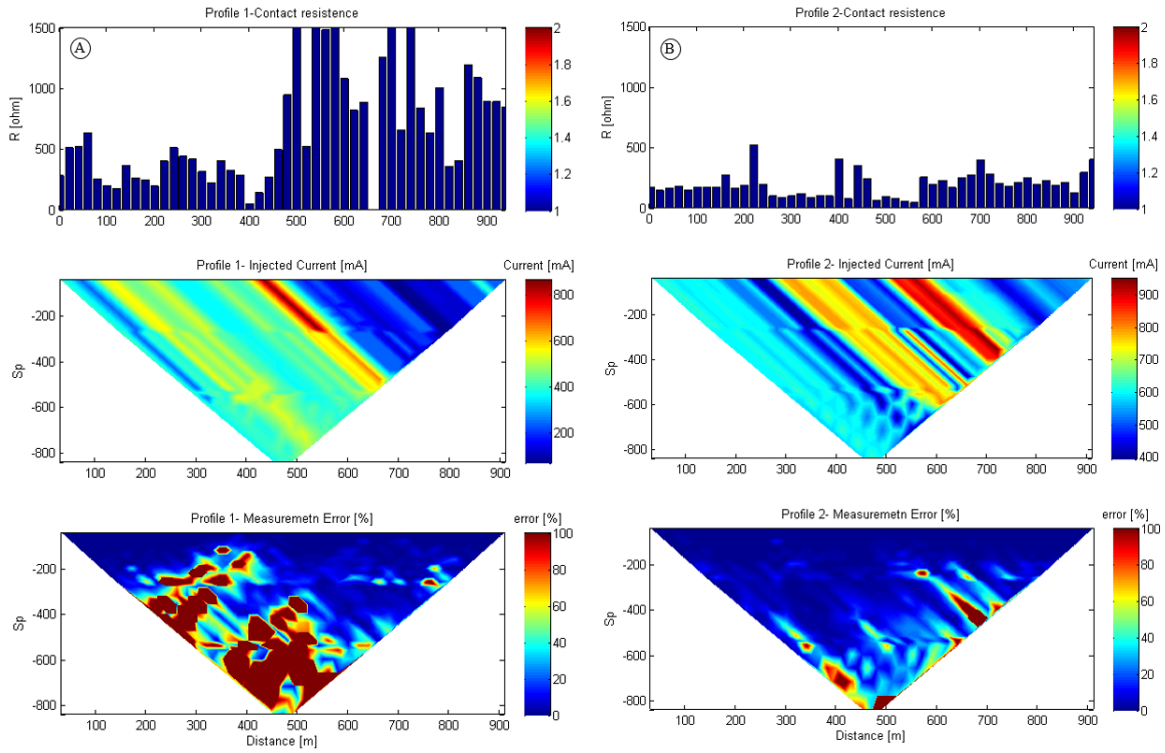

Figure B-4. Comparison between two profiles, where A has poor contact resistances, while B has all good contact resistances.

After filtering the data, as it is mentioned above, the apparent resistivity integrates the intrinsic resistivities and geometry of the medium and the electrical array used. The resistivity distribution of the subsurface is determined through forward and/or inverse models. In this study it was used the software ZonRes2D which uses Finite-element method as mathematical tool to solve forward and inverse problem.

Through the apparent resistivity obtained by the equipment Terrameter LS2, ZonRes2D allows to approximate the observations to the response of a given resistivity model. Figure B-5 is an example of modelling, upper and middle sections are the observations and model response apparent resistivity, respectively. The aim of the modeling effort is to approximate, as much as possible, observations and model response by modifying the resistivity model (lower section).

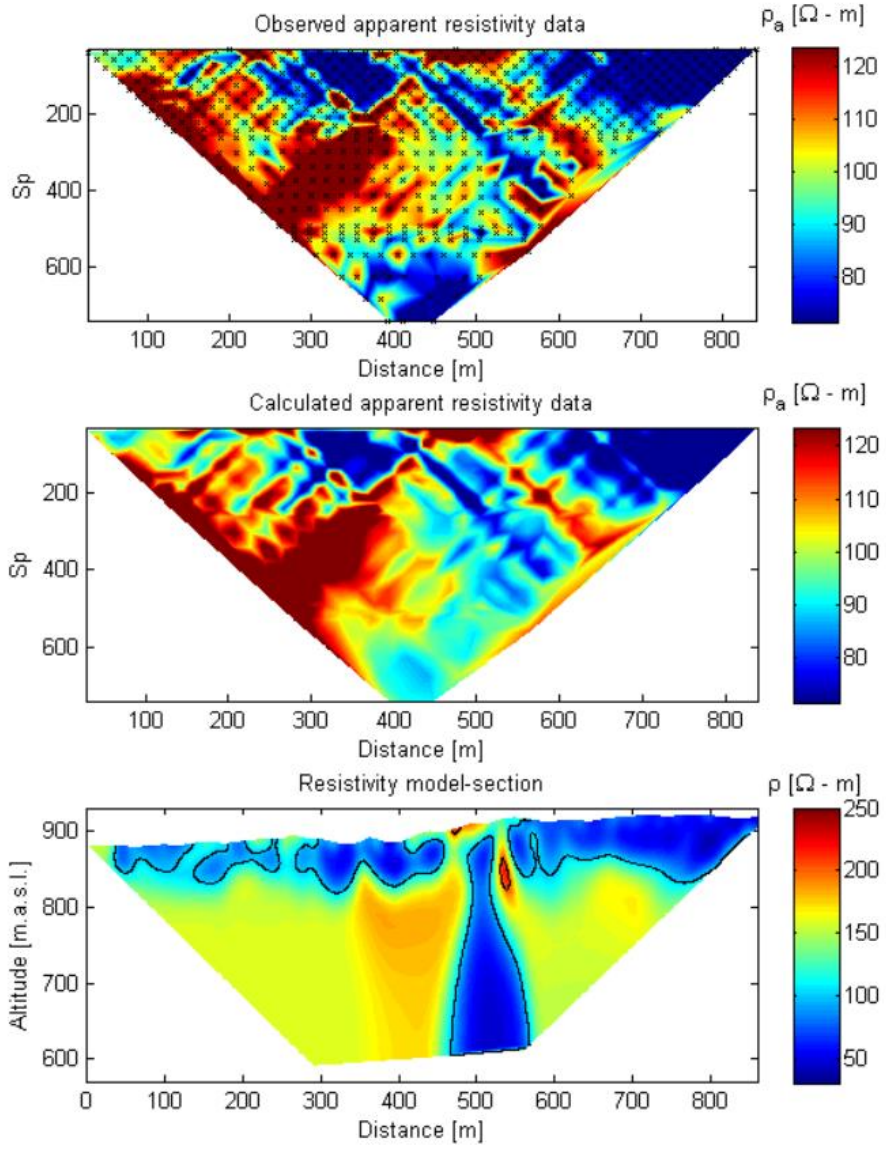

Figure B-5. Resistivity sections using in ZonRes2D to model. From top to bottom, first the observed apparent resistivity, then the calculated apparent resistivity, and finally the resistivity model.

APPENDIX C: "GPS COORDINATE ADJUSTMENT WITH SPECIFIC SPACING"

Profile and electrode location are based on simple GPS measurements. However due to the presence of vegetation (especially high trees) the location obtained by standard GPS was not consistent with the characteristics of the cables used (a total cable length of 940 m with electrodes every 20 m). The Figure C-1 shows the distance between each electrode obtained by the GPS position originally. It is observed that the GPS-based distance between electrodes do not have the expected constant value (20m), and in addition the measured length of the arrangement is not correct (total cable length of 940 m).

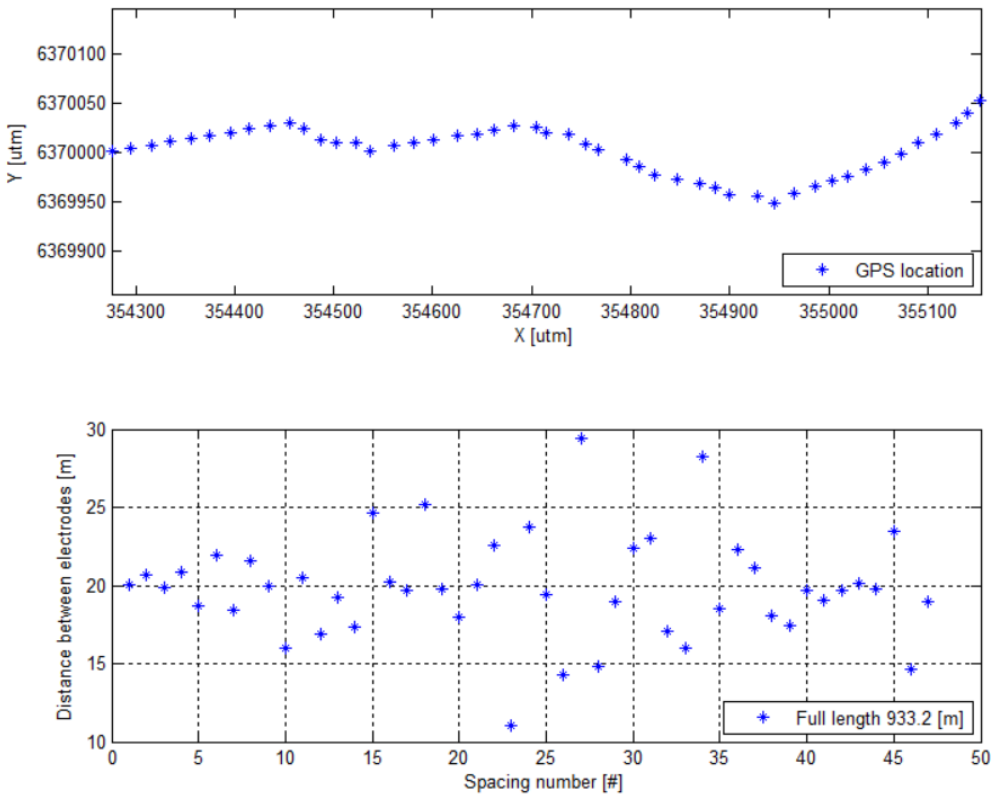

Figure C-1. Electrode locations, plant view (upper panel). Also, distance between two continuous electrodes (lower panel).

Since the standard GPS has an error that can be 15 m in the horizontal components, it was considered a maximum distance to correct of 15 m for each component (x and y or N-S and E-W). In this manner, it is fixed the first electrode and another 47 electrodes were relocated one by one from the first electrode such that the distance between the first and second electrode is 20 m, and so on. Each correction was an iterative process where the mobile electrode was added or subtracted from 10 cm in each direction until the distance between the two electrodes was 20 m. Figure C-2 shows the same profile as Figure C-1 with the new location of each electrode (cyan points), where it can be seen that the modified distances do not significantly alter the geometry of the profile. Lower panel shows the distance that was corrected for each electrode in comparison to the original location.

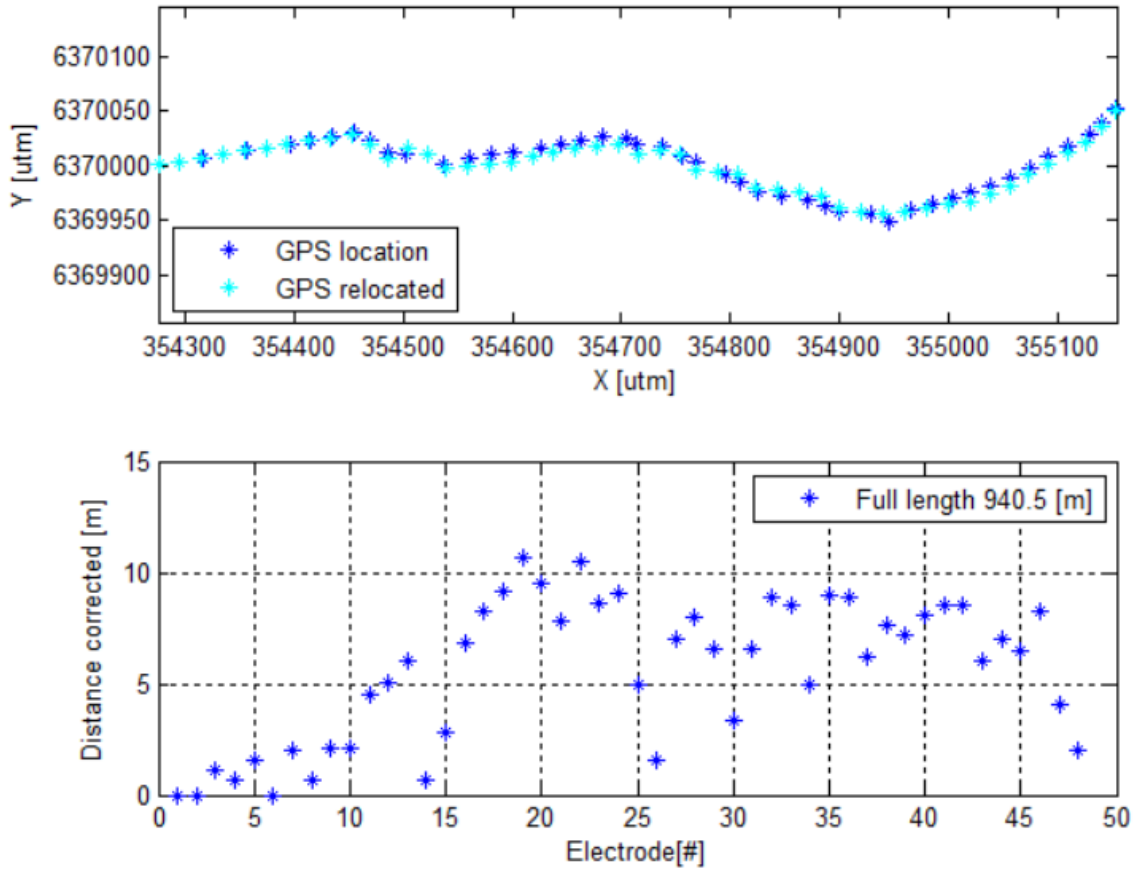

Figure C-2. (upper panel) Comparison between location and relocation of electrodes, plant view. (lower panel) Corrected distance between each spacing.

The following code was developed to correct this problem

```
%%%% MATLAB Code%%%%
```

```
name = 'Topo_TC_02.xyz';            %relative distance/X/Y/Z
data = load (name);

corr = 0;
create = false;                              %CREA NUEVO ARCHIVO DE
COORDENADAS
distance = false;                            %crea archivo de distancias
proyectadas sobre recta

x1 = data(1,2);
y1 = data(1,3);
x2 = data(length(data),2);
y2 = data(length(data),3);
vector = [x1,y1; x2,y2];
figure (1)

x_lin=x1:20:x2;
p=polyfit(data(:,2),data(:,3),1);
plot(x_lin,p(1)*x_lin+p(2),'k')
hold on

for i=1:length(data)
q = [data(i,2),data(i,3)];
[prj_po]=proj(vector,q);
axis equal
hold on
plot(q(1),q(2),'b*')
hold on
plot(prj_po(1),prj_po(2),'r*')
hold on
clear q prj_po
end

figure
vect=[x_lin(1),p(1)*x_lin(1)+p(2);x_lin(length(x_lin)),p(1)*x_lin(lengt
h(x_lin))+p(2)];
sum_up=0;
sum_dw=0;
if distance
    fidh=fopen(['Distance',name,'.xyz'],'wt');
end
for i=1:length(data)
q = [data(i,2),data(i,3)];
[prj_po2]=proj(vect,q);
axis equal
hold on
plot(q(1),q(2),'b*')
hold on
plot(prj_po2(1),prj_po2(2),'r*')
hold on
new_sec(i,1) = prj_po2(1);
new_sec(i,2) = prj_po2(2);
```

```
d(i) = sqrt((new_sec(i,1) - new_sec(1,1))^2 + (new_sec(i,2) -
new_sec(1,2))^2);
if data(i,3) - prj_po2(2) > 0
    sum_up=sum_up+sqrt((prj_po2(1)-data(i,2))^2 + (prj_po2(2)-
data(i,3))^2);
else
    sum_dw=sum_dw+sqrt((prj_po2(1)-data(i,2))^2 + (prj_po2(2)-
data(i,3))^2);
end
if distance
    fprintf(fidh,'%4.1f \n',d(i)+corr);
end
clear q prj_po
end
for i=1:length(data)-1
    dist(i) = sqrt((data(i,2)-data(i+1,2))^2 + (data(i,3)-
data(i+1,3))^2);
end

figure (99)
subplot(2,1,2)
plot(dist,'*')
grid on
xlabel('Spacing number [#]')
ylabel('Distance between electrodes [m]')
suma =sum(dist);
legend(['Full length ',num2str(suma,'%.1f'),'
[m]'],'Location','southeast')
set(gcf,'color','w');
xw = [data(:,2),data(:,3)];
for iii=1:length(data)-1
x0 = [xw(iii,1),xw(iii,2)];
xf = [xw(iii+1,1),xw(iii+1,2)];
for i=1:120
    for ii=1:20
        s0 = sqrt((x0(1) - (xf(1)))^2 + (x0(2) - (xf(2)))^2);
        s4 = sqrt((x0(1) - (xf(1) + i*0.5))^2 + (x0(2) - (xf(2) +
ii*0.5))^2);
        s2 = sqrt((x0(1) - (xf(1) + i*0.5))^2 + (x0(2) - (xf(2) -
ii*0.5))^2);
        s3 = sqrt((x0(1) - (xf(1) - i*0.5))^2 + (x0(2) - (xf(2) -
ii*0.5))^2);
        s1 = sqrt((x0(1) - (xf(1) - i*0.5))^2 + (x0(2) - (xf(2) +
ii*0.5))^2);

        s5 = sqrt((x0(1) - (xf(1) - i*0.5))^2 + (x0(2) - (xf(2) ))^2);
        s6 = sqrt((x0(1) - (xf(1) + i*0.5))^2 + (x0(2) - (xf(2) ))^2);
        s7 = sqrt((x0(1) - (xf(1) ))^2 + (x0(2) - (xf(2) - ii*0.5))^2);
        s8 = sqrt((x0(1) - (xf(1) ))^2 + (x0(2) - (xf(2) + ii*0.5))^2);
        if abs (s0 - 20 ) <0.1
            break;
        elseif abs (s1 - 20 ) <0.05
            break;
```

```
106             elseif abs (s2 - 20 ) <0.05
107                 break;
108             elseif abs (s3 - 20 ) <0.05
109                 break;
110             elseif abs (s4 - 20 ) <0.05
111                 break;
112             elseif abs (s5 - 20 ) <0.05
113                 break;
114             elseif abs (s6 - 20 ) <0.05
115                 break;
116             elseif abs (s7 - 20 ) <0.05
117                 break;
118             elseif abs (s8 - 20 ) <0.05
119                 break;
120             else
121             end
122         end
123         format longG
124             if abs (s0 - 20 ) <0.1
125                 xfi = xf(1);
126                 yfi = xf(2);
127                 break;
128             elseif abs (s1 - 20 ) <0.05
129                 xfi = xf(1) - i*0.5;
130                 yfi = xf(2) + ii*0.5;
131                 break;
132             elseif abs (s2 - 20 ) <0.05
133                 xfi = xf(1) + i*0.5;
134                 yfi = xf(2) - ii*0.5;
135                 break;
136             elseif abs (s3 - 20 ) <0.05
137                 xfi = xf(1) - i*0.5;
138                 yfi = xf(2) - ii*0.5;
139                 break;
140             elseif abs (s4 - 20 ) <0.05
141                 xfi = xf(1) + i*0.5;
142                 yfi = xf(2) + ii*0.5;
143                 break;
144             elseif abs (s5 - 20 ) <0.05
145                 xfi = xf(1) - i*0.5;
146                 yfi = xf(2) ;
147                 break;
148             elseif abs (s6 - 20 ) <0.05
149                 xfi = xf(1) + i*0.5;
150                 yfi = xf(2) ;
151                 break;
152             elseif abs (s7 - 20 ) <0.05
153                 xfi = xf(1) ;
154                 yfi = xf(2) - ii*0.5;
155                 break;
156             elseif abs (s8 - 20 ) <0.05
157                 xfi = xf(1) ;
158                 yfi = xf(2) + ii*0.5;
159                 break;
```

```
160             else
161             end
162     end
163
164     xw(iii+1,1) = xfi;
165     xw(iii+1,2) = yfi;
166     end
167     subplot(3,1,1)
168     plot(data(:,2),data(:,3),'b*')
169     set(gcf,'color','w');
170     axis equal
171     hold on
172     hold on
173     plot (xw(:,1),xw(:,2),'c*')
174     legend('GPS location','GPS relocated','Location','southwest')
175     curtick = get(gca, 'XTick');
176     set(gca, 'XTickLabel', cellstr(num2str(curtick(:))));
177     curtick = get(gca, 'YTick');
178     set(gca, 'YTickLabel', cellstr(num2str(curtick(:))));
179     xlabel('X [utm]')
180     ylabel('Y [utm]')
181     for j=1:length(data)-1
182         dist2(j) = sqrt((xw(j,1)-xw(j+1,1))^2 + (xw(j,2)-xw(j+1,2))^2);
183     end
184     for jj=1:length(data)
185         corr(jj) = sqrt((data(jj,2)-xw(jj,1))^2 + (data(jj,3)-xw(jj,2))^2);
186     end
187     sum (dist2)
188     subplot(3,1,2)
189     plot(dist2,'*')
190     grid on
191     xlabel('Spacing number [#]')
192     ylabel('Distance between electrodes [m]')
193     legend(['Full length ',num2str(sum (dist2),'%.1f'),'
194     [m]'],'Location','southeast')
195     set(gcf,'color','w');
196     ylim([10 30])
197     subplot(3,1,3)
198     plot(corr,'*')
199     grid on
200     xlabel('Electrode[#]')
201     ylabel('Distance corrected [m]')
202     set(gcf,'color','w');
203
204
205      if create
206     fidh2 = fopen([name,'_repost.xyz'],'wt');
207     for i=1:length(data)
208         fprintf(fidh2,'%4.1f %6.1f %7.1f %4.1f \n',...
209                 20*(i-1),xw(i,1),xw(i,2),data(i,4));
210     end
211      end
212     fclose all;
```

APPENDIX D: "PROCESSING TO CORRECT NO-STRAIGHT PROFILES OF ELECTRICAL RESISTIVITY TOMOGRAPHY"

As indicated in Appendix B, the apparent resistivity obtained for the equipment (in this study a Terrameter LS2) depends on the type of arrangement used (dipole-dipole). However, the apparent resistivity calculated considers an ideal situation in which all the electrodes are collinear. The real situation is not necessarily the ideal, geomorphology and plantations hamper the deployment of straight profiles in several cases (e.g. Figure C-1). This situation impacts the geometrical factor, distorting the apparent resistivity computation if theoretical spatial conditions are not corrected by the actual location of each electrode. Figure D-1 shows graphically the problem that needs to be solved, which compares the ideal and real situation. The Eq. D.1 (derived from Eq. B.12) allows to calculate the apparent resistivity, where the term that depends on the location of the electrodes is called geometrical factor G.

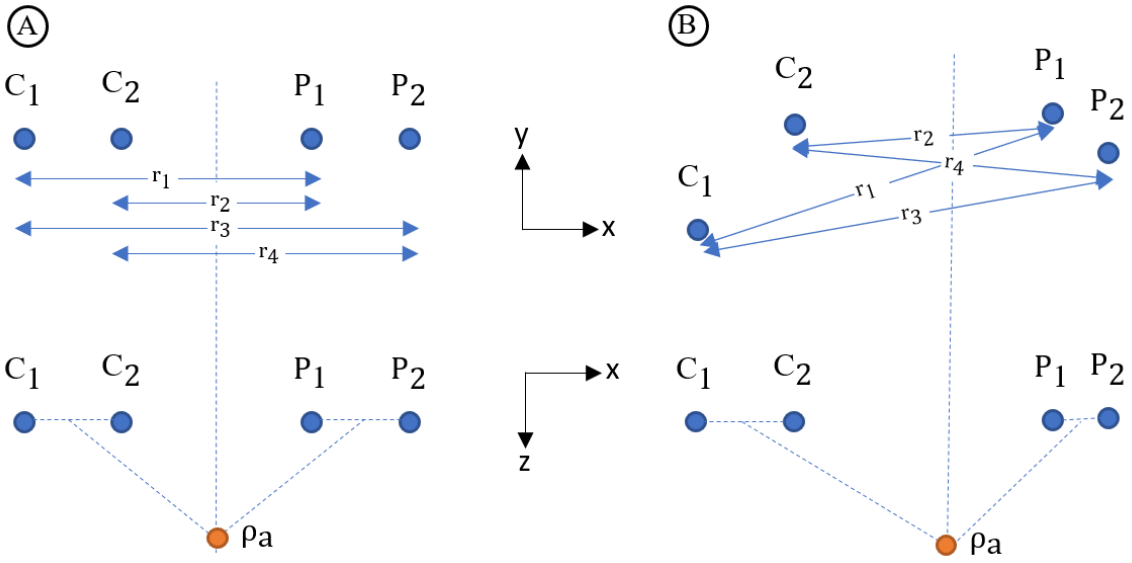

Figure D-1. ideal situation versus real situation. C1 and C2 represent electrode of current, P1 and P2 are electrode of potential, and ρa is the point location of the apparent resistivity measurement. (a) it is an ideal situation where the electrodes are aligned and equidistant, and (b) it is the real situation where electrodes are no-aligned and no-equidistant.

$$\rho_a = \frac{2\,\pi\,\Delta V}{I}\,\frac{1}{\left(\frac{1}{r_1}-\frac{1}{r_2}\right)-\left(\frac{1}{r_3}-\frac{1}{r_4}\right)} \text{ or } \rho_a = \frac{2\,\pi\,\Delta V}{I}\,G \qquad \text{(D.1)}$$

In order to correct this problem, the following data processing was carried out. The geometrical factors G were recalculated considering the real positions of each electrode. For this purpose, in each measurement the distance of the dipoles of that measurements were calculated (r_1, r_2, r_3 and r_4) and used in Eq. D.1. Figure D-2 shows the difference between the geometric factors re-calculated and those given by the instrument, and also show how they impact on the apparent resistivity.

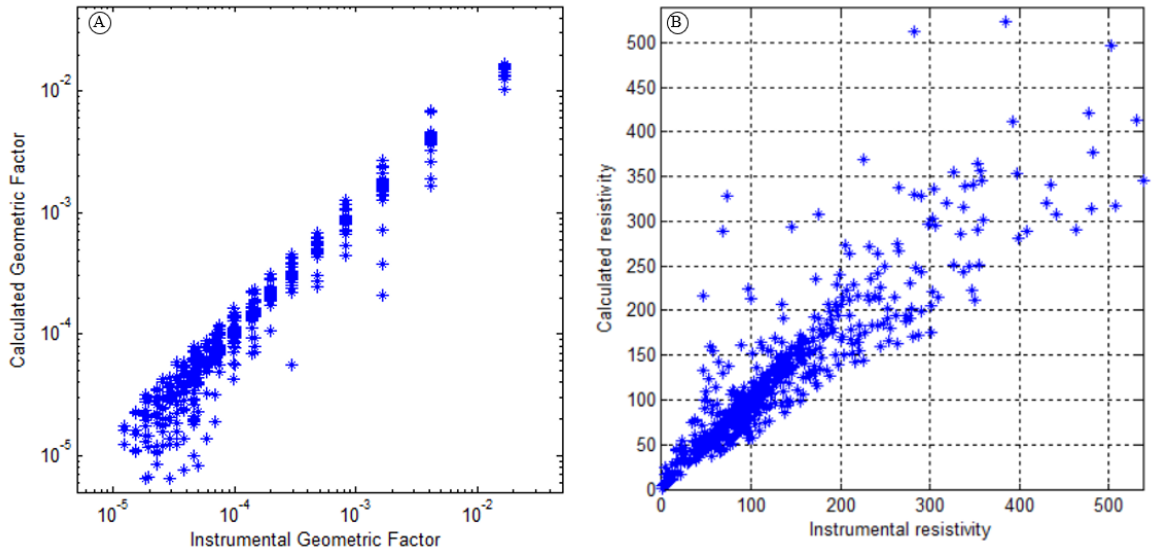

Figure D-2. (a) ratio between instrumental and calculated geometrical factor. (b) ratio between instrumental and calculated apparent resistivity.

Because ZondRes2D allows 2D modeling, data was projected on an approximate straight line by minimum squares according to the distribution of the apparent resistivity location. In addition, it is necessary to emphasize that apparent resistivity sections represent measurement points that are in the vicinity of the profile, and are not necessarily coplanar to the profile, due to this is not straight. Eventually, the recalculated apparent resistivity section would be different from the one obtained directly when the electrode profile is more irregular, whereas they would be the same when the electrode profile is straight. Figure D-3 shows an example of no straight profile, the dipoles midpoint location and the straight line where the apparent resistivity were projected. Dipoles midpoints are the location of each measurement corresponding to the distance between the center of the current dipole and the center of the potential dipole. Figure D-4 shows the direct apparent

resistivity and the recalculated resistivity obtained from the profile shown in Figure B-3, that is the most irregular profile in this study.

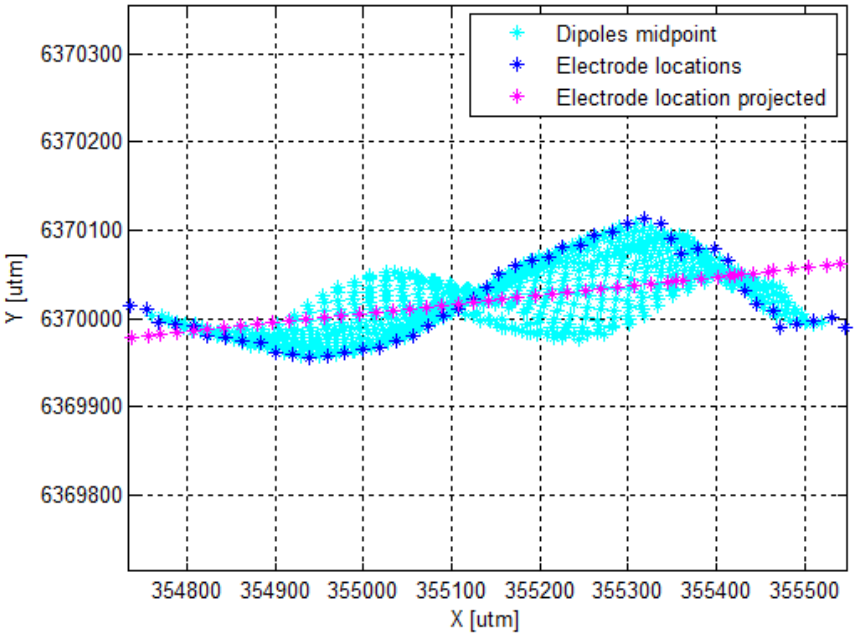

Figure D-3. Example of profile no-straight where cyan points represent the location of dipoles midpoint, blue points are the location of the electrodes, and magenta points are the location where the blue points were projected.

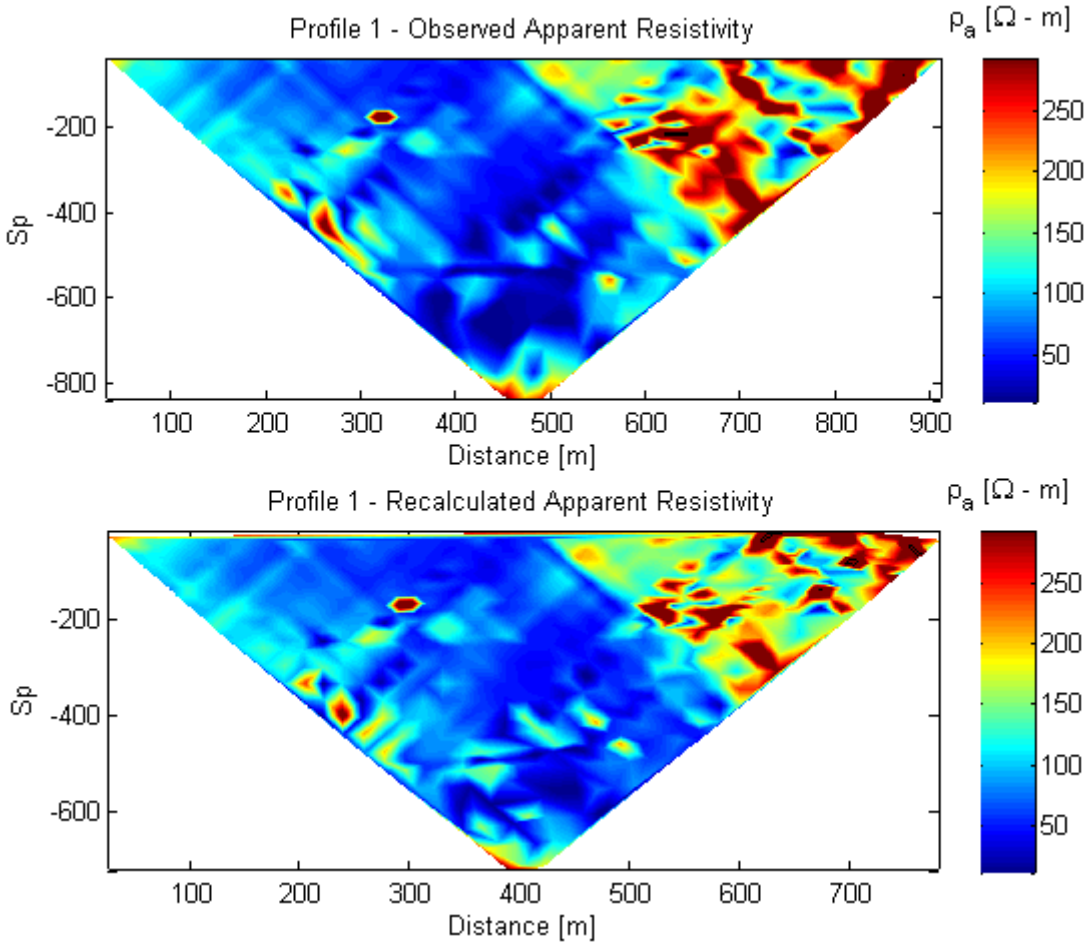

Figure D-4. Comparison of an ERT section before and after their values were recalculated.

As shown in Figure D-2.b, the apparent resistivity may range from two-thirds to twice the value estimated by the instrument, when the electrode profile is not stretched and straight. Because the distance between the electrodes is variable, the measured apparent resistivity may be greater or less than expected. However, as shown in Figure D-4 the texture of the section does not vary significantly, but changes in the intensity and shape of the apparent resistivity domains can be identify. The importance of making this correction is due to the

fact that when considering an apparent resistivity that is not representative of the medium, it causes a distorted resistivity modeling and a subsequent erroneous interpretation of the subsurface.

The following code was developed to process de electrical data.

```
%%%%%% MATLAB Code %%%
```

```
clear all
close all
clc

iii=1;                                  %numero de perfil

move = [458.5,0];
dx=move(iii);                          %corrije distancia global
name=['TC0',num2str(iii),'_Dip-dip7_1'];
fid=fopen([name,'.txt']);
[data] = lee_ert(fid);
topo=load(['Topo_TC_0',num2str(iii),'_repost.xyz']);
Cres = load(['TC0',num2str(iii),'_contact_resistence.txt']);

corr = 1;
error_limit = 50;                       %error tolerable
up_value = 2500;                        %filtra valores superior a este

show = false;                          %MUESTRA GRAFICOS
new_py = false;
%crea archivo con FG recalculado y proyectado a una recta

%% grafica recta de acuerdo a ubicacion de estacas
x1 = topo(1,2);
y1 = topo(1,3);

x2 = topo(size(topo(:,2)),2);
y2 = topo(size(topo(:,2)),3);

x_lin=x1:20:x2;
p=polyfit(topo(:,2),topo(:,3),1);

vector = [x1,y1; x2,y2];
vect=[x_lin(1),p(1)*x_lin(1)+p(2);x_lin(length(x_lin)),p(1)*x_lin(lengt
h(x_lin))+p(2)];
sum_up=0;
sum_dw=0;

for i=1:length(topo)
q = [topo(i,2),topo(i,3)];
[prj_po]=proj(vector,q);
[prj_po2]=proj(vect,q);
new_sec(i,1) = prj_po2(1);
new_sec(i,2) = prj_po2(2);
d(i) = sqrt((new_sec(i,1) - new_sec(1,1))^2 + (new_sec(i,2) -
new_sec(1,2))^2);
if topo(i,3) - prj_po2(2) > 0
    sum_up=sum_up+sqrt((prj_po2(1)-topo(i,2))^2 + (prj_po2(2)-
topo(i,3))^2);
else
    sum_dw=sum_dw+sqrt((prj_po2(1)-topo(i,2))^2 + (prj_po2(2)-
topo(i,3))^2);
```

```
53  end
54  clear q prj_po prj_po2
55  end
56  for i=1:length(topo)-1
57      dist(i) = sqrt((topo(i,2)-topo(i+1,2))^2 + (topo(i,3)-
58  topo(i+1,3))^2);
59  end
60
61  %%
62  C1 = data.ax/corr;
63  C2 = data.bx/corr;
64  P1 = data.mx/corr;
65  P2 = data.nx/corr;
66  xd=((C1+C2)/2 + (P1+P2)/2)/2;
67  yd=((C1+C2)/2 - (P1+P2)/2);
68
69  for i=1:length(data.R)
70  FG(i)=data.R(i)*2*pi/data.rho(i);          % factor geometrico
71  instrumental
72
73  Ram = sqrt((C1(i)-P1(i)))^2;
74  Rbm = sqrt((C2(i)-P1(i)))^2;
75  Ran = sqrt((C1(i)-P2(i)))^2;
76  Rbn = sqrt((C2(i)-P2(i)))^2;
77
78  fg(i)=1/Ram - 1/Rbm - 1/Ran + 1/Rbn;
79  end
80  clear Ram Rbm Ran Rbn
81
82  for i=1:length(data.R)
83  pos1=find(topo(:,1)==data.ax(i)/corr);
84  xc1=topo(pos1,2);
85  yc1=topo(pos1,3);
86  pos2=find(topo(:,1)==data.bx(i)/corr);
87  xc2=topo(pos2,2);
88  yc2=topo(pos2,3);
89  pos3=find(topo(:,1)==data.mx(i)/corr);
90  xp1=topo(pos3,2);
91  yp1=topo(pos3,3);
92  pos4=find(topo(:,1)==data.nx(i)/corr);
93  xp2=topo(pos4,2);
94  yp2=topo(pos4,3);
95
96  Ram = sqrt((xc1-xp1)^2+(yc1-yp1)^2);
97  Rbm = sqrt((xc2-xp1)^2+(yc2-yp1)^2);
98  Ran = sqrt((xc1-xp2)^2+(yc1-yp2)^2);
99  Rbn = sqrt((xc2-xp2)^2+(yc2-yp2)^2);
100
101 FG_cal(i)=1/Ram - 1/Rbm - 1/Ran + 1/Rbn;
102
103 C1_r(i) = sqrt((xc1 - topo(1,2))^2 + (yc1 - topo(1,3))^2);
104 C2_r(i) = sqrt((xc2 - topo(1,2))^2 + (yc2 - topo(1,3))^2);
```

```
105   P1_r(i) = sqrt((xp1 - topo(1,2))^2 + (yp1 - topo(1,3))^2);
106   P2_r(i) = sqrt((xp2 - topo(1,2))^2 + (yp2 - topo(1,3))^2);
107   C1_rp(i) = d(pos1);
108   C2_rp(i) = d(pos2);
109   P1_rp(i) = d(pos3);
110   P2_rp(i) = d(pos4);
111
112   Ram_p = sqrt((d(pos1)-d(pos3))^2);
113   Rbm_p = sqrt((d(pos2)-d(pos3))^2);
114   Ran_p = sqrt((d(pos1)-d(pos4))^2);
115   Rbn_p = sqrt((d(pos2)-d(pos4))^2);
116   FG_py (i) = 1/Ram_p - 1/Rbm_p - 1/Ran_p + 1/Rbn_p;
117   %Factor geometrico reproyectado sobre recta de tendencia
118   x_m(i) = ((xc1 + xc2)/2 + (xp1 + xp2)/2)/2;
119   y_m(i) = ((yc1 + yc2)/2 + (yp1 + yp2)/2)/2;
120   end
121   figure(1)
122
123   x0 = topo(1,2);
124   y0 = topo(1,3)-100;
125
126   b1=plot(x_m -x0,y_m -y0,'c*');
127   hold on
128   b2=plot(topo(:,2)-x0,topo(:,3)-y0,'b*');
129   hold on
130   b3=plot(new_sec(:,1)-x0,new_sec(:,2)-y0,'m*');
131   hold off
132   axis equal
133   grid on
134   legend([b1 b2 b3],'Dipoles midpoint','Electrode locations','Electrode
135   location projected','Location','northwest')
136   set(gcf,'color','w');
137   ylim([6369900-y0 6370200-y0])
138   xlim([min(topo(:,2))-x0 max(topo(:,2))-x0])
139   xlabel('X [m]')
140   ylabel('Y [m]')
141
142   xd_r=((C1_rp+C2_rp)/2 + (P1_rp+P2_rp)/2)/2;
143   yd_r=((C1_rp+C2_rp)/2 - (P1_rp+P2_rp)/2);
144
145   for i=1:length(data.R)
146   rho_cal(i)=data.R(i)*2*pi/FG_cal(i);
147   end
148
149   %%%%%%%
150   figure(99)
151   plot(data.rho,rho_cal,'*')
152   axis([0 max(data.rho) 0 max(data.rho)])
153   set(gcf,'color','w');
154   xlabel('Instrumental resistivity')
155   ylabel('Calculated resistivity')
156   axis square
157   grid on
```

```
158
159   figure (200)
160   loglog(abs(FG),abs(FG_cal),'*')
161   xlabel('Instrumental Geometric Factor ')
162   ylabel('Calculated Geometric Factor')
163   set(gcf,'color','w');
164   axis square
165   axis([5*10^-6 5*10^-2 5*10^-6 5*10^-2])
166
167   %%%%%%%%%%%%%%%%%%%%%%
168   v=data.rho;
169   vd=rho_cal;
170   x = 0:0.5:max(P2);
171   y = min(yd):0.5:0;
172   [X,Y] = meshgrid(x,y);
173
174   res_min=mean(rho_cal)-1.2*std(rho_cal);
175   res_max=mean(rho_cal)+2*std(rho_cal);
176
177   x=xd; y=yd; rho=data.rho;
178   xqq= (min(x):1:max(x))';
179   ny=(max(y)-min(y))/length(xqq);
180   yqq= (min(y):ny:max(y))';
181   yqq(length(xqq)+1)=[];
182   [xqz,yqz]=meshgrid(xqq,yqq);
183   nrho=nan(length(xqq),length(xqq));
184
185   for i = 1:length(xqq)
186       xq=xqz(:,i); yq=yqz(:,i);
187       nrho(:,i)=griddata(x,y,rho,xq,yq);
188   end
189
190   if show                          %MUESTRA COMPARACION ENTRE AMBOS
191   figure(100)
192   subplot(2,1,1)
193   s=pcolor(xqq,yqq,nrho);
194   shading flat;
195   s.FaceColor='interp';
196   caxis([res_min res_max])
197   set(gcf,'color','w');
198   colormap('jet')
199   hold on
200   pbaspect([1 0.408 1])
201   title(['Profile ',num2str(iii),' - Observed Apparent Resistivity'])
202   set(gca,'FontSize',10)
203   ylabel('Sp','FontSize',10)
204   xlabel('Distance [m]','FontSize',10)
205   hcb=colorbar;
206   title(hcb,'\rho_a [\Omega - m]','FontSize',10)
207   hcb.FontSize = 10;
208   contour(xqq,yqq,nrho,[500 1000 1500 2000 2500 3000],'k');
209
```

```
clear X Y x y rho

x=xd_r; y=yd_r; rho=rho_cal;
xqq= (min(x):1:max(x))';
ny=(max(y)-min(y))/length(xqq);
yqq= (min(y):ny:max(y))';
yqq(length(xqq)+1)=[];
[xqz,yqz]=meshgrid(xqq,yqq);
nrho=nan(length(xqq),length(xqq));

for i = 1:length(xqq)
    xq=xqz(:,i); yq=yqz(:,i);
    nrho(:,i)=griddata(x,y,rho,xq,yq);
end

subplot(2,1,2)
s=pcolor(xqq,yqq,nrho);
shading flat;
s.FaceColor='interp';
caxis([res_min res_max])
set(gcf,'color','w');
colormap('jet')
hold on
pbaspect([1 0.408 1])
title(['Profile ',num2str(iii),' - Recalculated Apparent Resistivity'])
set(gca,'FontSize',10)
ylabel('Sp','FontSize',10)
xlabel('Distance [m]','FontSize',10)
hcb=colorbar;
title(hcb,'\rho_a [\Omega - m]','FontSize',10)
hcb.FontSize = 10;
contour(xqq,yqq,nrho,[500 1000 1500 2000 2500 3000],'k');

clear X Y vq x y rho

x=xd; y=yd; rho=data.error;
xqq= (min(x):1:max(x))';
ny=(max(y)-min(y))/length(xqq);
yqq= (min(y):ny:max(y))';
yqq(length(xqq)+1)=[];
[xqz,yqz]=meshgrid(xqq,yqq);
nrho=nan(length(xqq),length(xqq));
for i = 1:length(xqq)
    xq=xqz(:,i); yq=yqz(:,i);
    nrho(:,i)=griddata(x,y,rho,xq,yq);
end

figure(101)
subplot(3,1,3)
s=pcolor(xqq,yqq,nrho);
shading flat;
s.FaceColor='interp';
caxis([0 100])
```

```
263   set(gcf,'color','w');
264   colormap('jet')
265   hold on
266   pbaspect([1 0.408 1])
267   title(['Profile ',num2str(iii),'- Measuremetn Error [%]'])
268   set(gca,'FontSize',10)
269   ylabel('Sp','FontSize',10)
270   xlabel('Distance [m]','FontSize',10)
271   hcb=colorbar;
272   title(hcb,'error [%]','FontSize',10)
273   hcb.FontSize = 10;
274
275   clear X Y x y rho
276
277   x=xd; y=yd; rho=data.amp;
278   xqq= (min(x):1:max(x))';
279   ny=(max(y)-min(y))/length(xqq);
280   yqq= (min(y):ny:max(y))';
281   yqq(length(xqq)+1)=[];
282   [xqz,yqz]=meshgrid(xqq,yqq);
283   nrho=nan(length(xqq),length(xqq));
284   for i = 1:length(xqq)
285       xq=xqz(:,i); yq=yqz(:,i);
286       nrho(:,i)=griddata(x,y,rho,xq,yq);
287   end
288
289   subplot(3,1,2)
290   s=pcolor(xqq,yqq,nrho);
291   shading flat;
292   s.FaceColor='interp';
293   caxis([min(rho) max(rho)])
294   set(gcf,'color','w');
295   colormap('jet')
296   hold on
297   pbaspect([1 0.408 1])
298   title(['Profile ',num2str(iii),'- Injected Current [mA]'])
299   set(gca,'FontSize',10)
300   ylabel('Sp','FontSize',10)
301   hcb=colorbar;
302   title(hcb,'Current [mA]','FontSize',10)
303   hcb.FontSize = 10;
304
305   clear X Y
306   subplot(3,1,1)
307   bar(Cres(:,1),Cres(:,4))
308   pbaspect([1 0.408 1])
309   axis([0 940   0 1500])
310   ylabel('R [ohm]')
311   colorbar
312   title(['Profile ',num2str(iii),'-Contact resistence'])
313   end
314
315   %%
```

```
316  if new_py
317  fidh=fopen([name,'_filter_',num2str(error_limit),'_projected_v3_newFG.d
318  at'],'wt');
319
320  if head;
321      fprintf(fidh,'Dip-dip7_1\n');
322      fprintf(fidh,'20\n');
323      fprintf(fidh,'11\n');
324      fprintf(fidh,'3\n');
325      fprintf(fidh,'Type of measurement
326  (0=app.resistivity,1=resistance)\n');
327      fprintf(fidh,'1\n');
328      fprintf(fidh,'%i\n',ndatos);
329      fprintf(fidh,'2\n');
330      fprintf(fidh,'11\n');
331      fprintf(fidh,'Chargeability\n');
332      fprintf(fidh,'mV/V\n');
333      fprintf(fidh,'10 0.01 0.02 0.02 0.04 0.06 0.1 0.14 0.2 0.3 0.44
334  0.66 2 2\n');
335  end
336  %%
337  for i=1:length(data.R)
338      R_new(i)=rho_cal(i)*FG_py(i)*0.5/pi;
339  end
340
341  for i=1:length(data.R)
342      if data.error(i)>error_limit || rho_cal(i)>up_value ||
343  rho_cal(i)<0;
344
345      else
346       fprintf(fidh,'4  %i    0 %i  0  %i 0     %i 0     %.8f     %.8f
347  %.8f     %.8f     %.8f     %.8f     %.8f     %.8f     %.8f     %.8f
348  %.8f\n',...
349            C1_rp(i)/corr +dx,C2_rp(i)/corr +dx,P1_rp(i)/corr
350  +dx,P2_rp(i)/corr +dx,R_new(i),data.ip1(i),...
351
352  data.ip2(i),data.ip3(i),data.ip4(i),data.ip5(i),data.ip6(i),...
353            data.ip7(i),data.ip8(i),data.ip9(i),data.ip10(i));
354      end
355  end
356  if head
357      for i=1:7
358      fprintf(fidh,'0\n');
359      end
360  end
361  fclose all;
362  end
```

APPENDIX E: "SENSITIVITY TEST OF RESISTIVITY MODELS"

This Annex shows the inversions of all the ERT section out of this study. Each figure shows the observed/field measurement apparent resistivity, then the calculated apparent resistivity, and finally the resistivity model. On site 1 (Figure 2-8) there were 9 sections, 7 compose the A-A profile, and 4 independent sections transversal to the A-A profile . On site 2 (Figure 2-9) there were 4 sections, 2 sections that compose the A-A profile, and two independent sections transversal to the A-A profile . In addition, in both sites the section with the LRSB (site 1 section 7, and site 2 section 2, Figure E-1 and E-9 respectively) is shown alternatives models that resolve the resistivity observations.

E.1 Site 1

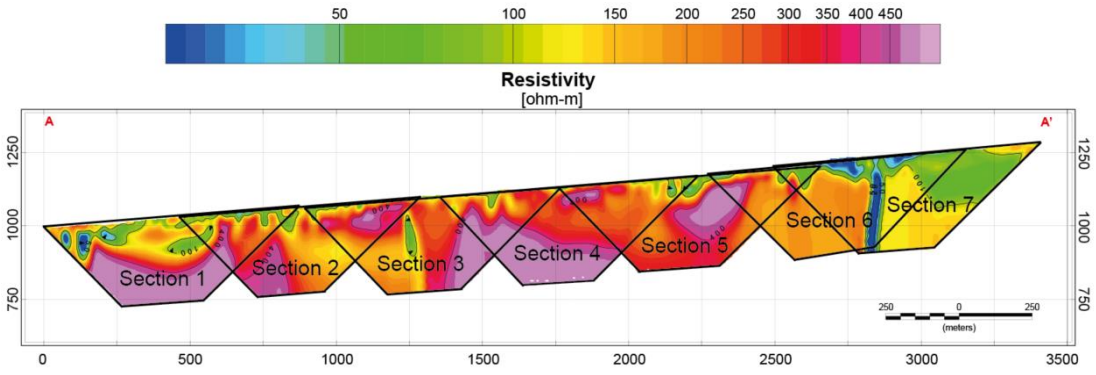

Figure E-1. A-A' profile and details of each section that compound this profile.

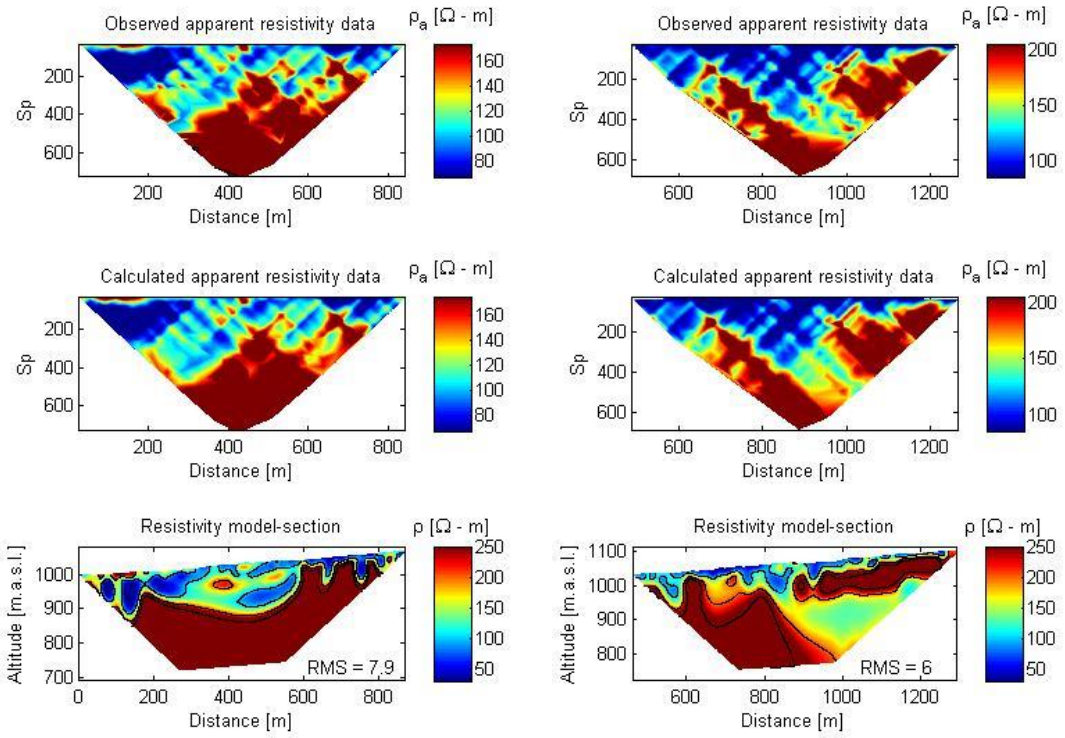

Figure E-2. A-A' profile, (left) section 1 and (right) section 2.

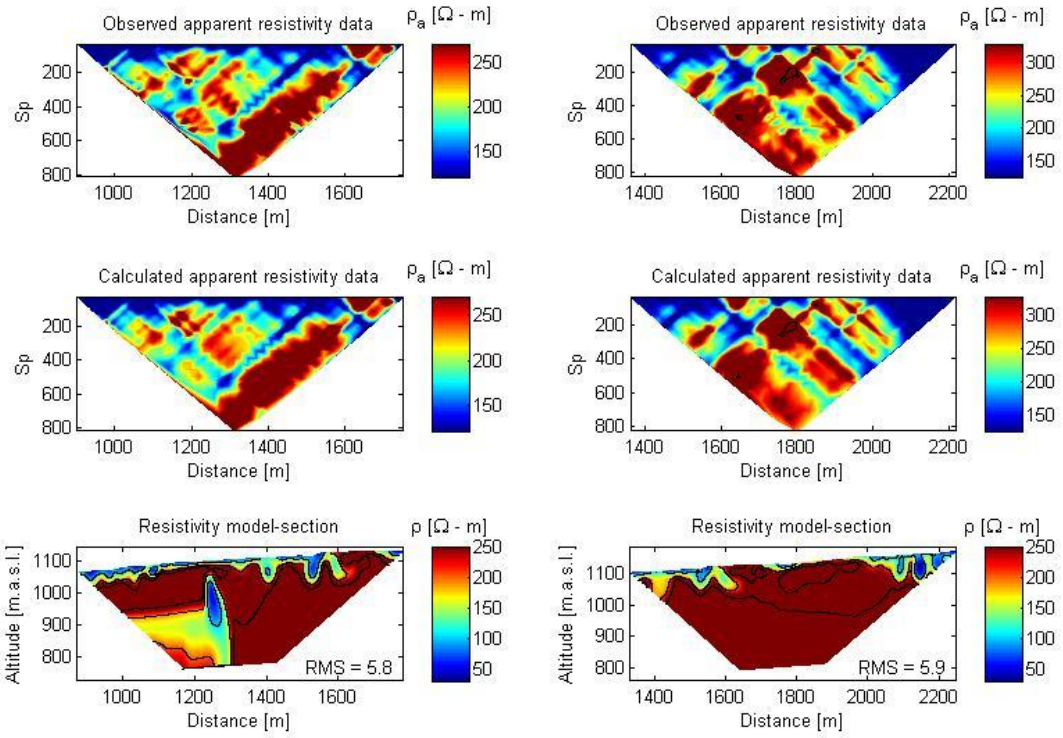

Figure E-3. A-A’ profile, (left) section 3 and (right) section 4.

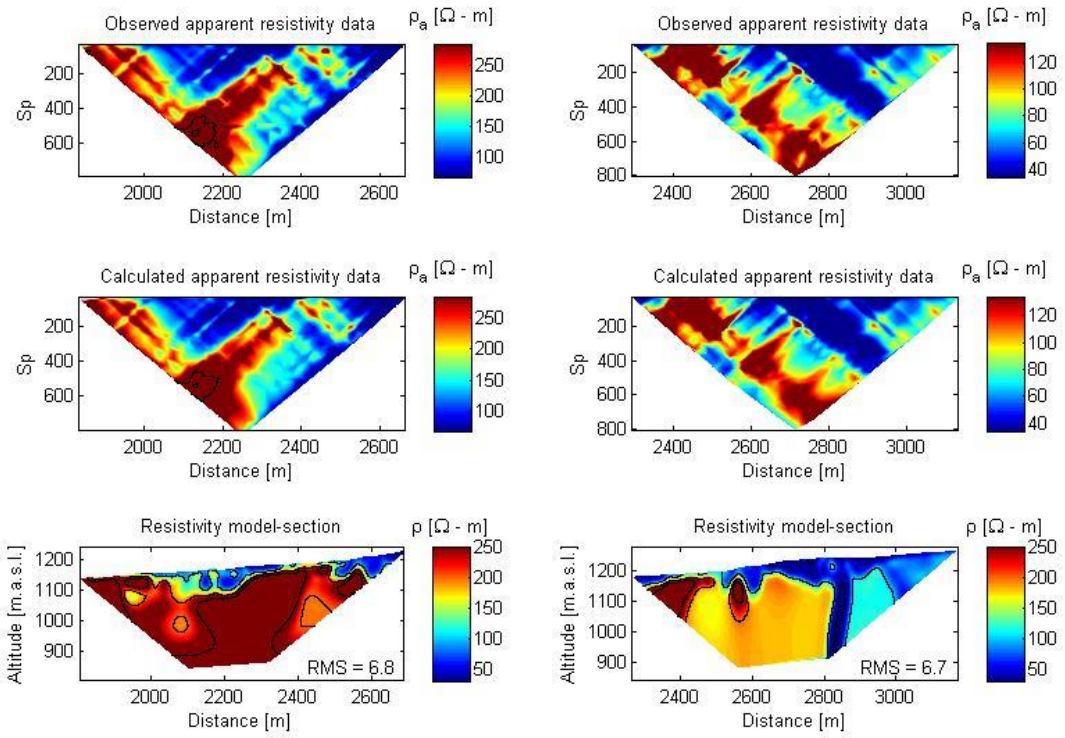

Figure E-4. A-A’ profile, (left) section 5 and (right) section 6.

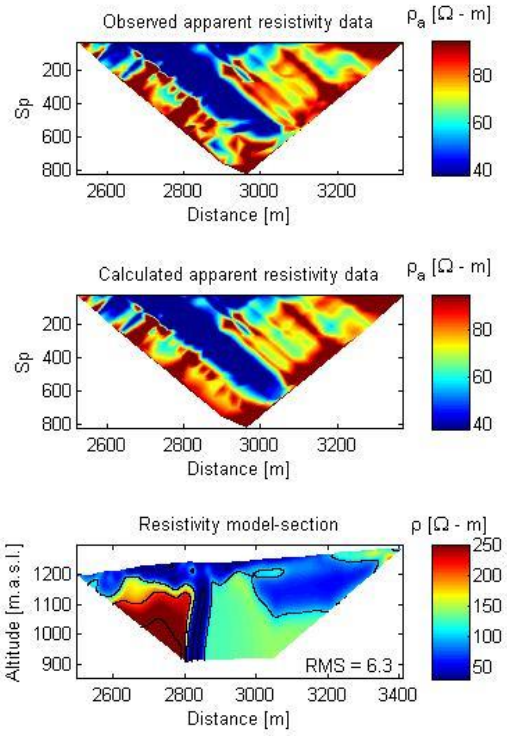

Figure E-5. A-A’ profile, section 7.

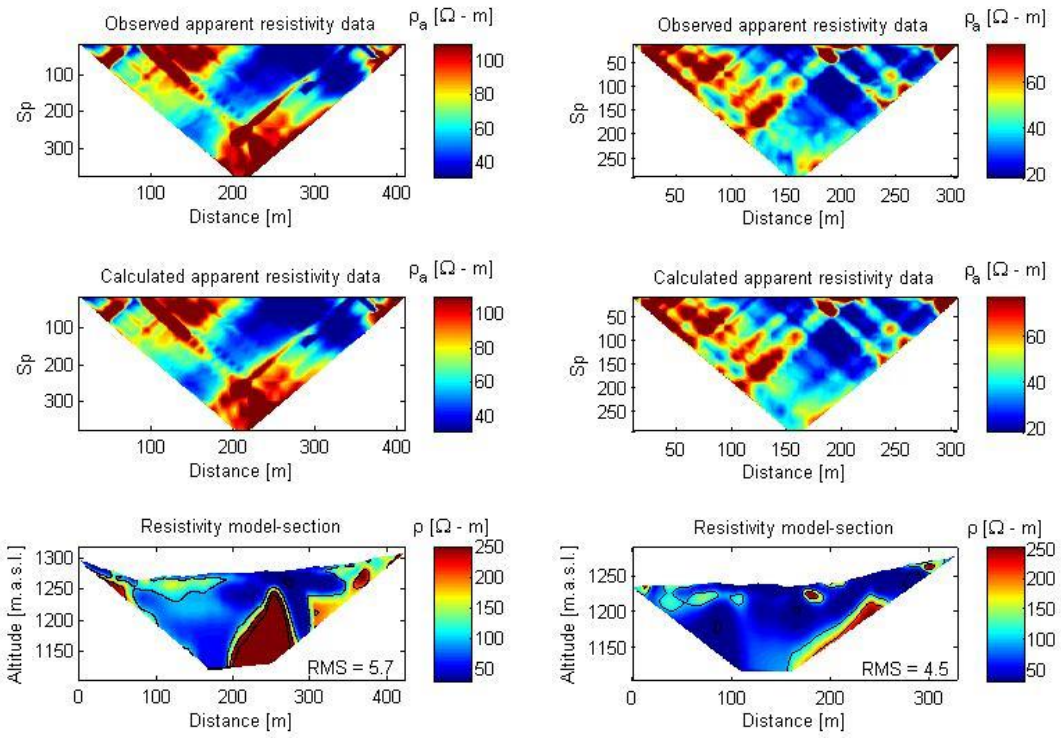

Figure E-6. (left) B-B’ profile and (right) C-C’ profile.

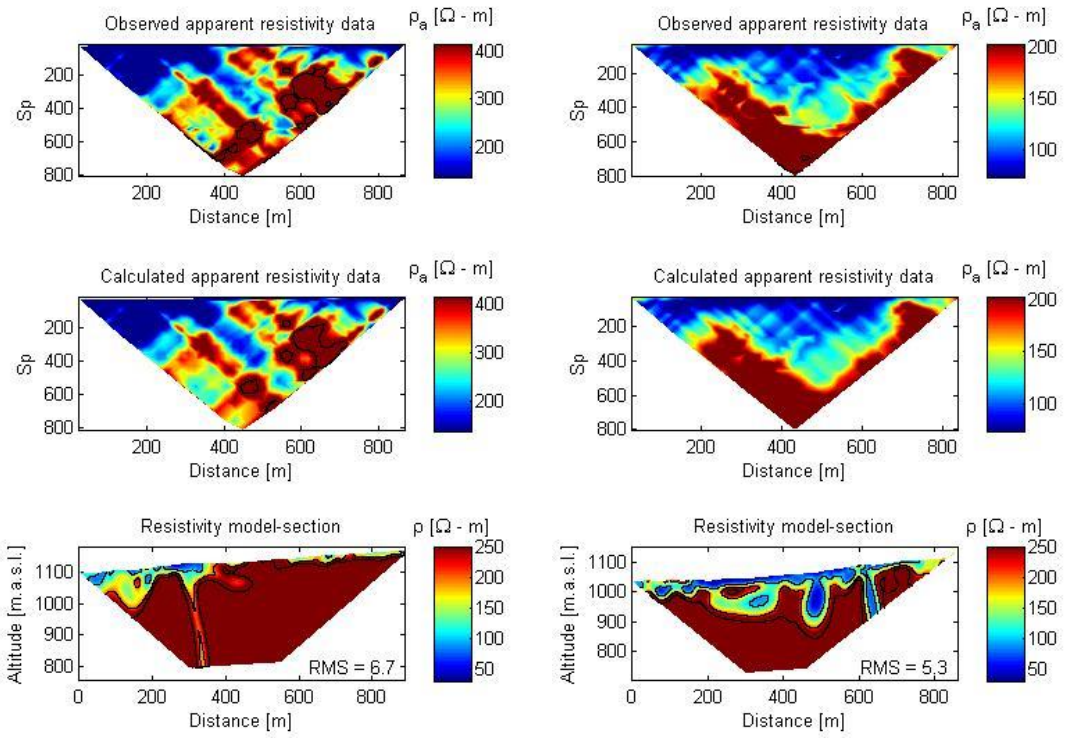

Figure E-7. (left) D-D' profile and (right) E-E' profile.

In addition, A-A' profile – section 7 was modeled considering different dipping cases for LRSB. Fig. E-8 shows two other alternatives for the modelling of that section, both were discarded due to geological evidence.

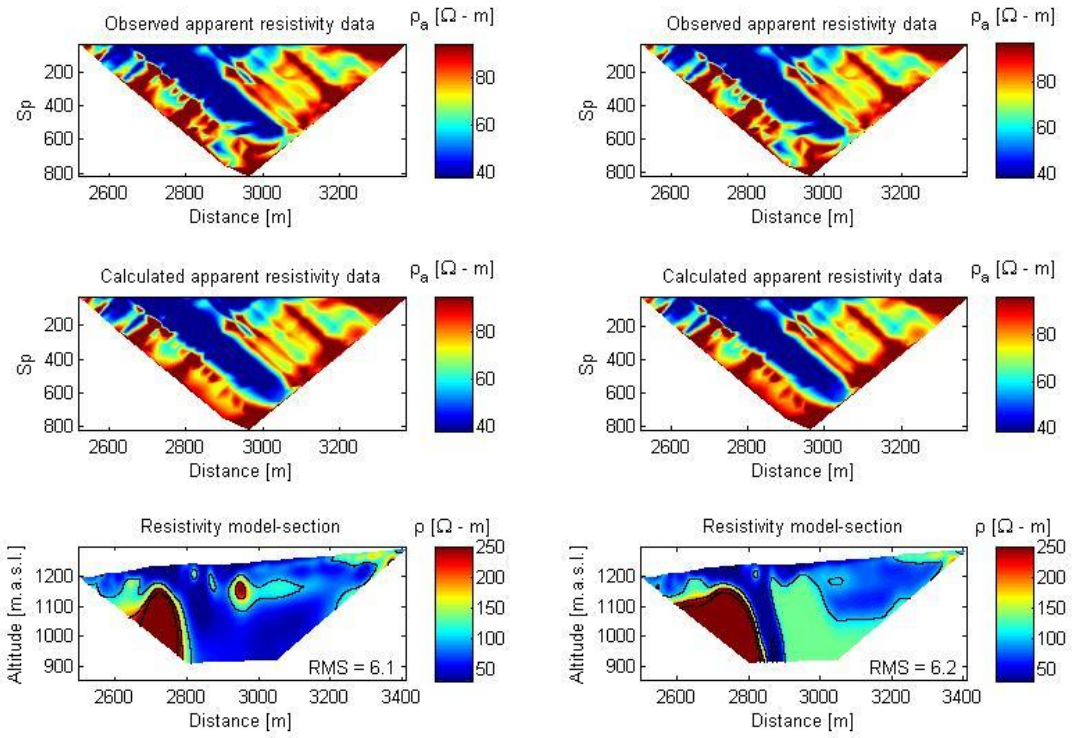

Figure E-8. A-A' profile – section 7. (left) inversion model (right) forward model with fault dipping NE.

E.2 Site 2

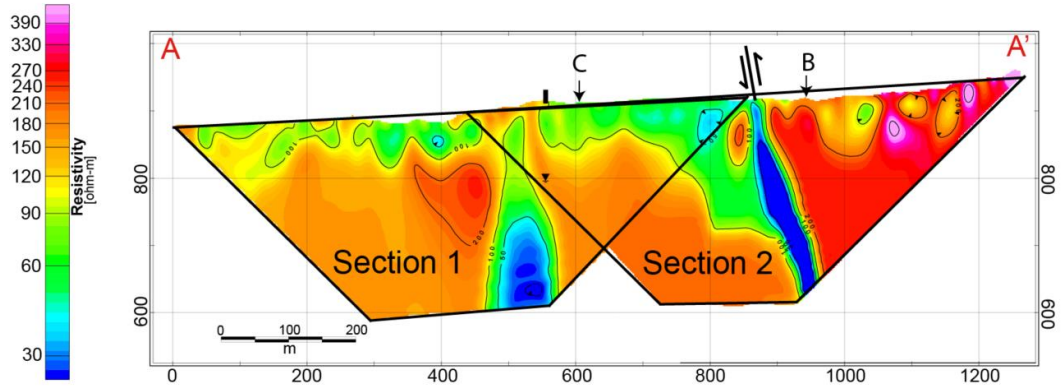

Figure E-9. A-A' profile and details of each section that compound this profile.

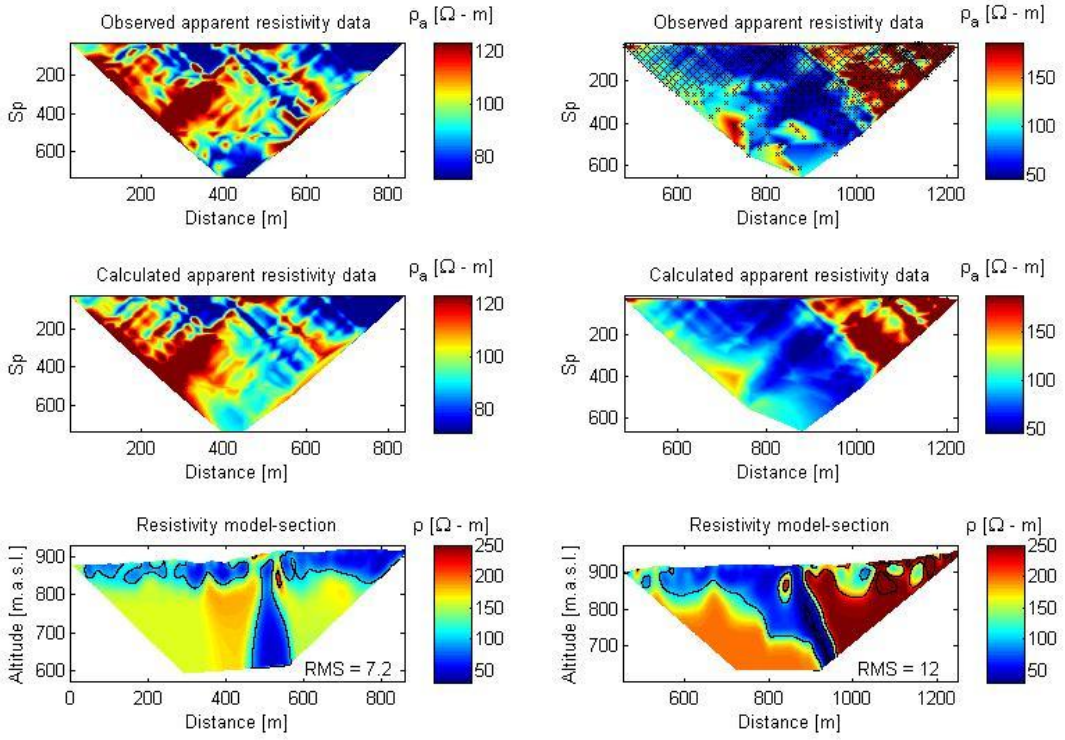

Figure E-10. A-A’ profile, (left) section 1 and (right) section 2.

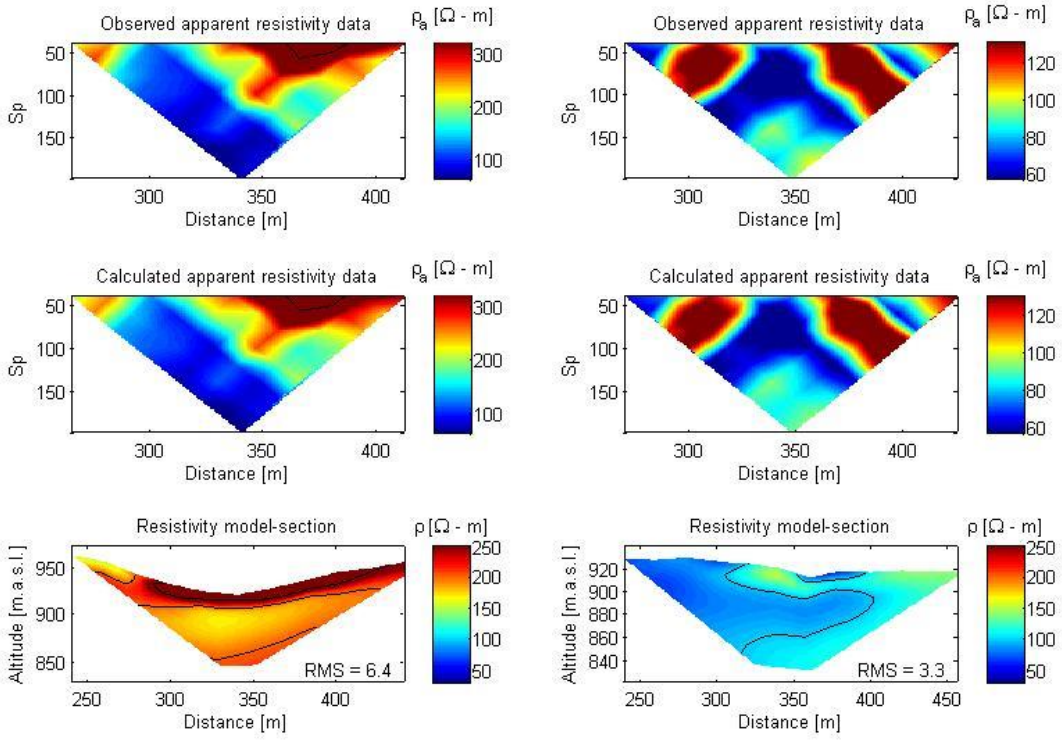

Figure E-11. (left) B-B' profile and (right) C-C' profile.

In addition, A-A' profile – section 2 was modeled considering different dipping cases for LRSB. Fig. E-12 shows two other alternatives for the modelling of that section, both were discarded due to geological evidence and gravity model.

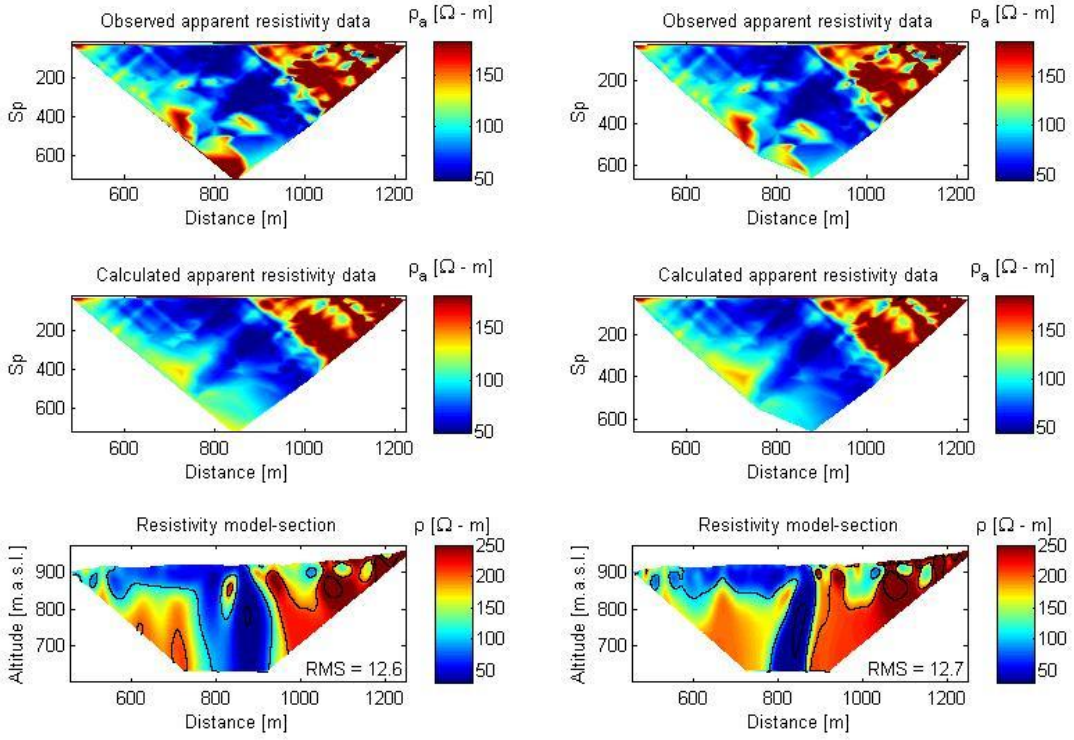

Figure E-12. A-A' profile – section 7. (left) inversion model (right) forward model with fault dipping W.